NANOMECHANICS OF PLASTICITY IN ULTRA-STRENGTH METALS AND SHAPE MEMORY ALLOYS

A Thesis
Presented to
The Academic Faculty

by

Yuan Zhong

In Partial Fulfillment
of the Requirements for the Degree
Doctor of Philosophy in the
School of Mechanical Engineering

Georgia Institute of Technology
December 2012

NANOMECHANICS OF PLASTICITY IN ULTRA-STRENGTH METALS AND SHAPE MEMORY ALLOYS

Approved by:

Dr. Ting Zhu, Advisor
School of Mechanical Engineering
Georgia Institute of Technology

Dr. Olivier Pierron
School of Mechanical Engineering
Georgia Institute of Technology

Dr. Kenneth Gall
School of Materials Science and Engineering
Georgia Institute of Technology

Dr. Arash Yavari
School of Civil and Environmental Engineering
Georgia Institute of Technology

Dr. David McDowell
School of Mechanical Engineering
Georgia Institute of Technology

Date Approved: 08/20/2012

This thesis is dedicated to the memory of my uncle, Fuyi Zhong.

ACKNOWLEDGEMENTS

First and foremost I offer my sincerest gratitude to my advisor Dr. Ting Zhu for his guidance, encouragements, patience and constructive criticisms. He supported me through all the hardest stages of my thesis and mentored me with his depth of knowledge. Without him, this thesis would not have been completed or even written. One simply could not wish for a better or friendlier advisor.

As committee members, Dr. Kenneth Gall, Dr. David McDowell, Dr. Olivier Pierron and Dr. Arash Yavari provided me their precious guidance, motivation and support during various stages of my research. Their suggestions are very helpful to enhance the level of my research work.

I extend my sincere thanks to the Woodruff School of Mechanical Engineering for offering me such a great opportunity to pursue my PhD degree and all the help and service during my study and research.

I also want to extend my gratitude to my fellow researchers: Dr. Ke Lu, Dr. Jun Lou, Dr. Wei Wang, Dr. Lei Lu for their help and collaboration throughout the research.

TABLE OF CONTENTS

		Page
ACKNOWLEDGEMENTS		1
LIST OF TABLES		4
LIST OF FIGURES		5
LIST OF SYMBOLS AND ABBREVIATIONS		7
SUMMARY		8
CHAPTER		
1	Introduction	10
	Martensitic phase transformation in nanoscale NiTi shape memory alloys	10
	Nucleation-controlled plasticity in ultra-strength metallic nanomaterials	15
2	Atomistic nanotwin in NiTi martensite	18
	Introduction	18
	Methods	21
	Results and discussions	26
	Conclusions	40
3	Pseudoelasticity and shape memory in NiTi nanopillars	42
	Introduction	42
	Methods	44
	Results and discussions	47
	Conclusions	64
4	Patterning and branching of martensitic nanotwins	66
	Introduction	66
	Methods	67

Results and discussions 68

Conclusions 74

5 Phase field modeling of martensitic microstructure in NiTi 75

Introduction 75

Methods 76

Results and discussions 84

Conclusions 95

6 Dislocation nucleation during nanoindentation 96

Introduction 96

Methods 97

Results 106

Discussions 114

Conclusions 121

7 Conclusions 122

APPENDIX A: Crystallographic theory of twinned martensite 124

APPENDIX B: Stress field in Fourier space 128

REFERENCES 132

LIST OF TABLES

Page

Table 2.1: Potential parameters for NiTi 22

Table 2.2: Comparison of lattice constant for NiTi 27

Table 2.3: Elastic constants of the B2 phase 28

Table 5.1: Compatibility of twin variants 88

Table 5.2: Compatibility of twin variants (alternative results) 90

Table 5.3: Compatibility of twin variants (different boundary conditions) 92

Table 5.4: Compatibility of twin variants (different crystallography) 95

Table 5.5: Compatibility of twin variants (different crystallography) 95

Table 6.1: Elastic constants of stress-free single crystals of Al, Cu and Ni 100

Table 6.2: Indentation moduli for single crystals of Al, Cu and Ni 107

Table 6.3: The critical resolved shear stress of dislocation nucleation 112

Table 6.4: Force and displacement at the onset of displacement bursts 116

LIST OF FIGURES

Page

Figure 2.1: Schematics of a tetragonal unit cell 23

Figure 2.2: Relaxed atomic structures of single phase NiTi 27

Figure 2.3: Relaxed structures of (001) compound twins 29

Figure 2.4: Relaxed structures of (010) compound twins 29

Figure 2.5: Twin structures with different twin widths 32

Figure 2.6: Relaxed atomic structures of (010) nano twins 34

Figure 2.7: MD simulation of phase transformation 37

Figure 3.1: Schematic of a tetragonal unit cell 46

Figure 3.2: Nanopillar compression at 400K with the applied strain up to 6.6% 48

Figure 3.3: Nanopillar compression at 400K with the applied strain up to 10.6%. 55

Figure 3.4: Nanopillar compression at 350K (Shape memory) 58

Figure 3.5: Nanopillar compression at 350K (Pseudoelasticity) 61

Figure 4.1: Martensitic transformation in thin film at 250K 69

Figure 4.2: Refinement and branching of nanotwins at 200K 72

Figure 5.1: 3D phase field simulation results 85

Figure 5.2: Different polytwinned microstructures 89

Figure 5.3: Microstructures at different applied boundary conditions 92

Figure 5.4: Formation of polytwinned martensitic microstructures 94

Figure 6.1: Stress-strain curves for simple shear of single crystals of Al, Cu, Ni 103

Figure 6.2: Finite element mesh for indentation simulation 105

Figure 6.3: Nanoindentation load-displacement curves 108

Figure 6.4: IPFEM predictions of nucleation sites 111

Figure 6.5: Displacement versus resolved shear stress at the critical nucleation site 113

Figure 6.6: Experimental results of nanoindentation in Cu 114

Figure 6.7: Modeling of nanoindentation in Cu 120

Figure A.1: Illustration of martensitic phase transformation in NiTi 125

LIST OF SYMBOLS AND ABBREVIATIONS

A_s	Austenite start temperature
A_f	Austenite finish temperature
M_s	Martensite start temperature
M_f	Martensite finish temperature
r_c	Cut-off radius
E'	Effective Young's modulus
f_{local}	Local specific free energy density
f_{int}	Interfacial energy density
f_{ela}	Strain energy density
$\xi_i(\boldsymbol{x}, t)$	Langevin noise term
k_B	Boltzmann constant
T	Temperature
NiTi	Nickel-Titanium
SMAs	Shape-memory alloys
MD	Molecular dynamics
MC	Monte Carlo
AFM	Atomic force microscopy
TEM	Transmission electron microscopy
HRTEM	High resolution transmission electron microcopy
IPFEM	Interatomic potential finite element method
fcc	Face-centered-cubic
3D	three-dimensional
2D	two-dimensional

SUMMARY

Recent experiments of nanoscale materials have shown the strong nano-size effects on their mechanical properties, such as the loss of pseudoelasticity and ultrahigh mechanical damping in shape memory alloys, and the ultra-high strength phenomena in metals. Understanding these unique properties and size effects at the nanoscale is critically important to the application of micro/nano-devices. The underlying mechanisms of nanoscale plasticity could be governed by the phase transformation or nucleation-controlled plasticity. In this thesis, we study the plasticity mechanisms of diffusionless martensite phase transformation in Nickel-Titanium (NiTi), one of the most widely used shape memory alloys. We also study the nucleation-controlled plasticity mechanisms in different metals of Copper (Cu), Aluminum (Al) and Nickel (Ni). The objective of this thesis is to elucidate the mechanisms of plasticity in the nanoscale metals and alloys by both the atomistic and phase field modeling at different time and length scales.

We study the plasticity mechanisms of martensitic phase transformation in NiTi shape memory alloys. NiTi usually exhibits various metastable phases (B2, B19, B19′, R etc.), the activation of which depends sensitively on temperature, loading, concentration, and precipitation, etc. The formation of a variety of twin structures further complicates the study. In the past the continuum theory and first principles calculations have been employed to study such a complicated system. However, they are deficient in terms of resolving the mechanisms of martensitic phase transformation. The research here involves four thrusts focusing on different length and time scales: (I) Molecular statics and dynamics simulations are applied to study the nanotwin structures and temperature-driven B2 → B19′ phase transitions. (II) Molecular dynamics simulations are performed

to explore the stress-driven martensitic phase transformation governing the pseudoelasticity and shape memory effects in NiTi nanopillars. (III) Monte Carlo simulations are conducted to characterize the temperature- driven B2 → B19 phase transition and the patterning of martensitic nanotwins in NiTi thin films. (IV) Phase field simulations are performed to predict the formation and evolution of complex martensitic microstructures, including the detailed analysis of twin compatibility under complex loading conditions. The above results not only provide new insights into the nanoscale martensitic phase transformation in NiTi, but also provide an effective modeling framework for studying the diffusionless phase transformation in large systems with atomic resolution.

We also study the nucleation-controlled plastic deformation in metals. Our work focuses on understanding how dislocations nucleate in single crystals. Interatomic potential finite element method is applied to determine when, where and how dislocations nucleate during nanoindentation in metals such as Cu, Al and Ni. We explore the effects of indentation orientation on the characteristics of activated dislocation sources. Results provide insight into the nanoscale mechanisms of plastic yielding, and are useful for guiding the nanomechanical experiments in the future.

Overall, the nanomechanics study in this thesis provides novel mechanistic insights into the deformation mechanisms in shape memory alloys and ultra-strength metallic nanostructures.

CHAPTER 1

INTRODUCTION

1.1 Martensitic phase transformation in nanoscale NiTi shape memory alloys

Shape-memory alloys, when deformed, can recover to their original shape upon unloading and heating [1-3]. Nickel-titanium (NiTi) is one of the most widely used SMAs [4]. The shape memory effect of NiTi usually results from the diffusionless martensitic phase transformation between the cubic B2 (austenite) and monoclinic B19′ (martensite) phase. NiTi can also exhibit pseudoelasticity [4], i.e., deformation is fully recovered upon unloading without the aid of heating. Compared to shape memory, pseudoelasticity similarly involves the martensitic phase transformation, but it occurs when the deformation temperature is higher, typically above the austenite finish temperature A_f.

The generation of large and reversible strains during both the shape memory and pseudoelasticity is governed by the diffusionless martensitic phase transformation of the crystal lattice in response to applied thermo-mechanical loadings [4-7]. Recent development in the processing, characterization and mechanical testing of nanostructured shape memory alloys provides opportunities of revealing the nanometer length scale effects on martensitic phase transformation, and may offer practical solutions of efficient shape memory, actuation, and mechanical damping in the microscale and nanoscale devices [8-16].

Understanding the martensitic transformation of nanostructured shape memory alloys first depends on knowing the structures of various phases at the nanometer scales. NiTi usually exhibits various metastable phases (B2, B19, B19′, R etc.), the activation of which depends sensitively on temperature, loading, concentration and precipitation, etc.

The most characteristic feature of martensites (B19, B19′, R etc.) is the existence of twin structures, which would help to accommodate the incompability between the martensite and the austenite. Twin martensites are conventionally classified as type I twin (i.e., the twin plane is a rational crystal plane), type II twin (i.e., the twin shear is a rational crystallographic direction) and compound twin (both the twin plane and twin shear are rational) [1]. The structures of martensite depend sensitively on the size. For example, in coarse-grained NiTi, type I and type II twins are more often observed than compound twins. This can be rationalized in terms of the requirement of deformation compatibility at extended interfaces (i.e. habit planes) between martensite and austenite. In contrast, compound twins typically form in nanocrystalline NiTi. Further, the twin-related variants were observed to span the entire nano-sized grain, so that the martensitic transformation-induced kinematic incompatibility is accommodated by the grain boundary rather than the habit plane. Such nanostructural size effect on martensitic phase transformation has been studied by Waitz and coworkers by considering the competing effects of twin boundary energy, grain boundary energy and elastic energy of twin variants and surrounding matrix [17, 18].

A next-level study of the martensitic phase transformation is concerned with how the phase transformation occurs and what the unique properties are at the nanoscale. A typical martensitic phase transition in NiTi involves the transformation from a high-temperature B2 cubic austenite phase to a low-temperature B19′ monoclinic martensitic phase [4]. The nanoscale size effects are observed and illuminated with the aid of recent development in the nanomechanical testing [9, 10, 13, 16-24]. For example, Frick et al. showed that decreasing diameter of NiTi sub-micrometer pillars inhibits and ultimately

suppresses the pseudoelasticity when diameters decrease to 200nm [13]. This size effect could be possibly due to the suppression of martensitic phase transformation. However, the martensitic phase transformation of B2 → B19′ was observed in NiTi pillars of 200nm diameter by in situ electron diffraction experiment [16]. It was thus suggested that the loss of pseudoelasticity might arise owing to incomplete strain recovery (austenite phase transformation), despite the occurrence of martensitic phase transformation [21]. In contrast to the loss of pseudoelasticity, the shape memory was usually measured for pillars with diameters of 200nm with the help of heating [21].

In the past the continuum theory and first-principles calculations have been employed to study the NiTi system involving multiple phases, twin structures and their temporal evolution during phase transformation. Continuum theory is limited to explain the atomistic level structure and deformation mechanisms. And first-principles calculations are deficient in terms of resolving the mechanisms of martensitic phase transformation and plastic deformation, especially in large systems that are necessary to capture the effects of long-range elasticity and complex twin structures. Those previous studies are also limited by the simulation time scale. To study the structures of various phases and martensitic phase transformation at the micro- and nano-scale, we develop a modeling framework that integrates the crystallographic theory of martensite, molecular statics and molecular dynamics (MD), Monte Carlo (MC), and phase field simulations. Considering the complexity of martensitic microstructures and phase transformation, as well as a large range of time and length scales involved, these atomistic and phase field modeling approaches are expected to play an important role in bridging the experiments,

continuum modeling and *ab inito* calculations for understanding the transformation mechanisms in shape memory alloys [18, 25-30].

1.1.1 Atomistic nanotwin structures in NiTi martensite

In Chapter 2, we perform the molecular statics and dynamics simulations to study in detail the atomic-scale structures of nanotwins in NiTi shape memory alloys. An empirical interatomic potential [31] is originally developed to describe the properties of NiTi, which has been benchmarked by both experimental measurements and first-principles calculations. However, it is deficient with discontinuities at cutoff radius. We modified this potential and improved the predicted properties. Based on the modified potential, atomistic simulations are performed to study the structures and geometrical limit of nanoscale twins in NiTi martensite. We analyze compound twins as narrow as about one nanometer, involving a few atomic layers. A novel nanotwinned structure is found, forming through the martensitic transformation of sub-lattices. We predict the transition temperatures for the thermal-induced phase transformation in bulk NiTi, which are consistent with experimental measurements. The results provide an atomistic basis for further study of the martensitic phase transformation process, pseudoelasticity and shape memory behavior in nanoscale NiTi.

1.1.2 Pseudoelasticity and shape memory in NiTi nanopillars

In Chapter 3, we perform the molecular dynamics simulations to study the atomistic mechanisms governing the pseudoelasticity and shape memory in NiTi nanostructures. For a $\langle 110 \rangle$ – orientated nanopillar subjected to compressive loading-unloading, we observe either the pseudoelastic or shape memory response, depending on

the applied strain and temperature that control the reversibility of phase transformation and deformation twinning. We show that the irreversible twinning arises owing to the dislocation pinning of twin boundaries, while the hierarchically twinned microstructures facilitate the reversible twinning. The nanoscale size effects are manifested as the load serration, stress plateau, and large hysteresis loop in the stress-strain curves, resulting from the high stresses required to drive the nucleation-controlled phase transformation and deformation twinning in nano-sized volumes. Our results underscore the importance of atomistically resolved modeling for understanding the phase and deformation reversibilities that dictate the pseudoelasticity and shape memory behavior in nanostructured shape memory alloys.

1.1.3 Patterning of martensitic nanotwins in NiTi thin films

In Chapter 4, we perform the Monte Carlo simulations of pattern formation in NiTi thin films. The above discussed atomistic simulations based on MD are limited by the achievable time scale (a few nanoseconds at most), so that the temperature-induced phase transformation in nanostructural NiTi is not easily accessible by the MD simulations. To overcome this limitation, we develop an atomic-level Monte Carlo simulation with importance sampling Markov Chain. We study the martensitic phase transformation and the pattern formation of martensitic nanotwins in a NiTi thin film. We show that large undercooling can lead to the refinement and branching of nanotwins, dictated by geometrical constraints at the interface between the martensitic thin film and austenitic substrate. The simulated twin refinement is consistent with a scaling analysis of the twin width, which depends on both the sample size and the characteristic material length that scales with the twin boundary thickness. Our work opens a new avenue

towards predictive modeling of the patterned martensitic microstructure at the atomic scale.

1.1.4 Phase field modeling of martensitic microstructure in NiTi

In contrast to the previous chapters that focus on the atomistic simulations, in Chapter 5, we perform the coarse-grained phase field simulations of formation and evolution of martensitic microstructures in the bulk of NiTi alloys. Atomistic simulations are not computationally efficient to study the large systems, with size larger than one micrometer involving over one billion atoms. In this chapter, the phase field simulations have been performed to study the martensitic microstructures in the large systems of bulk NiTi alloys. Our simulations enable the detailed characterization of the martensitic phase transformation from the B2 phase to twelve B19′ variants for exploring the twin compatibility and temporal evolution of martensitic microstructures under complex loading conditions. The three-dimensional simulations show the nucleation and growth of twelve monoclinic B19′ variants that form the polytwinned morphology of martensitic microstructures. The mechanical constraints govern both the selection and spatial patterning of multivariants in the formation of strain-accommodating microstructures. The present phase field model is generally applicable to study the dynamic evolution of complex alloy systems that involve multi-variants and polytwinned microstructures.

1.2 Nucleation-controlled plasticity in ultra-strength metallic nanomaterials

Metallic nanomaterials usually exhibit the “ultra-strength” properties [32]. That is, the measured strength (on the level of a few GPa) reaches a significant fraction of the ideal strength of perfect crystal, considerably larger than their coarse-grained counterparts (typically in the range of ten to hundred MPa). This phenomenon has been

shown by an increasing number of experiments such as bending of silver nanowire using atomic force microscopy (AFM) [33], compression of gold nanopillars [34], and nanoindentation in copper [35]. Moreover, the force-displacement curves of the aforementioned nanopillar compression and nanoindentation experiments are discontinuous. This implies the nucleation-controlled plasticity that produces the pronounced load discontinuities for releasing the stored deformation/elastic energy by dislocation formation.

The ultra-strength phenomenon can be caused by dislocation starvation [34]. In nanoscale materials, mobile dislocations can only travel a short distance before annihilating at a nearby free surface; they tend to leave the crystal rapidly without interacting with each other. Thus the probability of dislocation multiplication (through the mechanisms such as double cross slip and Frank-Read type sources) decreases. As a result, plasticity tends to be controlled by dislocation nucleation instead of dislocation multiplication. As the required stress for dislocation nucleation is generally higher than the one needed to move and multiply dislocations, the material strength increases. Nucleation-controlled plasticity often manifests as discontinuity in the nanopillar compression and nanoindentation experiments, because discrete nucleation events could lead to a pronounced load drop or displacement burst. The dislocation starvation has been directly observed by *in situ* Transmission electron microscopy (TEM) compression test of Ni nanopillars [36] , in which dislocations disappear as a result of mechanical annealing.

The above review motivates our study of nucleation-controlled plasticity in nanomaterials. However, the mechanisms of nucleation of dislocations are still not well understood. A multi-scale simulation method has been applied to explore the nucleation

controlled plasticity during the nanoindentation experiments. The effects of hyperelasticity have been considered to accurately describe the materials' properties.

1.2.1 Dislocation nucleation during nanoindentation

In Chapter 6, we perform the interatomic potential finite element method (IPFEM) simulations of dislocation nucleation during nanoindentation of face-centered-cubic metals. Dislocation nucleation is central to our understanding of the onset of plasticity during nanoindentation. The shear stress in small volumes beneath the nanoindenter can achieve the theoretical limit of a perfect crystal. The ensuing nonlinear elastic instability can trigger homogenous dislocation nucleation inside the crystal. Here we employ the interatomic potential finite element method to simulate nanoindentation and predict dislocation nucleation. Simulations are performed for indentation on the (111), (110) and (100) surfaces of Al, Cu, Ni single crystals. We quantify the critical conditions of dislocation nucleation, including the indentation load of nucleation, location of nucleation site, nucleation stress and activated slip system. We find these conditions sensitively depend on indentation orientation, but are consistent for different crystals. The results highlight the critical role of hyperelasticity (the nonlinear elasticity caused by elastic softening at large strain) and crystallography in dislocation nucleation in small material volumes. In addition, we use the IPFEM simulations to analyze the stochastic, discontinuous plasticity in nanoindentation experiments, and determine the nature of dislocation sources (i.e. surface versus bulk nucleation) in nanoindentation of Cu with different crystal orientations [37].

CHAPTER 2

ATOMISTIC NANOTWIN STRUCTURES IN NITI MARTENSITE

2.1 Introduction

Shape-memory alloys (SMAs) are a unique class of alloys which can recover to original undeformed shape from the deformed one by heating [1, 2, 5, 7]. Nickel-titanium (NiTi) is one of the most important SMAs [4]. The shape memory effect of NiTi based alloys typically involves the martensitic phase transformation from cubic B2 (austenite) to twinned monoclinic B19′ phase (martensite) through B2 → B19′ or B2 → tetragonal B19 → B19′, etc. [4, 38-42]. B19′ phase exhibits different twin structures (type I twin, type II twin and compound twin) to accommodate the displacement constraints during the martensitic phase transformations.

SMAs have strong potential applications such as damping and actuation [14, 43] in micro/nano-devices; however, the unique properties at nanoscale raise new challenges for further exploration [13, 16, 17, 19, 39, 44, 45]. Understanding the martensitic transformation in nanostructured shape memory alloys first requires the understanding of the structures of various martensitic phases in nanometer scale. In this chapter, we develop an atomistic modeling framework and apply atomistic simulations to study the structures of nanotwins in NiTi. We utilize the crystallographic theory of twinned martensite [46, 47] to construct the initial twin structures. Then the atomistic calculation is performed by using an empirical interatomic potential [31], which has been benchmarked by experimental values and first principles calculations. Our atomistic simulation goes beyond the crystallographic theory by providing more structural details

and mechanistic insights at the sub-lattice level. Compared to the first principles calculation [17, 39, 45, 48-51], it enables an efficient exploration of twinned microstructures, and can be further utilized to study their spatial-temporal evolution and associated phenomena of plasticity at the atomic scale, which is discussed in Chapter 3. Considering the complexity of martensite microstructures, as well as a large range of time and length scales involved in the martensitic transformation processes, the empirical potential-based atomistic modeling approach developed is expected to play an important role in bridging experiments, continuum models [18, 25-30, 52-55, 56], and *ab initio* calculations for understanding the transformation mechanisms in shape memory alloys.

The work in this chapter is focused on understanding the atomic-scale twin structures in NiTi martensite, and is motivated by recent high resolution transmission electron microcopy (HRTEM) imaging of nanocrystalline NiTi, showing the unique martensitic phase of nanoscale compound twins spanning the entire nano-sized grain [17]. It is useful to recall that a typical martensitic phase transition in NiTi involves the transformation from a high temperature B2 cubic austenite phase to a low temperature B19' monoclinic martensitic phase [4]. The most characteristic feature of martensitic transformation is the formation of twins, where the arrangement of the lattice on one side of the twin boundary plane is related to those on the other. Twin martensites are conventionally classified as type I (i.e., the twin plane is a rational crystal plane), type II (i.e., the twin shear is a rational crystallographic direction) and compound twin (both the twin plane and twin shear are rational); their rigorous definitions can be found for example in the review by Christian and Mahajan [1]. In coarse-grained NiTi, type I and type II twins are more often observed than compound twins. This can be rationalized in

terms of the requirement of deformation compatibility at extended interfaces (i.e. habit planes) between martensite and austenite. Namely, compared to the compound twins, the formation of type I and type II twins can better achieve geometrical compatibility with the parent B2 phase of austenite [41]. In contrast, compound twins often form in nanocrystalline NiTi [17]. Furthermore, the twin-related variants can span the entire nano-sized grain, so that the kinematic incompatibility caused by martensitic transformation is accommodated by the grain boundary rather than the habit plane. Such a size effect of nanostructures on martensitic phase transformation has been studied by Waitz and his coworkers by considering the competing effects of twin boundary, grain boundary, and elastic energies associated with the twin variants and surrounding matrix [17, 18]. However, it is not yet well understood from an atomic basis why they form and how stable they are.

In this chapter, we study the atomic-level details of nanotwinned structures by combining the crystallographic theory and atomistic simulation. We analyze the compound twins as narrow as about one nanometer, involving a few atomic layers. The HRTEM images of twinned structures [17] provide the validation for our simulations. We discover a novel transformation mode that may have implications for the martensitic phase transition of materials with the complex lattice structure, common to crystalline alloys and compounds. We also study temperature-driven phase transformations and the size effects. The results provide an atomistic structural basis for further investigation of martensitic phase transformation and shape memory behavior of the shape memory alloys at the nanometer scale [57].

2.2 Methods

2.2.1 Interatomic potential

A many-body interatomic potential is developed to describe the NiTi system. This potential was originally developed by Lai and Liu [31], and is improved in this work with a smooth cutoff behavior to avoid the diverging forces in simulations involving large atomic displacements. As a Finnis-Sinclair type potential [58], the potential function is constructed by using the second-moment approximation of the tight-binding theory. The total energy of the system is expressed as

$$E = \sum_i \left\{ \sum_{j \neq i} A_{\alpha\beta} \exp\left[-p_{\alpha\beta} \left(\frac{r_{ij}}{d_{\alpha\beta}} - 1 \right) \right] - \sqrt{\sum_{j \neq i} F(r_{ij})} \right\} \qquad (2.1)$$

where

$$F(r_{ij}) = \xi_{\alpha\beta}^2 \exp\left[-2q_{\alpha\beta} \left(\frac{r_{ij}}{d_{\alpha\beta}} - 1 \right) \right] \qquad (2.2)$$

Here, r_{ij} is the distance between atom *i* and *j*, and α and β denote the type of atoms (Ni or Ti) at sites *i* and *j*, respectively. In Eq. (2.1), the first term in the curly bracket describes the pair interaction and the second term represents the many-body effect. The potential parameters were fitted to the properties of the B2 phase at 0K from first principles calculations, and the potential cut-off radius r_c was determined to be 4.2 $\mathring{A}$ [31]. However, $F(r_{ij})$ and its derivative about r_{ij} are non-zero at r_c. To be suitable for use in molecular statics and dynamics simulations that generally require smooth energies and interatomic forces, we have modified the potential by changing $F(r_{ij})$ as follows,

$$F(r_{ij}) = \begin{cases} \xi_{\alpha\beta}^2 \exp\left[-2q_{\alpha\beta}\left(\frac{r_{ij}}{d_{\alpha\beta}} - 1\right)\right], & r_{ij} \le r_1 \\ c_{3,\alpha\beta}(r_{ij} - r_1)^3 + c_{2,\alpha\beta}(r_{ij} - r_1)^2 + c_{1,\alpha\beta}(r_{ij} - r_1) + c_{0,\alpha\beta}, & r_1 < r_{ij} \le r_c \end{cases} \quad (2.3)$$

In Eq. (2.3), for given r_1 the four coefficients of $c_{0,\alpha\beta}$ to $c_{3,\alpha\beta}$ are solely determined by four continuity conditions, namely, $F(r_{ij})$ and its first derivative are continuous at both r_1 and r_c. We determine r_1 by optimizing the predicted properties.

Table 2.1. Potential parameters for NiTi. A and ξ are in the unit of eV, and d in $\mathring{A}$.

	Ni-Ni	Ti-Ti	Ni-Ti or Ti-Ni
D	2.49	2.95	2.607
A	0.104	0.153	0.3
P	11.198	9.253	7.9
ξ	1.591	1.879	2.48
Q	2.413	2.513	3.002
c_3	27.3341	122.395	47.8513
c_2	-7.54308	-34.205	-12.92362
c_1	-0.26286	-1.0054	-0.572708
c_0	0.13561	0.59012	0.248676

The potential parameters are listed in Table 2.1 with $r_1 = 4.0\mathring{A}$ and $r_c = 4.2\mathring{A}$. This modified potential not only removes the discontinuities at r_c, but also improves the predicted properties, including the lattice constant and energy of various phases of NiTi, as compared with *ab initio* calculations in Table 2.2. In our atomistic calculations of single phases, both the atomic coordinates as well as the side lengths and angles of the simulation box are fully relaxed by using the stress-controlled conjugate gradient energy minimization [59, 60].

2.2.2 Crystallographic theory of twinned martensite

We have utilized the crystallographic theory of twinned martensite to facilitate the atomistic simulation of nanotwins in NiTi. While it is desirable to generate and analyze the nanotwins by direct molecular dynamics (MD) simulations, the attainable twin structures are limited because of the well-known timescale limitation of MD and the associated low efficiency of sampling the atomistic energy landscape when the atomic-level structure is not precisely known. To overcome these limitations, we construct the initial twin structures based on the crystallographic theory of twinned martensite, and then relax the system by using the stress-controlled conjugate gradient energy minimization. In this way, various type I, type II, and compound twins can be accessed for detailed analyses. Moreover, the direct atomistic simulation can go beyond the crystallographic theory to reveal more sub-lattice level information and insights.

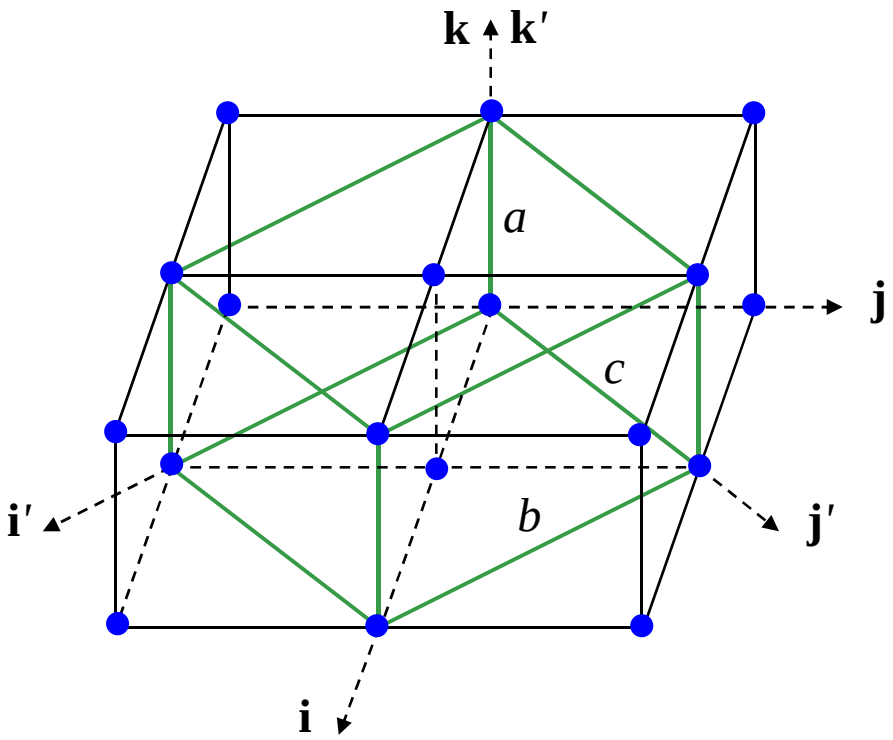

Fig. 2.1 Schematically shows a tetragonal unit cell (green lines) and four cubic unit cells (black lines) in the lattice of untransformed B2 parent phase. Only Ni atoms are shown for clarity. The orthonormal vectors $(\mathbf{i}, \mathbf{j}, \mathbf{k})$ are along the cube axes, and the orthonormal vectors $(\mathbf{i}', \mathbf{j}', \mathbf{k}')$ are along the cube directions of $[1\bar{1}0]$, $[110]$ and $[001]$, respectively.

The crystallographic theory of twinned martensite requires an input of the transformation matrix from the cubic parent phase to the martensitic phase. With this information, the twinning elements, including the twin plane normal and twin shear, can be predicted by solving the twinning equation that governs the kinematic compatibility between adjoining twin variants. Consider, as an example, the martensitic transformation from the B2 to B19' phase. Following the notation used by Knowles and Smith [40], the transformation takes a tetragonal unit cell of the parent B2 phase (Fig. 2.1) into a monoclinic cell of the product B19' phase. The associated lattice deformation involves a uniform expansion or contraction of the tetragonal cell, followed by a simple shear. In the orthonormal basis $(\mathbf{i}', \mathbf{j}', \mathbf{k}')$ given in Fig. 2.1, the deformation gradient matrix can be represented

$$\mathbf{F} = \frac{1}{a_0}\begin{bmatrix} b/\sqrt{2} & 0 & 0 \\ 0 & c\sin\beta/\sqrt{2} & 0 \\ 0 & -c\cos\beta/\sqrt{2} & a \end{bmatrix} \tag{2.3}$$

where a_0 is the lattice parameter of the cubic unit cell in B2, a, b, c are the lattice parameters of the monoclinic unit cell in B19', and β is the associated monoclinic angle between the edges with lengths of a and c. Prior to martensitic transformation, $a = a_0$, $b = c = \sqrt{2}a_0$ and $\beta = 90^\circ$. The shuffling of atoms in the cell was ignored in the crystallographic theory of martensitic transformation [40].

Twin variants of the B19' phase should satisfy the kinematic compatibility condition given by the twinning equation [7]

$$\mathbf{Q}\mathbf{F}_I - \mathbf{F}_J = \mathbf{m} \otimes \mathbf{n} \tag{2.4}$$

where $\mathbf{F}_I$ and $\mathbf{F}_J$ denote the symmetry-related deformation gradient of variant I and J, respectively, $\mathbf{n}$ is the normal vector of the twinning plane at the untransformed reference B2 state, $\mathbf{m}$ is the twinning shear vector at the transformed current B19' state, and $[\mathbf{m} \otimes \mathbf{n}]_{ij} = m_i n_j$. Eq. (2.4) essentially requires that any vector lying in the twin plane, which separates the two adjoining variants, should undergo the same deformation when viewed from either side. Note that $\mathbf{Q}$ represents an additional rotation of variant I after the transformation by $\mathbf{F}_I$; namely, the total transformation imposed on variant I is $\mathbf{Q}\mathbf{F}_I$. The rotation matrix $\mathbf{Q}$ is needed whenever the orientations of the twin planes are different after the transformations of variant I by $\mathbf{F}_I$ and variant J by $\mathbf{F}_J$. For the martensitic transformation from the cubic B2 to monoclinic B19' phase, there are 12 distinct variants. The transformation is conventionally described in terms of the symmetric deformation matrix $\mathbf{U}$ obtained from the polar decomposition of deformation gradient $\mathbf{F}$. Then there are 132 possible variant pairs between 12 monoclinic variants and those pairs can be classified as type I, type II or compound twin [1]. Solutions of Eq. (2.4) for type I, type II, and compound twins have been cataloged by Hane and Shield [41]. In this work, we focus on compound twins in order to directly compare simulations with available HRTEM images of twinned structures. Detailed solutions of compound twins suitable for atomistic calculations in the periodic supercell, including $\mathbf{F}_I$, $\mathbf{F}_J$, $\mathbf{m}$, and $\mathbf{n}$, are given in the Appendix A. Our method is general and applicable to create type

I and type II twins, and it can be further developed to produce complex twin microstructures (e.g., twinned wedges in the austenite matrix [7]) for providing an atomistic structural basis of studying their spatial-temporal evolution.

2.3 Results and discussions

2.3.1 Single phases

Figure 2.2 shows the relaxed structures of the B2, B19', and base-centered orthorhombic (BCO) single phases of equiatomic NiTi. Table 2.2 lists the lattice parameter, monoclinic angle and energy per atom for each phase calculated by the interatomic potential. Most results given by the potential are close to the available experimental values and *ab initio* calculations. However, the energy of the BCO phase (-5.069eV per atom) is slightly higher than that of the B19' phase (-5.073eV per atom), whereas the more accurate *ab initio* calculations predicted that BCO has a lower energy at zero temperature [48]. On the other hand, the B19' phase is most commonly observed in experiments at low temperatures [4]. It is still an open question as to the most stable martensitic phase at low temperatures. Nevertheless, the geometric features of nanotwins reported in this work are expected to be robust, as most of them are symmetry related. But one should take caution in interpreting the relative magnitude of energies among various phases and twins predicted by the potential. Also note that as shown in Fig.2.2(c), the relaxed BCO phase (with an orthorhombic unit cell in white lines) can be equivalently considered as B19' twinned at the level of unit cells (green lines) with the resulting monoclinic angle $\beta \approx 107^\circ$. This geometrical view was advanced by Huang et al. [48],

providing an interesting connection between nanotwinned and single phase structures. Table 2.3 lists the elastic constants of the B2 phase calculated from the interatomic potential at 0K, which are close to *ab initio* calculations. Due to omission of the temperature effects or lattice vibrations, these results are larger than experimental values measured at and above room temperatures [61, 62].

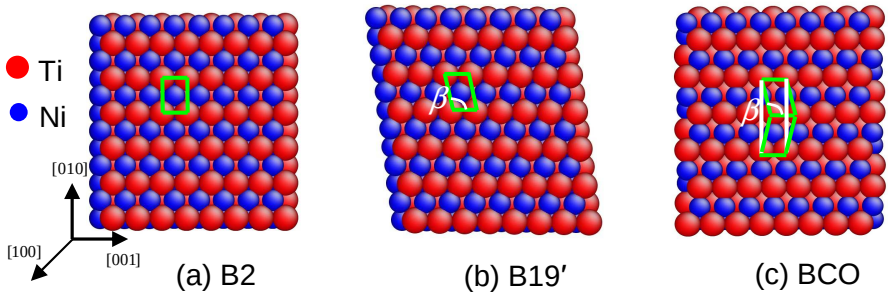

Fig. 2.2 Relaxed atomic structures of single phase, equiatomic NiTi, viewed from the [100] direction in the $(\mathbf{i}', \mathbf{j}', \mathbf{k}')$ basis of Fig. 2.1. (a) B2 phase, the rectangle indicates a tetragonal unit cell. (b) B19' phase, the parallelogram indicates a monoclinic unit cell with the monoclinic angle $\beta \approx 98^\circ$. (c) Base-centered orthorhombic (BCO) phases, the rectangle (white lines) indicates a BCO unit cell; the BCO structure can also be considered as a twinned B19' and each variant consists of one layer of monoclinic unit cell (green lines) with $\beta \approx 107^\circ$.

Table 2.2 Comparison of lattice constant, *a*, *b*, *c* , monocline angle β, and the energy per atom *E* for single phases and compound twins, as well as their differences with the energy of the B2 phase E_{B2}. Results from this work are indicated by Finnis-Sinclair (FS)-potential. The experimental and *ab initio* values are taken from Knowles and Smith [40] and Wagner and Windl [45], respectively. The last two rows list the properties of

nanotwins with monolayers of monoclinic unit cells, shown in Fig. 2.6(b) and (c), respectively.

	Structure	a (Å)	b (Å)	c (Å)	β (°)	E (eV)	$E - E_{B2}$ (eV)
B2	experiment	3.015	4.264	4.264	90		
	FS-potential	3.008	4.253	4.253	90	-5.022	
	ab initio	3.008	4.253	4.253	90		
BCO	FS-potential	2.994	4.001	4.883	107.86	-5.069	-0.047
	ab initio	2.953	3.993	4.951	108.52		-0.050
B19'	experiment	2.889	4.120	4.622	96.8		
	FS-potential	3.005	4.022	4.466	98.08	-5.073	-0.051
	ab initio	2.941	4.035	4.685	97.78		-0.044
B19'	twin (Fig.4.6b)	3.062	4.018	4.391	Ti 94.44 Ni 93.96	-5.058	-0.036
B19'	twin (Fig.4.6c)	3.011 3.011	4.022 4.022	4.464 4.416	98.43 90	-5.075	-0.053

Table 2.3 Elastic constants (GPa) of the B2 phase calculated from the interatomic potential of this work, in comparison with *ab initio* calculations and experimental measurements at different temperatures.

	FS-potential (T = 0K)	*ab initio* (T = 0K)	experiments (T = 298K) [62]	experiments (T = 400K) [61]
C_{11}	206.3	183	162	137
C_{12}	135.8	146	129	120
C_{44}	46.9	46	34	34

2.3.2 Compound twins

Figures 2.3 and 2.4 show the relaxed structures of (001) and (010) compound twins, respectively. Here (001) and (010) refer to the $(\mathbf{i}', \mathbf{j}', \mathbf{k}')$ basis in Fig. 2.1, and they are equivalent to (001) and (110) in the $(\mathbf{i}, \mathbf{j}, \mathbf{k})$ basis. We focus on a single twin boundary by studying the thick twins such that neighboring twin boundaries are sufficiently separated to minimize their interactions. The effect of the twin thickness will be addressed later in Fig. 2.5. Notice that the initial structures of (001) and (010) twins are constructed by

using the transformation matrices of Eq. (A2) and (A1), respectively. When applying these transformation matrices to construct the atomic structures, one can choose to position the mathematical mirror twin plane at various locations, including exactly on an atomic layer or between atomic layers. As a result, several metastable twin-boundary structures are obtained after stress-controlled conjugate gradient energy minimization. The corresponding mirror twin plane is indicated by the dashed line in Fig. 2.3 and 2.4. The position of a twin plane is determined according to its definition, i.e. the arrangements of the lattice on one side of the twin boundary plane are mirror reflections of those on the other.

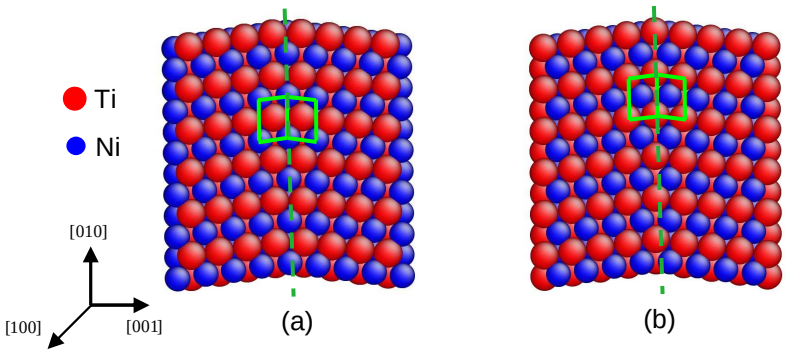

Fig. 2.3 Relaxed structures of (001) compound twins. The mirror twin plane (dashed line) is located on (a) the pure Ni laden layer and (b) the pure Ti layer, respectively.

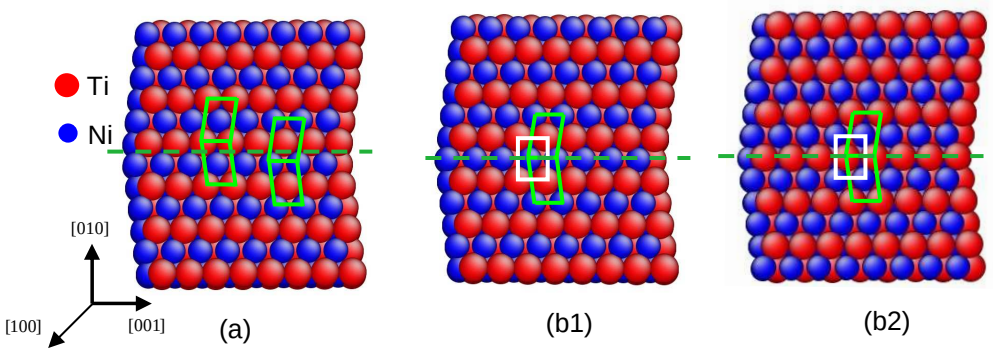

Fig. 2.4 Relaxed structures of (010) compound twins. The mirror twin plane (dashed line) is located (a) off the (010) atomic planes, and (b) on the (010) atomic plane. The front atomic layer in (b1) and (b2) exposes one of the two different (100) atomic planes of the same relaxed structure. The white unit cell of Ti atoms in (b1) and that of Ni in (b2) straddle the twin plane (dashed line), respectively, and remain the rectangular shape.

For the relaxed (001) compound twin shown in Fig. 2.3, the mirror twin boundary is always located on the atomic plane, irrespective the position of the twin plane. Since the (001) atomic planes consist of alternate pure Ni (blue atoms) or pure Ti (red atoms) layers, the mirror twin boundary can be either on a Ni laden plane (Fig.2.3(a)) or Ti laden plane (Fig. 2.3(b)). We define the twin boundary energy, γ, as the excess energy (in reference to the single phase of B19') divided by the boundary area. The calculated value of γ is, respectively, 0.136 J/m^2 and 0.047 J/m^2, indicating that the twin boundary located on the Ti plane is more energetically favorable than that on the Ni plane.

In contrast, for the relaxed (010) compound twin shown in Fig. 2.4, the energy minimization results in structures with the twin mirror plane located either on or off the atomic layer. To understand the "on" and "off" possibilities, one should notice the following geometrical feature of (010) planes. In contrast to the (001) planes that involve the alternate pure Ni and pure Ti layers generating the twin structures shown in Fig. 2.3, the order arrangement of atoms in a (010) plane involves a 2D rectangular net of Ni atoms interpenetrating a rectangular net of Ti atoms. As such, all the (010) planes are equivalent in terms of chemical arrangement of Ni and Ti atoms. Consequently, if the mirror twin plane is located on the atomic layer, there exists only one type of boundary

structure, as discussed next with Fig. 2.4(b). Interestingly, adjacent (010) layers differ by an in-plane shift in the diagonal direction of the 2D rectangle cell of Ni (or Ti) by one half of the diagonal length. As a result, one period in the [010] direction involves two neighboring (010) atomic planes.

Figure 2.4(a) shows the relaxed structures when the mirror twin plane is off the atomic layers. One can see that the mirror reflection is only approximately satisfied by unit cells of atoms near the twin boundary. The corresponding twin boundary energy γ is 0.089J/m^2, larger than 0.014J/m^2 from the first principles calculation [17]. In contrast, Fig. 2.4(b) shows the relaxed structure when the mirror twin plane is on the (010) atomic plane. Note that in Figs. 2.4(b1) and (b2) the front atomic layer of the simulation box exposes one of the two different (100) planes of the same relaxed structure, respectively. It is seen that the mirror reflection is obeyed by the parallelogram-shaped unit cells (in green) on the two sides of the twin plane. Moreover, the mirror twin plane is located in the middle of unit cells in white, and these cells keep the rectangle shape so as to maintain the symmetry about the twin plane. Such boundary is structurally different from that in Fig. 2.4(a), resulting in a different twin boundary energy $\gamma = -0.0091\,\text{J/m}^2$. While the small negative boundary energy could be specific to the interatomic potential, this boundary structure can possibly exist as a metastable state, justified by the local symmetry of the lattice. It follows that this kind of boundaries is expected to be observable in experiments, considering that the shape memory alloys generally consist of various co-existing metastable structures. As discussed next, the available HRTEM image [17] shows evidence of their existence.

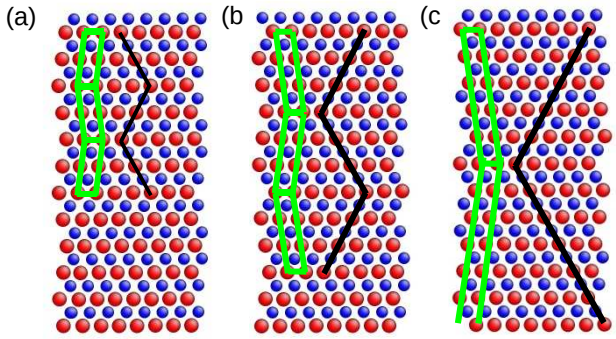

Fig. 2.5 Atomistically simulated twin structures with different twin widths, i.e. each green-colored twin variants comprises (a) 2, (b) 3 or (c) 6 layers of monoclinic unit cells. Black lines are drawn for guiding eyes, equivalent to the white lines in the TEM image by Waitz et al. (Fig. 2 in their paper) [17].

The HRTEM image of nanocrystalline NiTi by Waitz et al. has revealed the formation of nanoscale (010) compound twins that can span the entire grain [17]. It was observed that the thickness of twins varies in the same grain, and the thinnest variant is about 1 nm, involving two layers of monoclinic unit cells. These unit cells seem to be rectangular rather than monoclinic, lending a support to the existence of the boundary structures shown in Fig. 2.4(b). Further HRTEM experiments and *ab initio* calculations are needed to clarify the exact boundary structure.

To understand the effects of the twin thickness, we create (010) compound twins with the thickness of 2, 3 and 6 layers of monoclinic unit cells. Figure 2.5 shows the cases with the twin mirror plane located between the atomic planes, similar to Fig. 2.4(a). The twin boundary energies extracted from various twin structures in Fig. 2.5 are close to $\gamma \approx 0.09$ J/m^2. These nearly constant values indicate the validity of separating the total energy into the bulk and excess interfacial parts for the nanotwinned system. More

specifically, for coarse twins, it is common to analyze the optimal twin geometry in terms of competing effects of the increase of the total twin boundary energy with the decreasing twin thickness and the associated decrease of the bulk elastic energy caused by the geometric incompatibility of transformed phases with the surrounding materials [18]. The foregoing results show that such an approach can be extended to analyze the nanotwinned structures at low temperatures, considering the nearly constant twin boundary energies at the nanometer scale.

2.3.3 Geometrical limit of nanotwins

We have explored the geometrical limit of nanoscale twins with monolayers of the monoclinic unit cell, whereas the hitherto experiment only reveals nanotwins as thin as two layers of monoclinic unit cells in each B19' variant, as discussed above. Figure 2.6 shows the relaxed structures of (010) compound twins with one layer of monoclinic unit cells in each variant. Their boundary structures are similar to those shown in Fig. 2.4, but the twin thickness is reduced to the minimum. To understand these structures, it is useful to note that the lattice of the B2 phase of NiTi can be viewed as four sets of interpenetrating tetragonal sub-lattices, as schematically shown in Fig. 2.6(a). The martensitic transformation from the B2 to B19' phase can be considered as an expansion or contraction along the edges of the tetragonal unit cell, followed by a simple shear to a monoclinic angle β.

Figure 2.6(b) shows the relaxed twin structure when the mirror twin plane is located off the atomic plane, and its twin boundary structure is similar to that in Fig.2.4(a). This is a simple case of uniform martensitic transformation, where each of the four sub-lattices consists of alternate single layer of monoclinic unit cells with $\beta \approx 94^{\circ}$.

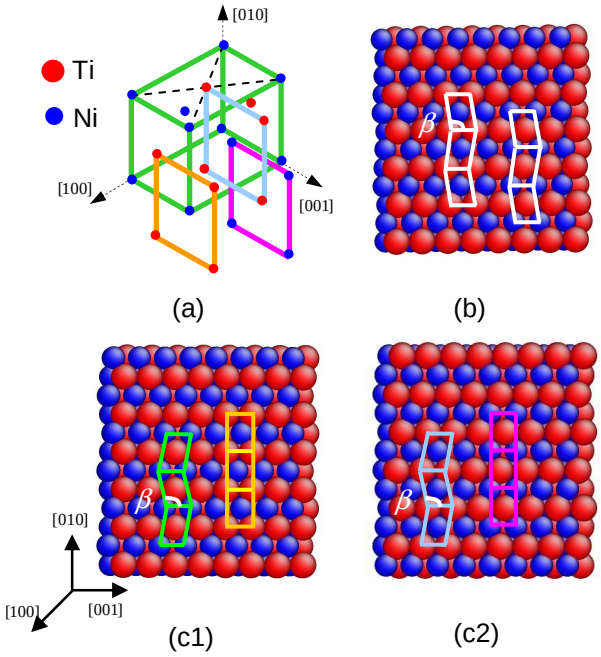

Fig. 2.6 Relaxed atomic structures of (010) twins with the smallest thickness (about 0.5nm), and each variant consists of one layer of monoclinic unit cells, i.e. two atomic planes. (a) Schematics of four sets of interpenetrating simple orthorhombic sub-lattices. One Ni sub-lattice is represented by a 3D green box, and the other Ni sub-lattice is indicated by a 2D pink rectangle instead of a 3D box for clarity. The two Ti sub-lattices are indicated by the orange and blue rectangles, respectively. (b) All sub-lattices are twinned, as indicated by the sheared unit cells. (c) A sub-set of interpenetrating sub-lattices is twinned. The front atomic layer of (c1) and (c2) exposes one of the two different (100) atomic planes, respectively. The Ni sub-lattice in (c1) and Ti sub-lattice in (c2) are twinned.

Of particular interest is that a new nanotwinned structure is found: one Ni sub-lattice and one Ti sub-lattice undergo martensitic transformations, while other Ni and Ti sub-lattices remain orthorhombic. This mode is discovered from the relaxed structure

when the martensitic transformations are imposed according to the matrices in Eq. (A1) with the mirror twin plane positioned at the (010) atomic plane; the relaxed boundary structure is similar to that in Fig. 2.4(b). Figures 2.6 (c1) and (c2) show the same state of such a twinned structure after energy minimization. Notice that because of interpenetration of 3D sub-lattices, one period in the [100] direction involves two neighboring (100) atomic planes. The front atomic layer of the simulation cell in Fig. 2.6(c1) and (c2) exposes one of the two different (100) planes, respectively. Comparing them with Fig. 2.6(a), one can see that one sub-lattice of Ni atoms (green cells in (c1)) and one sub-lattice of Ti atoms (blue cells in (c2)) consist of variants of single layer of monoclinic unit cells ($\beta = 98.43^\circ$), while one sub-lattice of Ti atoms (orange cells in (c1)) and one sub-lattice of Ni atoms (pink cells in (c2)) consist of orthorhombic unit cells ($\beta = 90^\circ$). One interesting feature is the tight coupling of sheared and un-sheared sub-lattices, resulting from interpenetration of the multi-lattices. While this nano-twinned structure was discovered from our atomistic simulations of equiatomic NiTi at zero temperature, it is geometrically reasonable and could present as metastable states in other alloy and compound systems with the multi-lattice structure [63, 64].

The alternate twinned structures shown in Fig. 2.6 can be considered as a single orthorhombic phase with the period doubled in the twin-plane normal direction of [010]. This geometrical view is motivated by a similar consideration of the single phase BCO as a twinned B19' with the monoclinic angle $\beta \approx 107^\circ$ [48], as discussed earlier. Of course, there is a notable difference between the two cases: all the sub-lattices of BCO are equivalent, whereas the new structure involves the interpenetration of alternatively sheared and un-sheared sub-lattices. Moreover, whereas these twin products were

obtained by a general procedure of constructing martensites according to Eq. (A1) followed by energy minimization, one may equivalently set up their initial states by shuffling every other (010) atomic plane in the [001] direction – the shuffling method has also been used to study the pathways of martensitic transformation [39, 65].

In the present geometrical limit of monolayer twinned structures, despite the spatial overlap of the bulk and twin boundary regions, the effective twin boundary energy (i.e., the excess energy per unit boundary area in reference to the B19' mono-variant) is still about $-0.0089\,\mathrm{J/m2}$, very close the values of $-0.0091\,\mathrm{J/m2}$ extracted from the previous cases of thicker nanotwins. As explained earlier, one should take caution in interpreting the energy values given by the interatomic potential. However, the geometric features of those nanotwins are symmetry related. They could possibly exist as metastable states, considering that the HRTEM image by Waitz et al. [17] has revealed the similar type of thicker nanotwins. Finally, to facilitate the future verification by *ab initio* calculations and experimental measurements, we list in Table 2.2 the predicted unit-cell geometry and energy per atom for the monolayer nanotwins shown in Figs. 2.6(b) and (c).

2.3.4 Phase transformation and size effect

Temperature-driven phase transformation is simulated by using the molecular dynamics (MD) simulation package LAMMPS [66]. We have implemented the NiTi potential in LAMMPS. In MD simulations, the starting structure is monoclinic B19'. The supercell box contains 9216 atoms. The system is subjected to periodic boundary conditions and fully relaxed to zero stresses. The temperature is initially set to 100K through thermal equilibration. Then the thermal load is applied by linearly varying

temperatures in three stages: (I) heating from 100K to 450K; (II) cooling from 450K to 100K; (III) re-heating until 450K. The MD simulation of each stage involves 200,000 time steps, each of which is 0.5fs. The phase transformation is characterized by geometrical changes of the simulation cell in terms of an order parameter, *W*, defined as the sum of all the shear components of the simulation box. *W* is further normalized by its maximum value, such that it varies between zero and one, corresponding to the cubic B2 and monoclinic B19' phases, respectively.

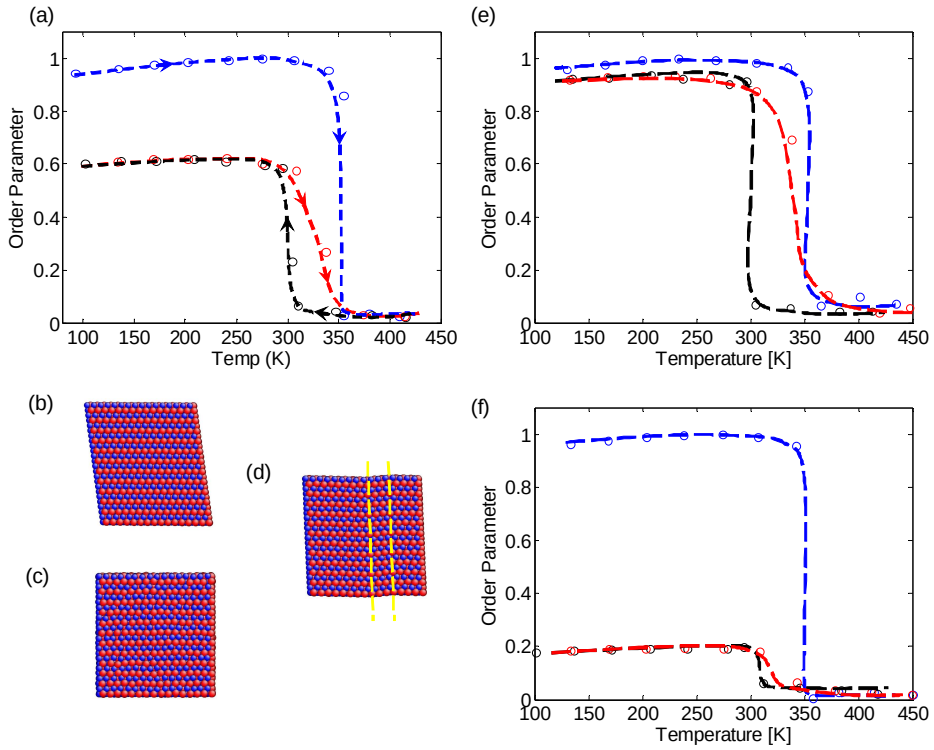

Fig. 2.7 MD simulation of phase transformation for different sizes of the simulation box. (a) The order parameter *W* as a function of temperature T for three stages of temperature loading: (I) heating (blue), (II) cooling (black), and (III) reheating (red). (b) The monoclinic B19' phase at the beginning of stage I of heating. (c) The cubic B2 phase at the end of stage I of heating. (d) The B19' phase at the end of stage II of cooling, forming

nanotwins indicated by dashed lines. (e) Same as (a) except that the volume is 1/8 of that in (a). (f) Same as (a) except that the volume is 8 times of that in (a).

Figure 2.7 shows that in stage I of heating (blue curve), W first increases slightly with temperature due to the effect of thermal expansion. As the temperature is further increased to around 350K, W decreases sharply to a very small value close to zero. Correspondingly, the B19' phase, Fig. 2.7(b), undergoes a structural phase transition to the B2 phase, Fig. 2.7(c). This indicates that both the start temperature, A_s, and finish temperature, A_f, of the B2 austenite are close to 350K.

In stage II of cooling (black curve), a similar abrupt change of W is observed as temperature is decreased to around 300K. This corresponds to the reverse transformation from the B2 austenite to the B19' martensite. Due to formation of the twinned B19' structures, Fig. 2.7 (d), W only increases to 0.6, smaller than $W = 1$ of a single B19' phase. This reduction of W can be attributed to the canceling effect of shearing of adjacent twin variants in the opposite directions, causing a decrease of the overall shear of the simulation box. The corresponding start temperature of the B19' martensite, M_s, is 310K and the finish temperature, M_f, is 290K, indicating that the formation of twinned structures occurs in a relatively narrow temperature range.

In stage III of reheating (red curve), the twinned B19' structure undergoes the transforms to a single B2 phase. The process starts at around 310K and finishes at 350K. Correspondingly, W deceases gradually from 0.6 to 0, in contrast to the abrupt change of W around 350K in stage I of heating of a single B19' phase. Both the decrease of A_s and gradual change of W can be attributed to the presence of twin boundaries acting as the

heterogeneous interfaces to facilitate the progressive de-twinning through boundary migration.

We further study the size effects of the simulation box on phase transformations. The length of all three sides of the simulation cell is either reduced by one half or doubled, corresponding to 1/8 and 8 times the previous volume, respectively. As shown in Figs. 2.7(e) and (f), the size effect is small on phase transition temperatures, indicating that the present MD predictions can well represent those of bulk NiTi. Indeed, the MD-predicted temperatures are only slightly lower (by 20K) compared to experimental values [67]. On the other hand, a size effect is observed on the magnitude of W. Namely, at the end of stage II of cooling, W decreases with the increasing size of the simulation box, implying that W will reach its lower limit of zero in bulk NiTi. This trend is expected because the twin variants in a large system can better self-accommodate their respective shear distortion, thereby reducing the overall (averaged) shear deformation. But the quantification of the size limit giving $W \approx 0$ is not feasible yet, due to the computational limitation on the time scale of MD simulations of large atomic systems. On the other hand, W increases as the size of the simulation box decreases. This is understandable by noting the following limit. For the smallest simulation box with one unit cell, the formation of twinned microstructures is completely suppressed because of the geometrical constraint of the simulation cell, so that W has to stay at its upper limit of one.

2.4 Conclusions

Combining the crystallographic theory of twinned martensite with atomistic simulations, we study the nanoscale twins and martensitic phase transformations in NiTi with the multi-lattice structure. We explore the geometrical limits of nanotwins by showing the possible formation of a nontrivial mode of twinned martensites: different sub-lattices undergo different martensitic transformations. These twin structures are metastable and likely to be attainable in nanoscale compound twins, as hinted by the HRTEM images by Waitz et al [17]. Our molecular dynamics simulations predict the phase transformation temperatures, consistent with experimental measurements [67]. We find both the formation of twinned microstructures and associated overall shear deformation are sensitive to the size of the simulation system.

The present atomistic study focuses on the structural aspects of nanoscale compound twins. In view of the imprecision of empirical interatomic potential, verification via experiments and first-principles calculations is needed to ascertain the conclusions. However, our results reveal the complexity of martensitic phase transformations at the sub-lattice level, and provide a structural basis for further atomistic study as well as multiscale modeling of the NiTi phase transformations through bridging the crystallographic theory with atomistic and quantum mechanical calculations. Furthermore, to fully reveal the physical origin of formation of nanotwins, the determination of the multilayer generalized gamma surface [44, 68] is needed. This type of calculation has been performed for elemental metals [68], but not NiTi with the multi-lattice structure. Finally, we note that the elemental metals (e.g. Cu) with nanotwins exhibited unusual properties, e.g., ultra-high strength with retained ductility and high

electrical conductivity [69, 70], the strongest twin size around 15nm [71, 72], etc. Nanotwins in alloy and compound systems are more complicated, and possibly work in a very different way than normal metals. This work is a necessary step towards understanding and exploiting the nanotwinned structure-property relationship in alloys and compounds with the complex multi-lattice structures.

CHAPTER 3

PSEUDOELASTICITY AND SHAPE MEMORY IN NITI NANOPILLARS

3.1 Introduction

Shape-memory alloys (SMAs), when deformed at a low temperature, recover to their original shape upon unloading and heating [1, 2, 5]. Nickel-titanium (NiTi) is one of the most widely used SMAs [4]. The shape memory effect of NiTi usually results from the reversible martensitic phase transformation between the cubic B2 (austenite) and monoclinic B19′ (martensite) phase. NiTi can also exhibit pseudoelasticity [4], i.e., deformation is fully recovered upon unloading without the aid of heating. Compared to shape memory, pseudoelasticity similarly involves the martensitic phase transformation, but it occurs when the deformation temperature is higher, typically above the austenite finish temperature A_f.

Both pseudoelasticity and shape memory have been extensively studied in the bulk SMAs [1, 2, 5]. However, these unique properties and size effects remain largely unexplored in the nanoscale SMAs [73], while they are being increasingly considered for use in micro/nano-devices for sensing, actuation, shape memory and mechanical damping [14, 43]. Recent development in the nanomechanical testing provides opportunities of illuminating the nanometer length scale effects on SMAs [9, 10, 13, 16-24]. For example, Frick et al. showed that decreasing diameter of NiTi nanopillars inhibits the pseudoelastic behavior and ultimately suppresses it for diameters of less than 200 nm [13]. This size effect could be possibly attributed to the suppression of martensitic phase transformation that gives way to dislocation plasticity. However, in a recent *in situ* electron diffraction

experiment, the martensitic phase transformation of B2 → B19′ was observed in NiTi pillars of 200nm diameter [16]. It was thus suggested that the loss of pseudoelasticity arises owing to incomplete strain recovery, despite the occurrence of martensitic phase transformation [21]. In contrast to loss of pseudoelasticity, the shape memory was measured for pillars with diameters of 200nm [21].

To understand the length scale effects on nanostructured SMAs, it is highly desired to develop the physics-based models to explore the structure-property relationship in these systems [31, 39, 44, 45, 48, 50, 74-78]. To this end, here we report an atomistic study of the pseudoelasticity and shape memory behaviors in NiTi nanopillars by using molecular dynamics (MD) simulations. We focus on the stress-induced martensitic phase transformation and deformation twinning, while the temperature-driven phase transformations has been reported in Chapter 2 [74]. It is important to note that compared to the previous atomistic study of pseudoelasticity and shape memory in pure metals [79-82], the NiTi alloy is complicated with the formation and evolution of a variety of phases (e.g., B2, B19, B19′, R and BCO) and twin structures (e.g., type I, type II and compound twins) [4]. However, it is likely that the facile multi-phase and multi-twin features could produce the pseudoelasticity and shape memory effects that are more robust and thus highly desirable to the “smart” micro/nano-devices. In this work, by controlling the applied strains and temperatures, we have simulated various characteristic stress-strain behaviors in shape memory alloys, such as pseudoelastic deformation, loss of pseudoelasticity, and shape memory. Our detailed atomistic characterization of the phase transformation and deformation twinning products offers new insights into the physical mechanisms governing the thermomechanical behavior of NiTi nanostructures.

3.2 Methods

A many-body Finnis-Sinclair type interatomic potential [58] is used to describe the NiTi system. This potential was originally developed by Lai and Liu [31], but it suffered from discontinuities at the cutoff radius. As discussed in Chapter 2, we modified the potential function by smooth interpolations near the cutoff with cubic polynomials [74]. The resulting NiTi potential not only enabled the well-behaved molecular statics and dynamics simulations, but also improved the predicted properties, including lattice constant and cohesive energy for a variety of phases [74].

In this chapter, we perform the MD simulations of uniaxial compression of NiTi nanopillars by using LAMMPS [66]. The initial structure is taken as the ordered B2 phase. A nanopillar with 46,080 atoms is constructed. It is 25.6 nm long, with a nearly square cross section, 4.8 nm×5.1 nm. The periodic boundary condition is applied only in the axial direction, such that the sidewalls of nanopillars are traction-free. The axial direction of nanopillar is aligned with $<110>_{B2}$ [19]. By thermal equilibration the simulation temperature is set to 400K, about 50K higher than A_f (~ 350K). The system is relaxed at zero stresses for 200,000 MD time steps, each of which is 0.5fs. The uniaxial compression is then applied by strain control. To explore the pseudoelastic deformation, a limited load range is applied up to 6.6% engineering strain. Note that all the strain values given in this paper refer to the magnitude of the applied compressive strain. The aforementioned strain limit is achieved in 400,000 time steps, followed by unloading to zero strain in another 400,000 time steps. As such, both loading and unloading correspond to a constant strain rate of about 3×10^8/s. Then we study the irreversible deformation after the complete martensitic phase transformation by imposing a larger

compressive strain up to 10.6%. Next, the temperature effect is investigated on both phase transformation and deformation twinning by reducing the deformation temperature to 350K, close to A_f. Last, the size effects on the stress- and temperature-driven phase transformation are discussed, as compared with the bulk NiTi behavior.

In all the MD simulations, we identify the formation of new phases in terms of the transformed lattice constants, internal atomic shuffling, and particularly monoclinic angle γ, i.e. $\gamma = 90^\circ$ for B2 and B19, $\gamma = 98^\circ$ for B19′, $\gamma = 108^\circ$ for the base centered orthorhombic (BCO) phase [74]. To reduce the error from thermal fluctuations, the aforementioned geometrical parameters are calculated by averaging over tens of MD time steps. Note that for a given temperature, several MD simulations have been performed with different initial distributions of randomly assigned atomic velocities, in order to explore the possibly different products of phase transformation and deformation twinning.

It is necessary to recall the crystallography of the B2 phase and B19′ phase of NiTi. Fig. 3.1 shows the lattice structure of the B2 phase with both cubic and tetragonal unit cells. We use a_0 to represent the lattice constant of the cubic unit cell. Correspondingly, the lattice parameters of the tetragonal cell are given by $a = a_0$ and $b = c = \sqrt{2}a_0$. In this paper, all the crystallographic orientations of different phases are referred to the $(\mathbf{i}, \mathbf{j}, \mathbf{k})$ basis of the cubic cell of the parent B2 phase. The martensitic transformation of B2 → B19′ takes a tetragonal unit cell into a monoclinic cell. The associated lattice deformation involves the expansion and contraction of the tetragonal cell, as well as a simple shear. We restrict $a < b < c$ in our notation. In B19′ the monoclinic angle γ between edges with length of a and c is around 98°, as measured

from experiments [4] and predicted from our MD simulations. The martensitic transformation also involves the atomic shuffling in unit cells, which can be directly simulated by MD.

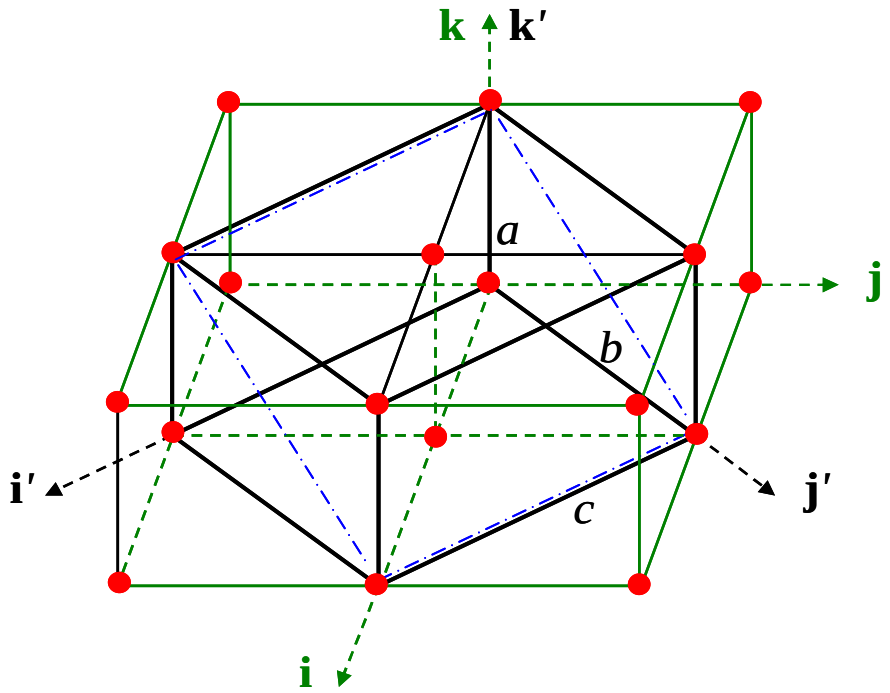

Fig. 3.1. Schematic of a tetragonal unit cell (black lines) and four cubic unit cells (green lines) in the untransformed B2 phase. Only Ti atoms (red circles) are shown for clarity. The orthonormal vectors $(\mathbf{i}, \mathbf{j}, \mathbf{k})$ are along the cube axes, and the orthonormal vectors $(\mathbf{i}', \mathbf{j}', \mathbf{k}')$ are along the cube directions of $[1\bar{1}0]$, $[110]$ and $[001]$, respectively. The rectangle enclosed by dash-dotted lines is the $\{112\}_{B2}$ twin plane, refereed to the $(\mathbf{i}, \mathbf{j}, \mathbf{k})$ basis of the cubic unit cell.

3.3 Results and discussions

3.3.1 Pseudoelasticity and reversible phase transformation

Fig. 3.2 shows the MD results of uniaxial compression of a NiTi nanopillar at a temperature of 400K, about 50K above the bulk value of A_f. Fig. 3.2 (a) presents the initial structure of the nanopillar in the B2 phase. During compression, the successive phase transformations of B2 → B19 → B19′ occur. Fig. 3.2(b) plots the corresponding stress-strain curve with the maximum compressive strain of ε = 6.6%. The compressive deformation constitutes four stages: (I) the initial linear response (ε < 2.5%) represents the elastic deformation of the B2 (austenite) phase; (II) the continuous but nonlinear response (2.5% < ε < 3%) corresponds to the martensitic phase transformation of B2 → B19, manifested by a smooth increase of slope; (III) another linear response (3% < ε <5.8%) signifies the completion of martensitic phase transformation to B19 and subsequent elastic deformation of B19; (IV) the load drop at ε ~ 5.8% indicates the phase transformation of B19 → B19′.

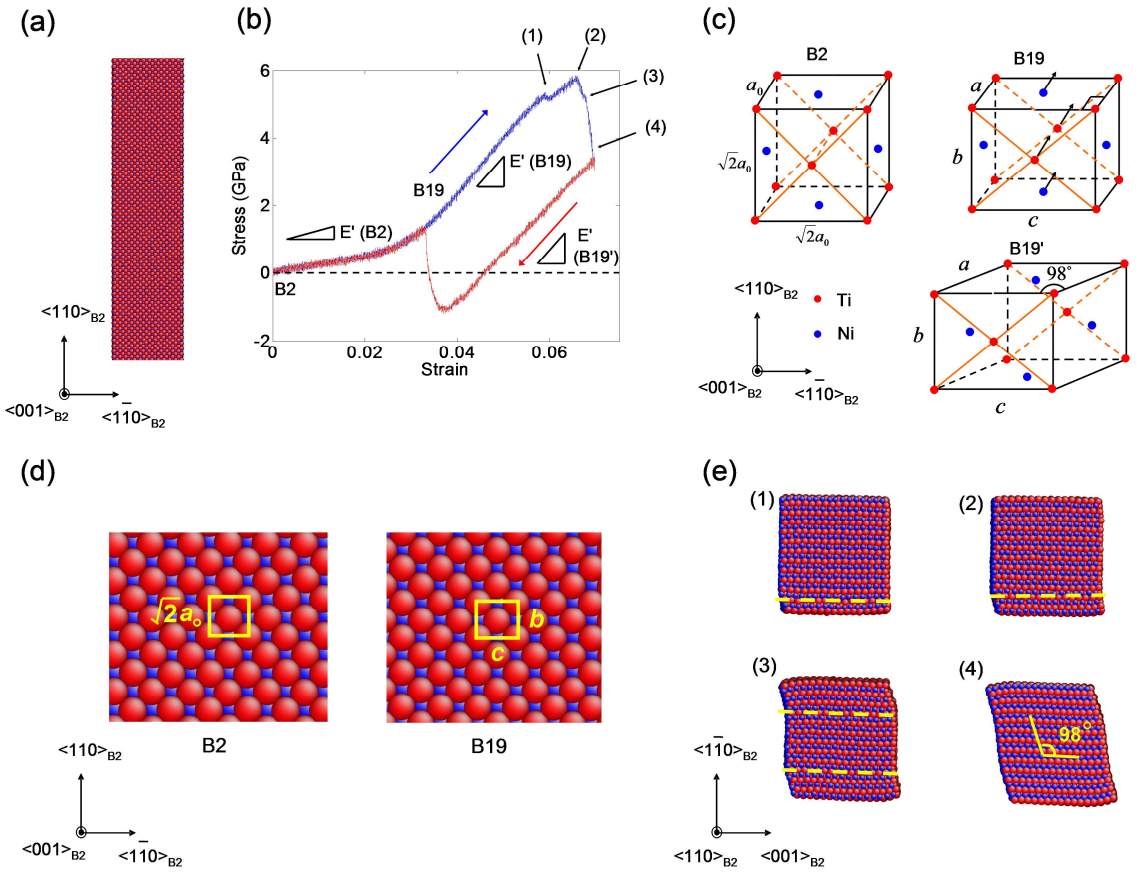

Fig. 3.2. Nanopillar compression at 400K with the applied strain up to 6.6%. (a) Initial structure in the ordered B2 phase (red atoms represent Ti and blue atoms Ni). (b) Stress-strain curve of loading (blue) and unloading (red); a positive stress means tension. (c) Schematics of B2, B19, B19′ unit cells. (d) Side view of the nanopillar before and after the phase transformation of B2 → B19. (e) Top view of the sequential steps of the B19 → B19′ phase transformation; the dashed line indicates the phase boundary.

Next, each of the aforementioned loading stages is described in detail. During stage I (ε < 2.5%), we start with the cubic B2 (CsCl type) phase of NiTi. Fig. 3.2 (c) shows the schematic of its atomic structure in a conventional tetragonal unit cell which includes both Ni and Ti atoms. This austenite phase is stable at 400K. Its effective Young's modulus E' is about 29GPa, estimated from the slope of the initial stress-strain

curve in Fig. 3.2 (b). Since the nanopillar is compressed in the $\langle 110 \rangle_{B2}$ direction, the corresponding Young's modulus can be related to the elastic constants of the B2 phase by

$$E' = \frac{2}{1/C_{44} + 1/(C_{11} + C_{12} - 2C_{12}C_{12}/C_{11})} \qquad (3.1)$$

Using Eq. (3.1) one can compare E' predicted from our MD with the experimental value. The elastic constants of the B2 phase have been measured by Brill et al. [61] at the same temperature of 400K as MD. On the basis of their experimental data, we estimate $E' = 39\text{GPa}$, consistent with our MD result. On the other hand, the B2 phase at low temperatures is metastable. It can be accessed in the well-controlled atomistic modeling, but not in experiment. As such, for the 0K case, we compare the results between the interatomic potential and *ab initio* density functional theory calculations. Using Eq. (3.1), we calculate E' from the 0K elastic constants predicted by the interatomic potential, yielding 72.9GPa. It is comparable to the value of 62.2GPa from the *ab initio* 0K elastic constants by Hatcher et al. [44], but smaller than 128.7GPa from Wagner and Windl [45]. From the above results at 400K and 0K, one see a strong temperature effect on the moduli of the B2 phase.

During stage II (2.5% < ε < 3%), the stress-strain curve in Fig. 3.2 (b) is continuous but nonlinear. This stage of deformation features the phase transformation of cubic B2 → tetragonal B19, as schematically illustrated by their respective unit cells in Fig. 3.2 (c). Fig. 3.2 (d) shows the atomic structures of nanopillar before and after B2 → B19. The lattice deformation associated with phase transformation can be understood in terms of a direct loading effect. The lattice constant *b* in B19 is smaller than the corresponding value of $\sqrt{2}a_0$ in B2 [44, 45, 48, 50]. As a result, the applied compression

along $<110>_{B2}$ tends to promote the formation of B19 with a smaller lattice constant in the loading direction. In addition, internal shuffling of atoms within the unit cell is observed in our MD, i.e. the atoms in $\{110\}$ planes move in the $[001]$ direction, as indicated by the arrows in Fig. 3.2 (c). Our results agree well with a recent study by Hatcher et al. [39, 44]. They performed the first principles calculations of energy barriers of multilayer shear, and found the shuffling on $[001]\{110\}$ requires the lowest energy barrier or even no energy barrier, depending on the number of the sheared layers. The shuffling mode from our MD essentially corresponds to their two-layer $[001]\{110\}$ shuffling. However, this mode is different from the $[1\bar{1}0]\{110\}$ basal shear/shuffle proposed by Otsuka and Ren [83]. It is still an open question concerning which shuffling mode dominates in the B2 → B19 phase transformation.

During stage III ($3\% < \varepsilon < 5.8\%$), the B19 phase is elastically deformed, and its effective Young's modulus is ~ 145GPa. The corresponding experimental data is currently unavailable. Combining stages I - III, we note that during the B2 → B19 phase transformation, a 5.8 % strain can be achieved through only 0.5 % phase transformation and 5.3 % elastic strain. This is because in such a stress-driven transformation process, a large elastic strain (~ 2.5%) is required. The large elastic loading can be sustained by the system because it is single crystalline without pre-existing internal defects. Furthermore, the B2 to B19 phase transformation involves a continuous and nonlinear variation of lattice constant. This implies a continuous diminishing of the energy barrier of the B2 to B19 transformation with increasing loading, characteristic of a second-order phase transition. Such a continuous process results in a small transformation strain of 0.5%.

Likewise, the B19 phase can sustain a large elastic strain, as it does not contain pre-existing internal defects.

During stage IV (ε > 5.8%), the deformation features the phase transformation of B19 → B19′. The resulting monoclinic angle γ of the B19′ phase is ~98°, as indicated in Fig. 3.2 (c). Notice that the shear transformation occurs in the plane (containing *a* and *c*) perpendicular to the loading direction. Furthermore, the transformation involves the nucleation and growth of the B19′ phase from the B19 parent matrix, to be discussed next. The associated stress-strain curve is plotted in Fig. 3.3 (b). During this stage of phase transformation, there are two load drops occurring at the strain of 5.9% and 6.6%, respectively. The first load drop is relatively small, only a few hundred MPa. It is followed by a load increase. The second load drop is considerably larger, ~ 2GPa. The compressive loading terminates at this point, while the stress-strain behavior under a further load increase will be studied to explore the martensite plasticity in the next section.

The aforementioned nucleation and growth of the B19′ phase is shown in detail by a cross-sectional view of the nanopillar in Fig. 3.2 (e). The B19′ phase first nucleates at a $\{1\,\bar{1}\,0\}_{B2}$ free surface of the pillar, Fig. 3.2 (e1), resulting in the first load drop in Fig.3.2 (b). As shown in Fig. 3.2(e2), the B19′ phase grows by migration of a phase boundary (dashed line) with increasing load. When ε reaches ~ 6.6%, a B19′ phase also nucleates at the opposite $\{1\,\bar{1}\,0\}_{B2}$ free surface, Fig. 3.2 (e3), and it grows similarly by migration of a phase boundary. Instability occurs when the two phase boundaries are sufficiently close, producing the second load drop and the final product of a uniform B19′ phase, shown in Fig. 3.2(e4). The monoclinic angle γ is 98° in the central region of the

pillar, while γ increases notably to 109° near the outer boundaries of the cross section due to the free surface effect.

The unloading starts with the B19′ phase. Fig. 3.2 (b) plots the associated stress-strain curve (in red). It comprises two linear parts with an abrupt stress change in between. The Young's modulus of the initial linear unloading is around 142GPa, close to $134\text{GPa} \pm 4\text{GPa}$ as measured from experiments at room temperature [84]. At $\varepsilon \approx 3.5\%$, the B19′ phase is reverted to B19 and finally to B2, causing a sudden change of stress. It is followed by another linear unloading with the associated stress-strain curve overlapping the initial loading one (in blue). When the axial strain is reduced to zero, the stress also becomes zero. Clearly, both the phase and load recoveries indicate that the nanopillar undergoes the pseudoelastic deformation during a loading-unloading cycle. In the experiment of NiTi nanopillars, Frick et al. reported that decreasing diameter inhibits the pseudoelastic behavior and ultimately suppresses it for diameters of less than 200nm [13]. As discussed earlier in the Introduction, this size effect has been ascribed to the suppression of martensitic phase transformation in small samples so as to favor the irreversible deformation mechanism by dislocation plasticity. Nevertheless, our pseudoelastic results do not conflict with their findings. This is because in our strain-controlled MD simulations, the realization of pseudoelasticity, through the B19′ $\rightarrow$ B2 phase transformation during unloading, actually requires the negative compressive (i.e. tensile) stress that has not been generally imposed in experiments of nanopillar compression [13]. If the unloading was stopped at zero stresses as experiment, the phase transformation would not be fully reversible, since the final product would be the B19′ martensite instead of the B2 austenite. Lastly, it is important to emphasize that the

chemical effect, i.e., formation of surface oxides, could play an important role in the loss of pseudoelasticity in the experimentally studied NiTi nanopillars. NiTi alloys can be spontaneously covered by a thin film of TiO_2+TiO_x [85, 86], with thickness typically in the range of a few tens of nanometers. San Juan et al. [87] pointed out that in NiTi nanopillar, such oxides will exhibit high modulus and compressive strength, thus acting as a stiff outer tube to enclose the NiTi inner core. As a result, much higher loads would need to be applied to deform the nanopillar, achieving the stress for plastic deformation of the NiTi core and potentially suppressing the pseudoelastic behavior, and in particular pseudoelastic recovery. In the future, it would be highly desired to study the influence of the surface oxides in NiTi nanopillars by atomistic modeling, but it is beyond the scope of this work as the Ni-Ti-O interatomic potential is currently not available.

3.3.2 Irreversible twinning and loss of pseudoelasticity

To study the irreversible deformation in NiTi martensite, we apply a larger range of compressive strain up to 10.6%. The corresponding stress-strain curve is shown in Fig. 3.3 (a), where the loading regime between point (I) and (II) represents the successive phase transformation of B2 → B19 → B19′, as described in section 3.3.1. In this section we focus on the subsequent deformation behavior. Upon continual compression, the B19′ phase at point (II) is not stable, and it immediately transforms to the BCO phase [48] without an obvious change in the stress-strain curve. Fig. 3.3(b) shows the cross-sectional view of the nanopillar with the BCO phase. One major difference between the BCO and B19′ phase is the monoclinic angle γ, i.e. 108° in BCO versus 98° in B19′ as schematically indicated in Fig. 3.3(c) and Fig. 3.2(c), respectively. It should be emphasized that γ in BCO cannot be an arbitrary value, because the orthorhombic

structure dictates $\gamma = \arcsin(a/2c)$, as illustrated in Fig. 3.3(d) [48]. Incidentally, the *ab initio* calculations show that the BCO phase in NiTi is the ground state under zero stresses at 0K, with its energy lower than that of B19′, the commonly observed martensitic phase in experiments [44, 45, 48]. Note that the formation of the BCO phase in our MD simulations is driven by the applied mechanical loading at finite temperature.

Deformation twinning occurs when the applied compressive strain reaches ~ 8.5%, causing a sharp load drop from 5GPa to 0.6GPa, i.e. from point (III) to (IV) in Fig. 3.3 (a). Fig. 3.3 (e) shows the nucleation and growth of a twinned shear band in the martensitic BCO phase. Our analysis of the crystallography and structure changes indicates that the twin plane is $\{112\}_{B2}$, as highlighted by the shaded plane in a BCO unit cell in Fig. 3.3(c) as well as the plane enclosed by the blue dashed lines in Fig. 3.1. The direction of twin shear does not appear to coincide with any typical crystallographic orientation. Such shear transformation is considered as type I twining.

Next, we fully unload the sample to zero strain. The unloading stress-strain curve is shown in Fig. 3.3(a) (in red). Compared to Fig. 3.2(b), an abrupt load change similarly occurs due to the phase transformation of BCO → B2. However, a major difference is the residual tensile stress of ~1.4GPa left in the nanopillar at zero strain, indicating a loss of pseudoelasticity. As shown in Fig. 3.3(f), the initial B2 phase has been recovered after unloading, but the twinned shear band remains in the final product. It is interesting to note that during the loading-unloading cycle, the system undergoes a series of B2 → B19 → B19′ → BCO → B19→ B2 phase transformations that finally recover the initial B2 austenite. However, the deformation twin is irreversible, leading to a loss of pseudoelasticity.

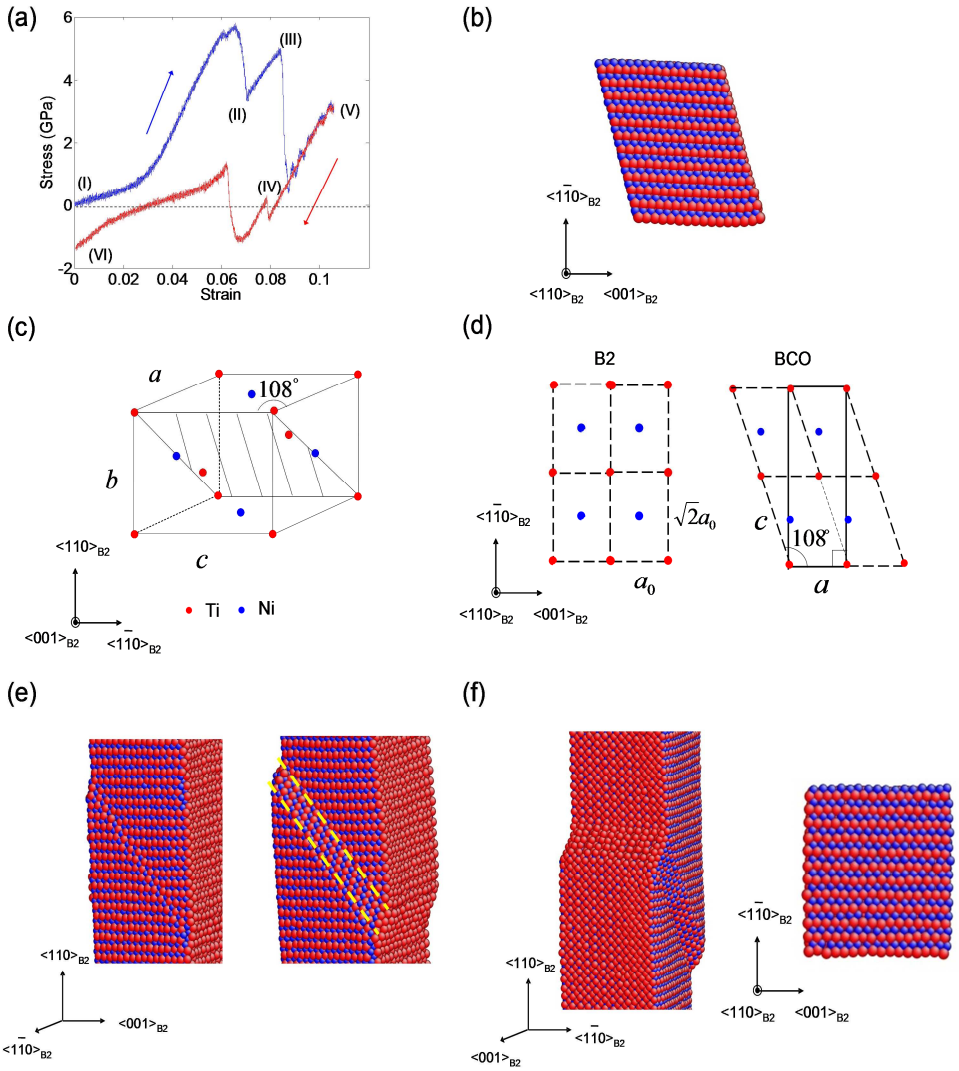

Fig. 3.3. Nanopillar compression at 400K with the applied strain up to 10.6%. (a) Stress-strain curve of loading (blue) and unloading (red). (b) Cross-sectional view of nanopillar, showing the martensitic BCO phase. (c) Schematic of a BCO unit cell. (d) 2D projection of B2 and BCO unit cells, showing the uniquely defined monoclinic angle $\gamma = \arcsin(a/2c) = 108^\circ$ in BCO unit cells. (e) Compressed nanopillar in the BCO phase, showing the formation (left) and growth (right) of a twinned shear band in between

dashed lines. (f) Nanopillar after unloading to zero strain, showing the residual twinned shear band (left) and the cross-sectional view of the B2 phase (right).

The above irreversibility of deformation twining can be attributed to the dislocation pinning effect on twin boundaries. Twins in the B19′ phase are usually reversible in bulk NiTi, as shown in MD simulations of the temperature-driven phase transformation at zero stresses [74]. However, the above deformation twinning in BCO is irreversible and could be caused by the nucleation of dislocations. In the final product containing an irreversible twin shear band, we observed residual dislocations in the $\{112\}_{B2}$ slip plane. This implies that during unloading, those dislocations could act as pinning defects in twin boundaries, preventing the de-twinning process. The irreversible twinning could be further related to the delayed formation of deformation twins in de-confined nanopillars. Namely, the lack of confinement on nanopillars (with the traction-free sidewalls) does not necessarily require the formation of twins at low loads, and the phase transformation to BCO occurs favorably to release the accumulated strain energy with increasing deformation instead. It follows that the deformation twining is postponed to a late stage of loading when the applied stress is considerably high (~ 5GPa). As a result, the high stress could trigger both twinning shear and dislocation nucleation concomitantly. Upon further unloading, the reverse load cannot eliminate these dislocations that act as pinning defects to impede the motion of twin boundaries, thus causing the irreversibility at 400K. Finally, we note that the above MD results are qualitatively similar with different initial distributions of randomly assigned atomic velocities.

3.3.3 Temperature effect and reversible twinning

To study the temperature effect on phase transformation and deformation twinning in NiTi nanopillars, we lower the deformation temperature from 400K to 350K, close to A_f. MD simulations are performed with various initial conditions of randomly-generated atomic velocity distribution, yielding different final products. This implies the thermomechanical response of NiTi nanostructures near the phase transformation temperature could become less deterministic than that at high temperatures. During loading, all the nanopillars undergo the phase transformations of B2 → B19 → BCO at 350K, in contrast to B2 → B19 → B19′ → BCO at 400K. In addition to phase transformations, two different kinds of twin microstructures, i.e., type I twin and 'twins within twin', form in the nanopillars when further loaded at 350K. Similar to results in section 3.3.2, type I twin is also irreversible due to the nucleated dislocations that pin the twin boundaries, and it is not further discussed for brevity. Here we focus on the newly observed 'twins within twin', which are fully recoverable after unloading. As a result, both shape memory and pseudoelastic behaviors can be observed.

Fig. 3.4 shows a MD result at 350K, exhibiting the reversible twins within twin and shape memory effect. Starting with the B2 phase, the transformation to B19 occurs at the strain of 0.7%, much smaller than the corresponding strain of 2.5% at 400K. This difference is understandable, because the low temperature encourages formation of the martensite. As the compressive strain reaches 4%, a direct transformation of B19 → BCO occurs at 350K, instead of B19 → B19′ → BCO at 400K. Fig. 3.4 (b) shows the cross-sectional view of the nanopillar in the BCO phase. Despite the apparently twinned outer boundaries, the sample is actually a single phase without twins, as evidenced by the

perfect periodicity of unit cells (yellow parallelograms) in the entire system. Interestingly, it is a macroscopically twinned structure without the microscopically twinned lattice. Such type of structure arises because the orthorhombic BCO phase possesses both the mirror and central symmetries.

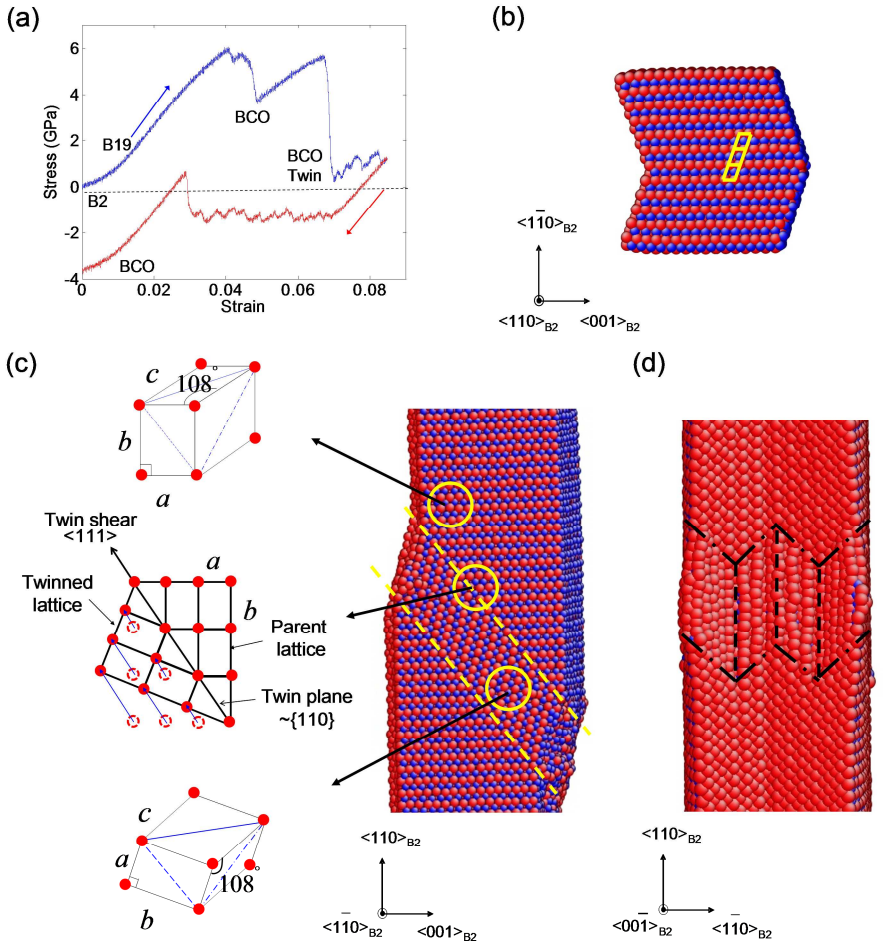

Fig. 3.4. Nanopillar compression at 350K, exhibiting the shape memory behavior. (a) Stress-strain curve of loading (blue) and unloading (red). (b) Cross-sectional view of the compressed nanopillar, showing a single BCO phase (uniform unit cells in yellow lines) in the entire system despite the apparently twined outer boundary. (c) 'Twins within twin' formed in a compressed nanopillar. Middle: a primary twin with twin boundaries marked

by yellow dashed lines. Left: schematics of BCO unit cells of twin variants and the shear transformation at the twin boundary. Right: secondary twins (marked by black dashed lines) viewed from the $\langle 00\bar{1} \rangle_{B2}$ direction.

After the phase transformation of B19 → BCO completes, further compression causes the formation of deformation twins in BCO, resulting in a large load drop at the strain of ~ 6.6%. It is interesting to note that a hierarchically twinned microstructure, i.e., twins within twin, develops in the nanopillar. As shown in Fig. 3.4(c), the boundaries of the primary twin, indicated by yellow dashed lines, are on the $\{110\}_{B2}$ plane, close to the orientation with the largest resolved shear stress. Within the twinning shear band, the secondary twins also develop with smaller twin widths. Such a hierarchically twinned microstructure provides an effective means of releasing strain energy, and it also enables an approximate satisfaction of geometry incompatibility across the primary twin boundaries.

During unloading, the hierarchically twinned microstructure shrinks and finally disappears, resulting in a single BCO phase without twins, i.e. recovering the structure prior to formation of deformation twins as shown in Fig. 3.4(b). Specifically, when the applied compressive strain is reduced from 7% to 3%, the width of the primary twin begins to decrease by migration of twin boundaries. Correspondingly, the stress-strain curve in Fig. 3.4(a) exhibits a plateau, indicating a steady-state process of boundary migration that involves a minor variation of the applied stress. At $\varepsilon \approx 3\%$, a discontinuity appears in the stress-strain curve, signifying the strain energy release caused by a complete elimination of the hierarchically twinned microstructure. No dislocation is

observed in this case. After complete unloading to zero strain, the tensile residual stress remains in the nanopillar, suggesting a loss of pseudoelasticity. Since the final product is a single BCO phase without twins, the shape memory can be realized by heating or further tension, and the B2 austenite is then recovered from the BCO martensite.

Fig. 3.5 shows a different MD result at 350K. Compared to Fig. 3.4, it also exhibits the reversible twins within twin, but pseudoelasticity rather than shape memory. The key difference between the two cases is the cross-sectional geometry of the nanopillar when the BCO phase forms during loading, i.e., the parallelogram-shaped (Fig. 3.5(b)) versus twinned outer boundary (Fig. 3.4(b)). As a result, upon complete unloading to zero strain, the BCO phase is fully recoverable to B2, Fig. 3.5(c); and the nanopillar has no residual stress, Fig. 3.5(a). This is a pseudoelastic deformation.

To understand the origin of the above difference in the cross-sectional geometries, we note that there are two equivalent variants that could possibly form after the phase transformation from B2 to BCO. In Fig. 3.4(b) and 3.5(b), two BCO variants nucleate from the free surface, one at the top and another at the bottom, and they grow by migration of the respective phase boundary toward each other. If the two variants happen to be in the opposite orientation (as selected randomly by thermal fluctuations), the twinned outer boundary will eventually form, i.e. Fig. 3.4(b). Otherwise, the parallelogram-shaped cross section will develop, i.e. Fig. 3.5(b). Lastly, we note a minor difference in the structure of twins within twin between Fig. 3.5(d) and Fig. 3.4(c), while they are both reversible upon unloading.

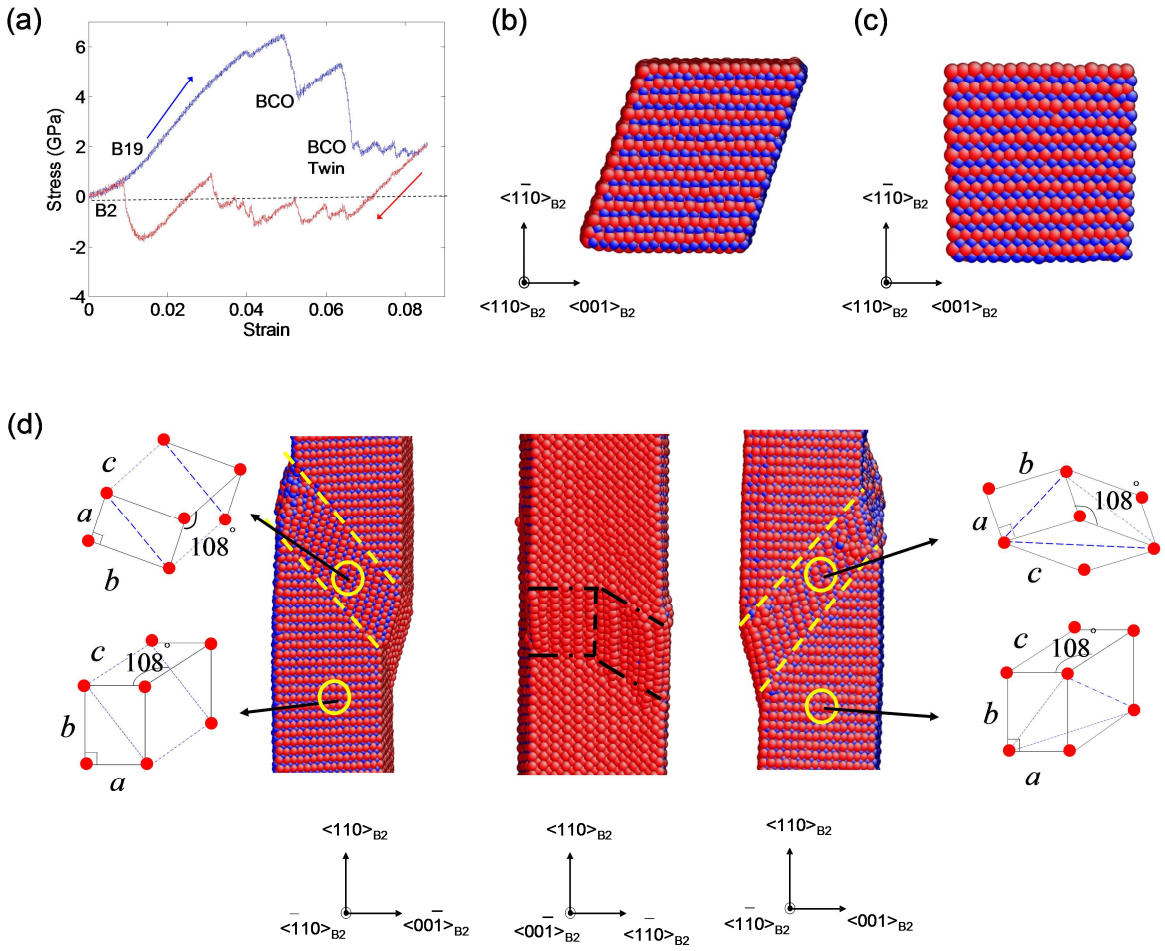

Fig. 3.5. Nanopillar compression at 350K, exhibiting the pseudoelasticity. (a) Stress-strain curve of loading (blue) and unloading (red). (b) Cross-sectional view of the compressed nanopillar, showing a single BCO phase. (c) Final product of the B2 phase in a fully unloaded nanopillar. (d) A different mode of 'twins within twin' formed in the nanopillar, showing three side views with the corresponding BCO unit cells of twin variants.

3.3.4 Size effect

We have studied the size effect on the stress-driven phase transformations in NiTi nanopillars, which appears to be insignificant within the accessible size range. For instance, MD simulations at 400K are performed, with the only difference in the doubled

side lengths of the cross section. The stress-strain curve exhibits no major change; the system similarly undergoes the phase transformations of B2 → B19 → B19′ → BCO; and the deformation twinning mode is also similar. However, the twinned structure is complicated with formation of multiple twinned shear bands, which arise due to the high symmetry of the loading orientation, as well as the large volume that promotes strain accommodation by multiple twins.

Compared to the coarse-grained NiTi alloys, the nanometer size effect can be appreciated in terms of the characteristic stress-strain behaviors of NiTi nanopillars, such as the load serration, stress plateau, and large hysteresis loop as revealed by MD simulations. During loading, the system has to be over-driven to accumulate a large amount of strain energy in order to overcome the nucleation barriers of phase transformation and deformation twinning in the nearly perfect nanopillar. Those nucleation processes can result in the major load drops to release strain energy, leading to serrations in the stress-strain response. During unloading, the nucleation-controlled reverse phase transformation can similarly produce discontinuities in the stress-strain curve. To understand the stress plateaus in Fig. 3.4(a) and 3.5(a), we note that when the deformation involves the interfacial migration, the layer-by-layer movement of the twin boundaries can proceed by similar processes of atomic shuffling (as illustrated in Fig. 3.4(c)), thereby requiring a nearly constant driving stress as manifested by the stress plateau. The above considerations also allow us to rationalize the large hysteresis loop, as evident in Figs. (3.3-3.5). On one hand, the nucleation-controlled processes during loading/unloading require the large forward/reverse transformation stresses. On the other hand, while the migration of twin boundaries during unloading is relatively easy

compared to nucleation, it still requires a large load reversal, giving a low value of reverse transformation stress. This is because in nano-sized systems, there is typically a lack of self-sustaining 3D mechanisms (e.g., pole dislocations) to facilitate the easy movement of twin boundaries that could prevail in the coarse-grained NiTi alloys. As a result, the large hysteresis loop should feature the stress-strain curve of the nanoscale shape memory alloys, as experimentally shown in Cu-Ni-Al nanopillars [14].

In addition, we have studied the size effect on the temperature-driven martensitic phase transformation by comparing the cooling response of a bulk crystal and a nanopillar at zero stresses. In the bulk NiTi subjected to periodic boundary conditions, the martensite start temperature M_s is 310 K and the finish temperature M_f is 290 K. However, in nanopillars, no phase transformation of B2 → B19′ has been observed even when the temperature is lowered to 200K. Such a size effect is likely related to the phase energy differences between atoms at the free surface and in the bulk. It is noteworthy that a recent atomistic study of NiTi nanoparticles by Mutter and Nielaba [76] showed that the size effect also exists in the austenite transformation: the smaller the nanoparticle, the lower the temperatures of A_s and A_f. This trend appears to be consistent with our MD results of the lowered phase transformation temperatures with decreasing pillar size. They attributed the size effects to the increasing role of surface atoms on phase transformation with decreasing particle size [76]. This size effect on the temperature-driven martensitic phase transformation exhibits the similar trend as polycrystalline NiTi [9], where the martensitic phase transformation is suppressed when the grain size is smaller than 60nm.

3.4 Conclusions

The molecular dynamics simulations of $\langle 110 \rangle_{B2}$-oriented NiTi nanopillars have revealed the atomistic mechanisms governing the pseudoelasticity and shape memory in NiTi nanostructures. The major findings of this work are summarized as follows:

At high temperatures (e.g. ~ 50K above the austenite finish temperature) and low loads (e.g. compressive strain up to 6.6%), pseudoelasticity dominates during the loading-unloading cycle. Imposing a higher load will lead to loss of pseudoelasticity, owing to the dislocation pinning of twin boundaries that leads to the irreversibility of deformation twinning.

The thermomechanical responses of NiTi nanostructures become less deterministic as the temperature decreases to around the austenite finish temperature. Both phase transformation and deformation twinning could be reversible or irreversible at high loads (e.g. compressive strain up to 10%). Only when both are reversible, pseudoelasticity is realized. If only the deformation twinning is reversible, as facilitated by the formation of a hierarchically twinned microstructure, shape memory ensues.

The molecular dynamics results also reveal the load serration, stress plateau and large hysteresis loop in the stress-strain curves of NiTi nanopillars. These characteristics have been rationalized in terms of the nucleation-controlled phase transformation and deformation twinning, as well as the migration of phase boundaries, in nano-sized volumes. It was suggested that the large hysteresis loop could be potentially utilized to provide ultrahigh mechanical damping for applications in nano/micro-devices [14].

Finally, we note that the molecular dynamics are limited in the simulation timescale, such that they could not be quantitatively compared with experimental measurements.

While some of the atomic processes revealed in this work could be specific to the model system, the mechanisms and insights concerning the reversible/irreversible phase transformation and deformation twinning should be useful for understanding the pseudoelasticity and shape memory behavior in the nanostructured shape memory alloys.

CHAPTER 4

PATTERNING AND BRANCHING OF MARTENSITIC NANOTWINS

4.1 Introduction

The phase-change materials, such as shape memory alloys [4], ferroelectrics [88] and other multiferroics [89] are being increasingly used for a variety of multifunctional applications. In these materials the twinned martensite is often observed [90]. Understanding the formation and evolution of the martensitic twinned microstructure is crucial for the control of its functional properties, for example, producing large strains in response to the thermomechanical stimuli in shape memory alloys.

Various theoretical and modeling approaches have been applied to study the martensitic microstructure, including the crystallographic and geometrically nonlinear theory [4, 7], phase field simulation [91, 92], as well as the atomistic molecular dynamics [74, 75] and quantum mechanical calculation [17, 39]. While those studies have greatly advanced our understanding of twinned martensite [90], they often require a priori assumptions on the phase transformation geometry and energy function, or are limited in the spatial-temporal resolution. We report a novel atomistic modeling of nanotwinned martensite by using the Monte Carlo (MC) method. Without geometrical construction and timescale limitation, our MC simulations reveal the patterning and branching of nanotwins in a model system of NiTi thin film. The results generate insights into the length scale and temperature effects on the formation of nanotwinned martensite.

4.2 Methods

As discussed in Chapter 2 and 3, a many-body Finnis-Sinclair [58] type interatomic potential is employed to describe the NiTi system. This potential was originally developed by Lai and Liu [31], and later improved to smooth the discontinuities at its cutoff [74]. Canonical Monte Carlo simulations following the Metropolis algorithm [93] are performed to study the temperature-driven martensitic transformation and formation of twinned microstructures. We construct a NiTi thin film in the austenitic B2 phase. The system is $5.1\text{nm}\times 4.8\text{nm}$ wide in the film plane and 16.8nm thick, involving a total of 23,040 atoms. Periodic boundary conditions are applied along both $\langle 001\rangle_{B2}$ and $\langle 1\bar{1}0\rangle_{B2}$ directions within the film plane. The top surface is free to move in the vertical $\langle 110\rangle_{B2}$ direction. Four bottom layers are fixed to the parent B2 phase, mimicking the constraint of the austenitic substrate.

The martensitic phase transformation starting temperature (M_s) in this model system of NiTi thin film has been benchmarked to be around 260K, lower than the bulk value of M_s ~ 310K predicted in Chapter 2 [74]. This difference can be attributed to the boundary effects. Namely, the atomic bonding environment at the free surface and fixed bottom is different from that in the bulk of the thin film, leading to a shift of phase transformation temperature. We have performed the MC simulations in a NVT ensemble at various undercooling temperatures. For each temperature, tens of simulations are conducted to identify the possibly different metastable microstructures. Each of MC simulations involves 1.4 billion steps, ensuring the converged twin structure and energy. We present the representative MC results at 250K (~ 10K undercooling) and 200K (~

60K undercooling). Simulations at temperatures lower than 200K yield results similar to those at 200K.

4.3 Results and Discussions

Our MC simulations reveal the temperature-driven diffusionless phase transformation from the parent B2 to the martensitic B19 phase in the NiTi thin film at both 250K and 200K. Fig. 4.1(a) shows the schematic of the B2 → B19 transformation in a conventional unit cell. In the parent B2 phase, the cell edge is $\sqrt{2}a_0$ in both $\langle 110 \rangle_{B2}$ and $\langle 1\bar{1}0 \rangle_{B2}$ directions, where a_0 denotes the B2 lattice constant. Upon phase transformation, the B19 phase forms two equivalent variants in the plane of the paper, with $c > \sqrt{2}a_0 > b$; the cell edge in the out-of-plane direction of $\langle 001 \rangle_{B2}$ remains unchanged due to geometrical constraint of the austenitic substrate. Note that the previous molecular dynamics simulations with the similar interatomic potential predicted the B2 → B19′ phase transformation in the NiTi bulk (temperature-driven) in Chapter 2 [74] and nanopillar (stress-driven) in Chapter 3 [94]. In this chapter, the favorable formation of the martensitic B19 phase in the thin film can be attributed to the small film thickness, resulting in the increasing role of free surface and fixed austenitic substrate in selecting the transformation product. Interestingly, the resultant martensitic B19 phase exhibits multiple variants, whose periodic arrangement leads to nanotwin patterning.

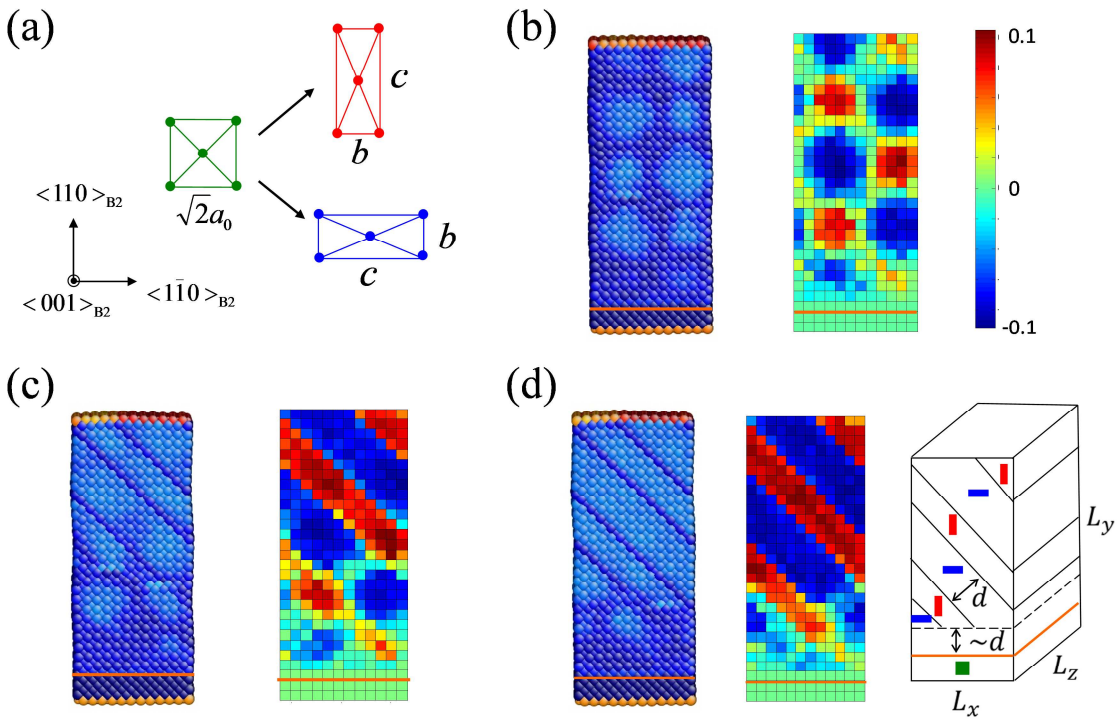

Fig. 4.1 Martensitic transformation and nanotwin patterning in a NiTi thin film at 250K (~ 10K undercooling). The region below the red line is fixed to represent the austenitic substrate. (a) Schematic of the B2 to B19 transformation in a conventional unit cell. The unit cell deformation is exaggerated to increase the geometric contrast of the two B19 variants. (b) MC snapshot showing the initiation of martensitic phase transformation. (b) An intermediate state of formation of twinned martensite. (d) The final converged state with the fully developed periodic twin stripes. In (b-d), the left image shows the atomic configuration where atoms are colored by the von Mises shear strain invariant, and the right one shows the distribution of ratio of the lattice constant in the $<110>_{B2}$ direction over that in $<1\bar{1}0>_{B2}$. In the schematic of twin stripes in (d), the two B19 variants are represented respectively by the red and blue rectangle, and the B2 phase by the green square.

Figs. 4.1 (b-d) show the sequential process of nanotwin patterning at 250K (~ 10K lower than M_s). In Fig. 4.1 (b), the initiation of the B2 → B19 transformation appears to be a homogeneous nucleation process. The atomic configuration on the left shows that the martensitic B19 phase emerges as equally spaced circular nuclei, each of which involves a group of light blue atoms with a diameter about 1.5 nm. In the corresponding color map on the right, it is seen that the nuclei with the same B19 variant (i.e., same color) are neighbored in the 45° direction. Those nuclei grow and coalesce to form the inclined twin stripes. Fig. 4.1 (c) shows an intermediate state, and Fig. 4.1 (d) the final converged structure of twinned martensite. Notice that the above sequence represents a transformation path from an initial state to the mode of the stationary distribution along the Markov chain, and it does not necessarily reflects the temporal evolution of martensitic phase transformation. A number of repeated MC simulations at 250K all yield the same final product.

Both the atomic configuration and color map in Fig. 4.1(d) reveal the periodic stripes of nanotwins, featuring the atomically sharp twin interface with its normal in the $\langle 100 \rangle_{B2}$ direction. Of particular note are the different twin widths in the periodic nanotwinned stripes, i.e., ~ 1.5 nm for variant I (red stripe), and ~ 2.0 nm for variant II (blue stripe). Correspondingly, the volume fraction of variant I, denoted as λ, is 0.42. This volume fraction can be readily rationalized on the basis of the geometrical compatibility requirement at the habit plane between the martensitic twins and austenitic substrate,[4] i.e., $\lambda\beta + (1-\lambda)\gamma = 1$, where $\gamma = c/(\sqrt{2}a_0)$ and $\beta = b/(\sqrt{2}a_0)$.

It should be emphasized that nanotwins near the substrate are not in their equilibrium states, as evidenced by the blurred von Mises shear strain plot and color map in Fig. 4.1(d). This so-called transformation decay region results from the accommodation of lattice mismatch between the austenitic substrate and twinned martensite. Such a decay region plays a key role in selecting the size of the nanotwin stripes. That is, the nanotwin width is governed by the competition between the strain energy in the decay region and the twin interface energy in the film. Incidentally, a similar energy competition leads to periodic stripes in the strained liquid crystal elastomer, and a scaling analysis of stripe width has been given by Terentjev and coworkers [95]. Along the same line of reasoning, we note that the size of the decay region is proportional to the twin width d, since the lattice distortion from the equilibrium B19 state (being either of the two B19 variants) is periodic in the L_x direction with a period of order of d, as indicated in Fig. 4.1(d). Hence the strain energy per stripe is ~ $\mu\varepsilon^2 d^2 L_z$, where μ is the shear modulus and ε is the characteristic lattice strain in the stripe. There are L_x / d stripes in the film. As a result, the total elastic energy in the decay region is $\sim \mu\varepsilon^2 L_x L_z d$. On the other hand, the total interfacial energy associated with twin boundaries is $\sim f_{\mathrm{TB}} L_x L_y L_z / d$, where f_{TB} is the twin boundary energy per unit area. Minimization of the sum of the above elastic and interfacial energies with respect to d yields the optimal twin width

$$d \sim \sqrt{\frac{f_{\mathrm{TB}}}{\mu\varepsilon^2} L_y} \tag{4.1}$$

The scaling relation of Eq. (4.1) makes transparent the physical factors governing the characteristic twin width. It depends on the geometric mean of two length scales: one is

the extrinsic sample length scale of the film thickness L_y; the other is the intrinsic material length scale of $\xi \equiv f_{TB}/(\mu\varepsilon^2)$ that scales with the twin boundary thickness [95]. Using the typical values of NiTi martensite [74], $f_{TB} \sim 0.1\text{J/m}^2$, $\mu \sim 50\text{GPa}$, $\varepsilon \sim 0.05$, we estimate $\xi \sim 1\text{nm}$. Given $L_y = 16.8\text{nm}$ in our MC simulations, Eq. (4.1) predicts the twin width d in the range of a few nanometers, consistent with our MC results. Moreover, since μ increases with decreasing temperature and it usually has a stronger temperature dependence than f_{TB} [95], Eq. (4.1) suggests that an increase of undercooling can lead to twin refinement. This has been verified in our MC simulations, to be detailed next.

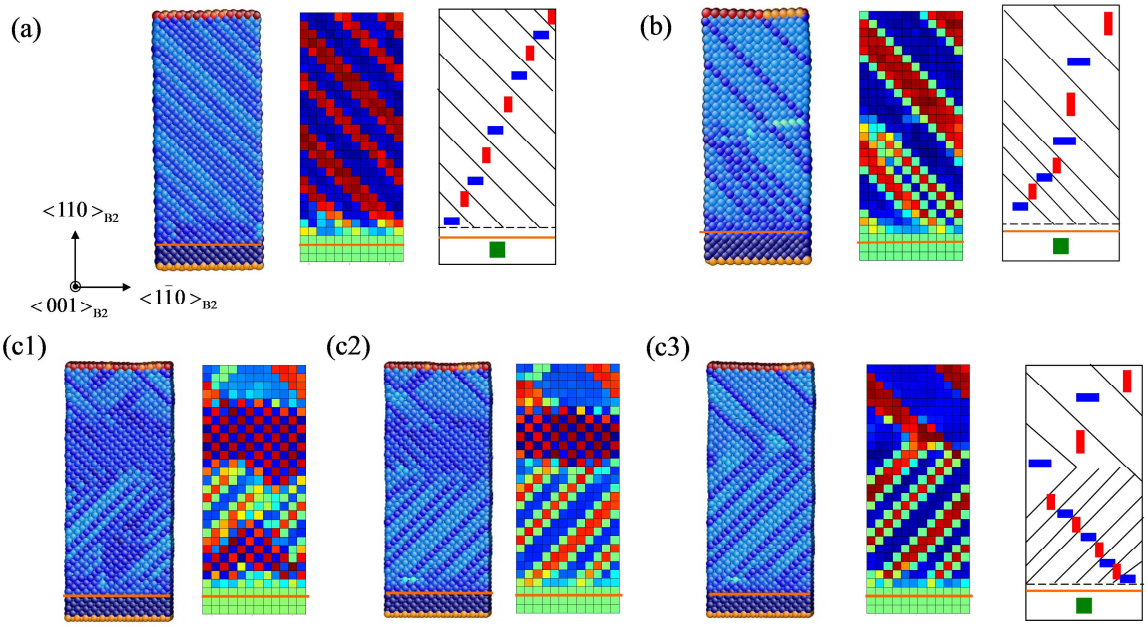

Fig. 4.2 Refinement and branching of nanotwins at 200K (~ 60K undercooling). (a) The final converged state showing the refined twin stripes, as opposed to the coarse ones in Fig. 4.1(d). (b) Branched nanotwins with all the twin boundaries are aligned in the same orientation. (c) Sequential process of formation of branched nanotwins. Compared (b),

the branched twin boundaries form in another equivalent $\{100\}_{B2}$ plane. The coloring scheme in (a-c) is the same as in Fig. 4.1.

Large undercooling can yield a variety of patterning in nanotwinned martensite. Fig. 4.2(a) shows the converged martensitic microstructure at 200K. The nanotwinned stripes consist of alternating B19 variants similar to those at 250K, as shown in Fig. 4.1(d). However, the twin width decreases, so does the size of the transformation decay region. This temperature-induced twin refinement is consistent with the prediction from our previous scaling analysis.

More interestingly, repeated MC simulations reveal the branching of nanotwins near the habit plane between the martensitic twins and austenitic substrate. One scenario of twin branching is shown in Fig. 4.2(b), where the coarse twins appear near the free surface and fine twins, aligned in the same orientation, occur when approaching the habit plane. Alternatively, the fine twins could form with twin boundaries in another equivalent $\{100\}_{B2}$ plane, as shown in Fig. 4.2(c3). This produces an intriguing pattern of "twins within twins" [90], with the primary twin interface of $\{110\}_{B2}$ and the secondary twin interfaces of $\{100\}_{B2}$.

The branched nanotwins in Fig. 4.2(b-c) are likely more favorable energetically than the non-branched ones in Fig. 4.2(a). Along the line of previous analysis of the energy competition in twinned martensite, it is understandable that the energy budget could be effectively reduced by adopting multiple twin sizes, e.g., the coarse and fine twins coexist, but are located at different places, as shown in our MC simulations. The fine twins near the habit plane lower the elastic energy by reducing the size of the decay

region. On the other hand, the coarse twins near the free surface reduce the overall twin interfacial energy.

Fig. 4.2 (c1-c3) shows the sequential process of nucleation and growth of the branched nanotwins, with their converged state in Fig. 4.2(c3). In contrast to the homogenous nucleation of martensite within the bulk of the thin film at 250K in Fig.4.1(b), the martensitic nanotwins nucleate simultaneously near the free surface and substrate at 200K. They exhibit different twin widths and grow to meet inside the thin film, yielding the final product in Fig. 4.2(c3). The geometrical constraints near the free surface and habit plane are distinctly different, setting the different characteristic twin sizes. The apparent branching of nanotwins actually results from the simultaneous nucleation of nanotwins from both the free surface and habit plane. Different branching modes in Fig. 4.2(b-c) originate from random selection of the orientation of nanotwins when they are initiated.

4.4 Conclusions

In summary, we perform the Monte Carlo simulations to study the patterning of martensitic nanotwins at the atomic scale, without geometrical construction and timescale limitation. Our results show that large undercooling can lead to the refinement and branching of nanotwins. We use a scaling law to make transparent the physical effects governing the characteristic twin width. This work opens up the possibilities of predictive modeling of the martensitic twinned microstructures down to the atomic scale.

CHAPTER 5

PHASE FIELD MODELING OF MARTENSITIC MICROSTRUCTURE IN NITI

5.1 Introduction

The martensitic phase transformation in NiTi has been studied by a variety of modeling approaches. The continuum models are usually focused on the crystallography and compatibility of phase transformation and twin microstructure [7, 40, 41, 96]. First principles calculations are well situated to investigate the atomic-level structures and their stabilities, as well as phase transformation paths and size effects, at zero Kelvin [17, 39, 44, 45, 48]. As discussed in Chapter 2-4, atomistic studies based on the empirical interatomic potential can explore the phase transformation and martensitic microstructures at finite temperatures in systems larger than those accessed by the first principles methods [74-76, 94, 97]. However, both the first principles and interatomic potential-based studies are severely limited by the achievable spatial-temporal scale. Such limitation can be alleviated by the phase field model that is particularly suitable for the study of dynamic evolution of martensitic microstructure [91, 98-100].

The NiTi system generally involves a variety of metastable phases (B2, B19, B19′ and R etc.), martensite variants (e.g. twelve variants in B19′ martensite) and twin structures (such as type I, II and compound twin). This poses significant challenges to the modeling. Nevertheless, encouraging progress has been recently made in the development of phase field models for the NiTi system. For example, Shu and Yen developed a multi-variant model to study a relatively simple mode of R phase

transformation [92]. Yang and Dayal proposed a simple energy function to describe the B19′ multi-variants of NiTi [101]. Both models assumed the penalty-based energy function and were applied to two-dimensional phase filed simulations. However, the phase field model with the physics-based Landau-type energy function is still unavailable. The Landau-type polynomial energy function is generally favored in the phase field model, as it facilitates an explicit link between the model parameters with the physical properties such as overcooling temperature. Constructing the Landau-type polynomial energy function is non-trivial, because it requires the co-existence of thirteen local metastable energy wells that respectively correspond to the parent B2 phase and twelve martensitic B19′ variants; meanwhile other metastable energy wells should be eliminated to avoid the interference of physically irrelevant states. In this work, we construct an effective Landau-type polynomial energy function, and perform the three-dimensional phase field simulations of B2 to B19′ phase transformation. Results reveal nucleation and growth of polytwinned morphology of martensitic microstructures.

5.2 Methods

We take a single crystal of B2 austenite as the start configuration. This parent austenitic phase can transform to the B19′ martensite when the temperature is reduced below the martensite start temperature. The phase field modeling provides the solutions of the temporal evolution of phases and microstructures by numerically solving the time-dependent partial differential equations of the field variables. Twelve continuous field variables $\eta_1, \eta_2, \cdots, \eta_{12}$ between zero and one are defined to describe the B2 to B19′ transformation, which involves twelve possible B19′ variants. Austenite is described if all

$\eta_1 = \eta_2 = \cdots = \eta_{12} = 0$, and martensite with variant *i* is described if $\eta_i = 1$ and $\eta_j = 0$ for all $j \neq i$.

The stress-free strain, which comes from the locally inhomogeneous martensitic phase transformation, can be characterized as

$$\boldsymbol{\varepsilon}^*(\boldsymbol{x}) = \sum_{i=1}^{12} \eta_i(\boldsymbol{x})\boldsymbol{\varepsilon}_i^0 \tag{5.1}$$

where the stress-free strain tensor at spatial coordinate $\boldsymbol{x}$ is the summation of each field variable η_i multiplied by the B2 to B19′ transformation strain tensor $\boldsymbol{\varepsilon}_i^0$ for each corresponding martensitic variant *i*.

The free energy of the system can be described by the volume integral of free energy density, which contains the local specific free energy density f_{local}, interfacial energy density f_{int} , and the strain energy density f_{ela}.

$$\boldsymbol{F} = \int_V (f_{local} + f_{int} + f_{ela})\, d^3r \tag{5.2}$$

5.2.1 Local specific free energy

The local specific free energy density f_{local} is contributed by the bulk thermodynamics properties of the system. A Landau-type polynomial has been applied to approximate the local specific free energy f_{local} as

$$f_{local} = f_0 + \Delta f(T)\left\{\frac{1}{2}A(\sum_{i=1}^{12}\eta_i^2) - \frac{1}{3}B(\sum_{i=1}^{12}\eta_i^3) + \frac{1}{4}C(\sum_{i=1}^{12}\eta_i^2)^2 + \frac{1}{4}D(\sum_{i=1}^{12}\eta_i^4)\right\} \tag{5.3}$$

where f_0 represents the free energy density of the austenitic phase, $\Delta f(T)$ is the free energy density between austenite and martensite, which depends on the temperature *T*, and *A*, *B*, *C* and *D* are constants describing the shape of free energy density function.

The parameters *A*, *B*, *C* and *D* in Eq. (5.3) cannot be arbitrarily assigned. Two constraints must be satisfied. Firstly, the partial derivative of f_{local} with respect to all the field variables $\eta_1, \eta_2, \cdots, \eta_{12}$ must be zero for all the austenite and martensite phases. Secondly, the free energy density difference between austenite and martensite should be $\Delta f(T)$. These requirements lead to

$$\begin{cases} -A + B - C - D = 0 \\ \frac{1}{2}A - \frac{1}{3}B + \frac{1}{4}C + \frac{1}{4}D = -1 \end{cases} \tag{5.4}$$

In this work we choose parameters of $A = 1$, $B = 15$, $C = 7$ and $D = 7$ for f_{local}. The driving force on the field variable η_i associated with f_{local} is

$$F_i^{local} = -\frac{\partial f_{local}}{\partial \eta_i} = \Delta f(T)\left\{-A\eta_i + B\eta_i^2 - C\eta_i\left(\sum_{j=1}^{12}\eta_j^2\right) - D\eta_i^3\right\} \tag{5.5}$$

5.2.2 Interfacial energy density

The interfacial energy density f_{int} is the nonlocal part of the chemical free energy density. We express f_{int} in terms of the gradient of the field variables

$$f_{int} = \frac{1}{2}\sum_{p=1}^{12}\beta_{ij}(p)\frac{\partial \eta_p}{\partial x_i}\frac{\partial \eta_p}{\partial x_j} \tag{5.6}$$

where the Einstein summation convention is applied only for subscript *i* and *j*. In Eq. (5.6), the coefficients $\beta_{ij}(p)$ are the components of a semi-positive definite tensor. They are not necessarily the same among different field variables η_p, and may be anisotropic depending on the direction of the gradient given by the partial difference with respect to the spatial coordinates x_i and x_j. To capture the essential phase effects with reduced complexity, we consider the isotropic interfacial energy in this work. Namely, we take $\beta_{ij}(p) = \beta\delta_{ij}$, where δ_{ij} is the Kronecker's delta. Then Eq. (5.6) becomes

$$f_{int} = \frac{1}{2}\sum_{p=1}^{12}\beta|\nabla\eta_p|^2 \tag{5.7}$$

The driving force on the field variable η_i associated with f_{int} is

$$F_i^{int} = \beta\nabla^2\eta_i \tag{5.8}$$

5.2.3 Elastic energy density

The elastic energy density can be determined by the total strain minus the stress-free strain defined above

$$f_{ela} = \frac{1}{2}(\boldsymbol{\varepsilon} - \boldsymbol{\varepsilon}^*)^T \cdot \boldsymbol{C} \cdot (\boldsymbol{\varepsilon} - \boldsymbol{\varepsilon}^*) - \boldsymbol{\sigma}_0{}^T \cdot \boldsymbol{\varepsilon} \tag{5.9}$$

Where $\boldsymbol{\sigma}_0$ is the external applied stress, and the total strain and non-elastic strain $\boldsymbol{\varepsilon} = (\varepsilon_{11},\ \varepsilon_{22},\ \varepsilon_{33},\ 2\varepsilon_{23},\ 2\varepsilon_{31}, 2\varepsilon_{12})^T$, $\boldsymbol{\varepsilon}^* = (\varepsilon_{11}^*, \varepsilon_{22}^*, \varepsilon_{33}^*, 2\varepsilon_{23}^*,\ 2\varepsilon_{31}^*, 2\varepsilon_{12}^*)^T$ are in term of the Voigt notation, and the stiffness matrix $\boldsymbol{C}$ is 6 by 6. The constitutive equation can be derived from Eq. (5.9), giving that the stress tensor

$$\boldsymbol{\tau} = (\sigma_{11},\ \sigma_{22},\ \sigma_{33},\ \sigma_{23},\ \sigma_{31}, \sigma_{12})^T = \boldsymbol{C} \cdot (\boldsymbol{\varepsilon} - \boldsymbol{\varepsilon}^*) \tag{5.10}$$

The driving force acting on field variable η_i due to elastic energy density is

$$F_i^{ela} = -\frac{\partial f_{ela}}{\partial \eta_i} = [\boldsymbol{C} \cdot (\boldsymbol{\varepsilon} - \boldsymbol{\varepsilon}^*)]^T \cdot \frac{\partial \boldsymbol{\varepsilon}^*}{\partial \eta_i} + \boldsymbol{\sigma}_0{}^T \cdot \frac{\partial \boldsymbol{\varepsilon}}{\partial \eta_i} = \boldsymbol{\tau}^T \cdot \frac{\partial \boldsymbol{\varepsilon}^*}{\partial \eta_i} + \boldsymbol{\sigma}_0{}^T \cdot \frac{\partial \boldsymbol{\varepsilon}}{\partial \eta_i} \tag{5.11}$$

In this work, the boundary conditions are either strain-controlled or zero-stress applied, indicating the second term in Eq. (5.11) can be dropped. Note that the total strain $\boldsymbol{\varepsilon}$ and stress $\boldsymbol{\tau}$ needs to be numerically solved during the simulation. Please see appendix B for the details.

5.2.4 Stochastic Phase Field Kinetic Equation

The evolution of the field variables is governed by the time-dependent Ginzburg-Laudau (TDGL) equation, which is a stochastic phase field kinetic equation that assumes

the rate of the evolution of the field variables is proportional to the thermodynamics driving force.

$$\frac{\partial \eta_i}{\partial t} = \sum_{j=1}^{12}\left[\hat{L}_{ij}\left(F_j^{local} + F_j^{int} + F_j^{ela}\right)\right] + \xi_i(\boldsymbol{x}, t) \qquad (5.12)$$

where $\hat{L}_{ij}$ is the kinetic coefficient matrix and $\xi_i(\boldsymbol{x}, t)$ is the Langevin noise term. The Langevin noise term $\xi_i(\boldsymbol{x}, t)$ is a random variable as a function of location and time, which follows the normal distribution and mutually independent at different locations and time. To satisfy the requirement of fluctuation-dissipation theorem, the correlation of $\xi_i(\boldsymbol{x}, t)$ is given by:

$$\langle \xi_i(\boldsymbol{x}, t)\xi_j(\boldsymbol{x}', t')\rangle = 2k_B T\hat{L}_{ij}\delta_{ij}\delta(\boldsymbol{x} - \boldsymbol{x}')\delta(t - t') \qquad (5.13)$$

where k_B is the Boltzmann constant, *T* is the temperature, δ_{ij} is the Kronecker delta, and δ is the Dirac delta function. For simplification, the kinetic coefficient $\hat{L}_{ij}$ is given to be diagonal, i.e. $\hat{L}_{ij} = L\delta_{ij}$, with the assumption that the driving force on the field variable η_i has no concurrent effect on the evolution of field variable η_j when $i \neq j$. Substitution of Eq. (5.5), (5.8) into Eq. (5.12) yields

$$\frac{\partial \eta_i}{\partial t} = L\left\{\Delta f(T)\left[-A\eta_i + B\eta_i^2 - C\eta_i\left(\sum_{j=1}^{12}\eta_j^2\right) - D\eta_i^3\right] + \beta\nabla^2\eta_i + F_{ela}^i\right\} + \xi_i(\boldsymbol{x}, t) \qquad (5.14)$$

5.2.5 Numerical simulation

The phase field simulations are performed in a three-dimensional (3D) cubic cell, with periodic boundary conditions imposed in all three directions. We discretize the 3D spatial domain into uniform grids and the one-dimensional time domain into equal steps. All of the field variables at time step *n* are in the form of $\eta_i^n(\boldsymbol{x}, n\Delta t)$ for $i = 1,2,\cdots,12$, where Δt is the time step size. It is convenient to normalize the length and time scale,

thereby eliminating the unnecessary parameters. We define the dimensionless space coordinate $\tilde{x}_1 = x_1/l_0$, $\tilde{x}_2 = x_2/l_0$ and $\tilde{x}_3 = x_3/l_0$, where l_0 is the length of grid cell, and the dimensionless time $\tilde{t} = tL\Delta f(T)$ and $\Delta\tilde{t} = \Delta tL\Delta f(T)$. It follows that the normalized Eq. (5.14) is

$$\frac{\partial \eta_i}{\partial \tilde{t}} = \left[-A\eta_i + B\eta_i^2 - C\eta_i\left(\sum_{j=1}^{12}\eta_j^2\right) - D\eta_i^3\right] + \tilde{\beta}\tilde{\nabla}^2\eta_i + \frac{F_{ela}^i}{\Delta f(T)} + \tilde{\xi}_i(\tilde{\boldsymbol{x}}, t) \qquad (5.15)$$

where $\tilde{\nabla}^2 = \frac{\partial^2}{\partial \tilde{x}_1^2} + \frac{\partial^2}{\partial \tilde{x}_2^2} + \frac{\partial^2}{\partial \tilde{x}_3^2}$, $\tilde{\beta} = \frac{\beta}{\Delta f(T) l_0^2}$ and $\tilde{\xi}_i(\tilde{\boldsymbol{x}}, t) = \frac{1}{L\Delta f(T)}\xi_i(\tilde{\boldsymbol{x}}, t)$. Random variable $\tilde{\xi}_i(\tilde{\boldsymbol{x}}, t)$, which is mutually independent at different space coordinates and time steps, follows the normal distribution with mean of zero and variance of $\frac{2k_bT}{\Delta f(T) l_0^3}$.

To numerically solve a partial differential equation of heat-equation type, one typically applies the forward Euler method (explicit), backward Euler method (implicit) or Crank-Nicolson method (implicit). The nonlinear terms (the first and third terms in Eq. (5.15)) pose the computational challenge to either the backward Euler or Crank-Nicolson method. On the other hand, the stability condition of the forward Euler method due to the Laplace operator limits the time step size $\Delta\tilde{t} \approx \Delta\tilde{x}^2$. The semi-implicit Fourier-spectral method proposed by Chen and Shen provides an efficient and accurate solution for the TDGL equation [99]. The key of this semi-implicit method is to calculate the Laplace operator implicitly and nonlinear terms explicitly, such that the Eq. (5.15) is discretized to

$$\frac{\eta_i^{n+1} - \eta_i^n}{\Delta\tilde{t}} = \left(\frac{F_i^{local}\left(\boldsymbol{\eta}^n(\boldsymbol{x}, n\Delta t)\right)}{\Delta f(T)} + \tilde{\beta}\tilde{\nabla}^2\eta_i^{n+1}(\boldsymbol{x}, (n+1)\Delta t) + \frac{F_i^{ela}\left(\boldsymbol{\eta}^n(\boldsymbol{x}, n\Delta t)\right)}{\Delta f(T)}\right)$$
$$+\tilde{\xi}_i(\tilde{\boldsymbol{x}}, (n+1)\Delta t) \qquad (5.16)$$

It is more computationally efficient to solve Eq. (5.16) in the Fourier space, so as to avoid the inverse Fourier transformation of stress. The Laplace operator in the real space is transformed to $-4\pi(s_1^2+s_2^2+s_3^2)$ in the Fourier space, where $\boldsymbol{s}=(s_1,s_2,s_3)^T$ is the coordinate in the reciprocal space. Eq. (5.16) can be transformed to

$$\widehat{\eta_l^{n+1}}=\frac{1}{1+4\pi\tilde{\beta}(s_1^2+s_2^2+s_3^2)\Delta\tilde{t}}\cdot\left(\widehat{\eta_l^n}+\frac{\Delta\tilde{t}}{\Delta f(T)}\widehat{F_l^{local}(\boldsymbol{\eta}^n)}+\frac{\Delta\tilde{t}}{\Delta f(T)}\widehat{F_l^{ela}(\boldsymbol{\eta}^n)}\right) \quad (5.17)$$

5.2.6 Model parameters and simulation setup

In Eq. (5.1), the stress-free strain of B2 to B19′ transformation is described by twelve field variables $\eta_1,\eta_2,\cdots,\eta_{12}$, corresponding to twelve B19′ variants. When the global Cartesian coordinate system is aligned with the cubic axes of the parent B2 phase, the twelve transformation strain tensors $\boldsymbol{\varepsilon_i^0}$ $(i=1,2,\cdots,12)$ in Eq. (5.1) are given by

$$\boldsymbol{\varepsilon_1^0}=\begin{pmatrix}\theta&\rho&\rho\\\rho&\sigma&\tau\\\rho&\tau&\sigma\end{pmatrix},\qquad \boldsymbol{\varepsilon_2^0}=\begin{pmatrix}\theta&-\rho&-\rho\\-\rho&\sigma&\tau\\-\rho&\tau&\sigma\end{pmatrix},$$

$$\boldsymbol{\varepsilon_3^0}=\begin{pmatrix}\theta&-\rho&\rho\\-\rho&\sigma&-\tau\\\rho&-\tau&\sigma\end{pmatrix},\ \boldsymbol{\varepsilon_4^0}=\begin{pmatrix}\theta&\rho&-\rho\\\rho&\sigma&-\tau\\-\rho&-\tau&\sigma\end{pmatrix},$$

$$\boldsymbol{\varepsilon_5^0}=\begin{pmatrix}\sigma&\rho&\tau\\\rho&\theta&\rho\\\tau&\rho&\sigma\end{pmatrix},\qquad \boldsymbol{\varepsilon_6^0}=\begin{pmatrix}\sigma&-\rho&\tau\\-\rho&\theta&-\rho\\\tau&-\rho&\sigma\end{pmatrix}, \quad (5.18)$$

$$\boldsymbol{\varepsilon_7^0}=\begin{pmatrix}\sigma&-\rho&-\tau\\-\rho&\theta&\rho\\-\tau&\rho&\sigma\end{pmatrix},\ \boldsymbol{\varepsilon_8^0}=\begin{pmatrix}\sigma&\rho&-\tau\\\rho&\theta&-\rho\\-\tau&-\rho&\sigma\end{pmatrix},$$

$$\boldsymbol{\varepsilon_9^0}=\begin{pmatrix}\sigma&\tau&\rho\\\tau&\sigma&\rho\\\rho&\rho&\theta\end{pmatrix},\qquad \boldsymbol{\varepsilon_{10}^0}=\begin{pmatrix}\sigma&\tau&-\rho\\\tau&\sigma&-\rho\\-\rho&-\rho&\theta\end{pmatrix},$$

$$\boldsymbol{\varepsilon_{11}^0}=\begin{pmatrix}\sigma&-\tau&\rho\\-\tau&\sigma&-\rho\\\rho&-\rho&\theta\end{pmatrix},\ \boldsymbol{\varepsilon_{12}^0}=\begin{pmatrix}\sigma&-\tau&-\rho\\-\tau&\sigma&\rho\\-\rho&\rho&\theta\end{pmatrix}$$

The components of transformation strain in Eq. (5.18) have been calculated by Hane and Shield using the lattice constants given by Otsuka et al., i.e. $\theta = -0.0437$, $\sigma = 0.0243$, $\rho = -0.0427$ and $\tau = 0.0580$ [4, 41]. When the global Cartesian coordinate system is not aligned with the cubic axes of the parent B2 phase, a rotation operation of $\boldsymbol{R}\boldsymbol{\varepsilon}_i^{\mathbf{0}}\boldsymbol{R}^T$ is required, where $\boldsymbol{R}$ is the rotation matrix.

The elastic constant matrix $\boldsymbol{C}$ is determined by the density functional calculations from Hatcher et al., i.e. $C_{11} = 183\text{GPa}$, $C_{12} = 146\text{GPa}$ and $C_{44} = 46\text{GPa}$ [44]. The typical strain energy density (scaled with $\boldsymbol{\varepsilon}_{\mathbf{1}}^{\mathbf{0}^T}\boldsymbol{C}\boldsymbol{\varepsilon}_{\mathbf{1}}^{\mathbf{0}}$, where the vector $\boldsymbol{\varepsilon}_{\mathbf{1}}^{\mathbf{0}}$ is in the Voigt notation) is $4.403 \times 10^8 \text{J/m}^3$. We take the free energy density between austenite and martensite $\Delta f(T)$ to be 10% of the strain energy, i.e., $\Delta f(T) = 4.403 \times 10^7 \text{J/m}^3$. A simple relation between $\Delta f(T)$ and undercooling temperature ΔT is assumed

$$\Delta f(T) = L \cdot \Delta T / T_0 \tag{5.19}$$

In Eq. (5.19), the latent heat is taken as $L = 110\text{MJ/m}^3$, the equilibrium temperature $T_0 = 271\text{K}$ [102, 103], so that the undercooling temperature is $\Delta T = 108K$.

The specific interfacial energy γ (i.e., interfacial energy per area) is related to the coefficient β in Eq. (5.7) according to $\gamma = \frac{4\sqrt{2}}{3}\sqrt{\beta \Delta f(T)}$. We use the normalized interfacial energy coefficient $\tilde{\beta}$ in Eq. (5.15), then the gird size becomes $l_0 = \frac{3\gamma}{4\Delta f(T)\sqrt{2\tilde{\beta}}}$, where γ is taken as the interfacial energy of type I twin, 187mJ/m^2 [17].

The time step needs to be carefully chosen to ensure the numerical convergence. By trial and error, we find that $\Delta\tilde{t} = 0.01$ provides the reasonable accuracy and efficiency. The numerical integration is performed up to 12,500 time steps, i.e. $\tilde{t} = 125$, with no further change of microstructures.

5.3 Results and Discussions

5.3.1 Microstructure evolution

To study the nucleation and growth of martensitic microstructures, we first consider a mixed loading mode: zero in-plane strain and zero out-of-plane stress, i.e. $\varepsilon_1^{app} = \varepsilon_2^{app} = \varepsilon_6^{app} = 0$ and $\tau_3^{app} = \tau_4^{app} = \tau_5^{app} = 0$. Such boundary conditions are typical of thin films subjected to rigid constraints from the substrate. The global Cartesian coordinate system is aligned with the cubic axes of the parent B2 phase. The system contains $64 \times 64 \times 64$ mesh grids. We set $\tilde{\beta} = 2$, so that $l_0 = \frac{3\gamma}{4\Delta f(T)\sqrt{2\tilde{\beta}}} = 1.6nm$. This corresponds to the cubic system with side length of 102.4nm.

Given the positive value of $\Delta f(T)$, the martensitic transformation of B2 to B19′ is energetically favored. However, owing to the metastable state of the B2 phase, the martensitic transformation would not occur spontaneously, thus requiring thermal fluctuations to assist the martensite nucleation. The Langevin noise term $\xi_i(\boldsymbol{x}, t)$ in Eq. (5.12) plays the role of thermal fluctuations. This stochastic term is independent with each other at different time steps or spatial locations, thus does not provide any constraints on the phase transformation process. The stochastic noise term is turned off after 3000 simulation steps when $\tilde{t} = 30$.

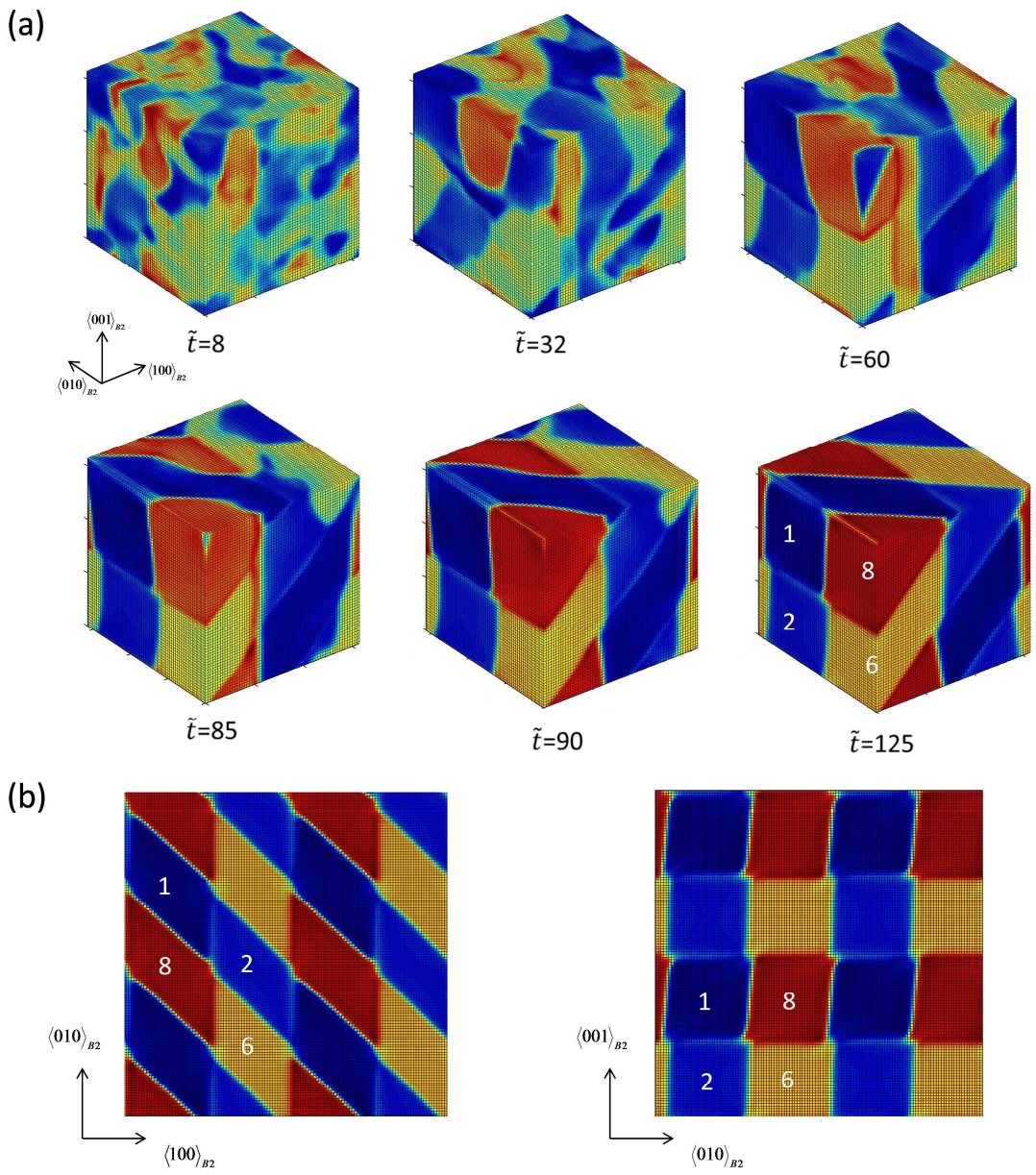

Fig. 5.1. 3D phase field simulation results. (a) Time-elapse snapshots showing the nucleation and growth of polytwinned martensitic microstructures. The mesh grids are colored by $\sum_{i=1}^{12} i\eta_i(\boldsymbol{x})$. (b) The 2D projections of 3D microstructures. For a better visualization of polytwinned microstructures, the simulation cell is periodically doubled in the two in-plane directions.

Fig. 5.1(a) shows the nucleation and growth of martensites and polytwinned pattern. At $\tilde{t} = 8$, precursors of martensite form, driven by the free energy difference and thermal fluctuations. Different colors, representing different values of field variables, show the nucleation of multivariants. At this stage, none of the field variables η_i is close to 1 and no variant is fully formed. However, the field variables also deviate from all-zero values (the metastable B2 phase). Those martensite precursors involve lattice distortion. They form and disappear during this early stage. The microstructure further evolves from the existing lattice distortion promoted by thermal fluctuations, when the stochastic noise terms are turned off at $\tilde{t} = 30$. At $\tilde{t} = 32$, shortly after the stochastic noise terms are turned off, nuclei of size around tens of nanometers are generated. The boundaries of nuclei are curved and no obvious laminate twin structure is visible. The growth and elimination of these nuclei are driven by the local free energy, interfacial energy and elastic energy. The twin-shaped pattern first emerges at $\tilde{t} = 60$, where some of the nuclei, colored by red, blue and green, finally grow to different twin variants. Some of other nuclei disappear at $\tilde{t} = 85$. Soon later at $\tilde{t} = 90$, the twin pattern becomes stable, while the twin boundaries are still not flat planes. Finally at $\tilde{t} = 125$ the three-dimensional twin structure containing four different B19′ variants form with the respective transformation strain of $\boldsymbol{\varepsilon}_1^0, \boldsymbol{\varepsilon}_2^0, \boldsymbol{\varepsilon}_6^0$ and $\boldsymbol{\varepsilon}_8^0$. Fig. 5.1(b) shows the top view and left side view of the final product. The nucleated martensite variants form a novel three-dimensional polytwinned structures. The multivariants are self-accommodating. The average transformation strain is

$$\left(\boldsymbol{\varepsilon}_\mathbf{1}^\mathbf{0} + \boldsymbol{\varepsilon}_\mathbf{2}^\mathbf{0} + \boldsymbol{\varepsilon}_\mathbf{6}^\mathbf{0} + \boldsymbol{\varepsilon}_\mathbf{8}^\mathbf{0}\right)/4 = \begin{pmatrix} -0.01 & 0 & 0 \\ 0 & -0.01 & 0.0504 \\ 0 & 0.0504 & 0.0243 \end{pmatrix} \qquad (5.20)$$

The averaged transformation strain is compatible with the zero in-plane strain boundary conditions.

The in-plane components of the average transformation strain are very small, i.e. 1% compression normal strain and zero shear strain, thus agree very well with the applied zero in-plane strain boundary conditions of $\varepsilon_1^{app} = \varepsilon_2^{app} = \varepsilon_6^{app} = 0$. The 1% difference between normal average transformation strain and zero applied strain increases the homogeneous strain energy. However, since the local free energy for martensite is smaller than the austenite, total energy decreases. Also, compared with the case where single martensite variant nucleates, the self-accommodated twin structures significantly decreases the homogeneous strain energy. For the out-of-plane components of average transformation strain in Eq. (5.20), although the values are relatively larger, they do not increase the homogeneous strain energy under the applied zero out-of-plane stress boundary conditions of $\tau_3^{app} = \tau_4^{app} = \tau_5^{app} = 0$.

The nucleated martensite variants form twins, where the heterogeneous strain energy is minimized if the compatibility requirements are satisfied at twin interfaces. The observed twin planes between each pair of variants $\{2:6\}$, $\{1:8\}$, $\{1:2\}$and $\{6:8\}$ are all $\{110\}$ type of plane, as shown in Fig. 5.1 and summarized in Table 5.1. Three of them are consistent with theoretical solutions of NiTi type I twin, with the exception of the pair of $\{6:8\}$. This exception violates the compatibility of twin interface, and increases short-range energy due to the incompatibility. However, this scarification is necessary to decrease the total energy. Theoretical solution based on compatibility at twin interfaces [41] provides a general guide line of twin structures when applied far-field stress are zero, but it is inefficient under other boundary conditions. Under stricter conditions, such

as zero applied strain and periodic boundary conditions, there might be no "perfect" solution which is fully compatible at twin interface (decrease heterogeneous strain energy) as well as minimize the free energy (chemical energy) and homogeneous energy. Scarification is necessary. Phase field simulations show the compatibility at twin interfaces is not always guaranteed.

Table 5.1. Compatibility of twin variants obtained in phase field simulations and given by continuum based solutions.

Pair	Theoretical Solution [41]	Phase Field
$\{2:6\}$	$\{110\}$ type I	$\{110\}$
$\{1:8\}$	$\{110\}$ type I	$\{110\}$
$\{1:2\}$	$\{110\}$ compound	$\{110\}$
$\{6:8\}$	$\{100\}$ type I	$\{110\}$

The martensitic phase transformation in a complicate system containing multiple martensite variants such as NiTi could yield many different final products. We repeat our simulation with all the parameters unchanged to explore the different possible microstructures. Figure 5.2(a) show the martensite nucleation and microstructures evolution process. The precursors of martensite form and disappear similarly with the results above. At $\tilde{t} = 50$, nuclei form and migrate to each other containing same twin variants, and finally form the twin structures at $\tilde{t} = 125$. The formed twin structures are in a two-dimensional shape. The top view of the final products are shown in Figure 5.2(b), containing four different B19′ variants with the basis transformation strain $\boldsymbol{\varepsilon}_2^0, \boldsymbol{\varepsilon}_4^0, \boldsymbol{\varepsilon}_5^0$ and $\boldsymbol{\varepsilon}_6^0$. The twin planes between pair $\{2:6\}$ and $\{4:5\}$ are in $\{110\}$ type of plane; while the other two twin planes are in $\{100\}$ type of plane, as summarized in Table 5.2. Similarly, the compatibility constraints in pair $\{5:6\}$ are scarified, while the

compatibility requirements of other three pairs are still satisfied. Similarly, the average transformation strain of variants 2, 4, 5 and 6 reduces the homogeneous strain energy:

$$\left(\boldsymbol{\varepsilon}_{\mathbf{2}}^{\mathbf{0}}+\boldsymbol{\varepsilon}_{\mathbf{4}}^{\mathbf{0}}+\boldsymbol{\varepsilon}_{\mathbf{5}}^{\mathbf{0}}+\boldsymbol{\varepsilon}_{\mathbf{6}}^{\mathbf{0}}\right)/4=\begin{pmatrix}-0.01 & 0 & 0.0504\\ 0 & -0.01 & 0\\ 0.0504 & 0 & 0.0243\end{pmatrix} \qquad (5.21)$$

It is interesting to note that the repeated simulations with the same applied boundary conditions always result in the selection of four variants out of variant 1 to 8, but not 9-12. This is because the in-plane transformation strains for each of variant 1-8 contain one tension and one compression component, as shown in Eq. (5.18). They can cancel each other to reduce the averaged in-plane transformation strain, so as to lower the stored strain energy, as shown by Eq. (5.20) and (5.21).

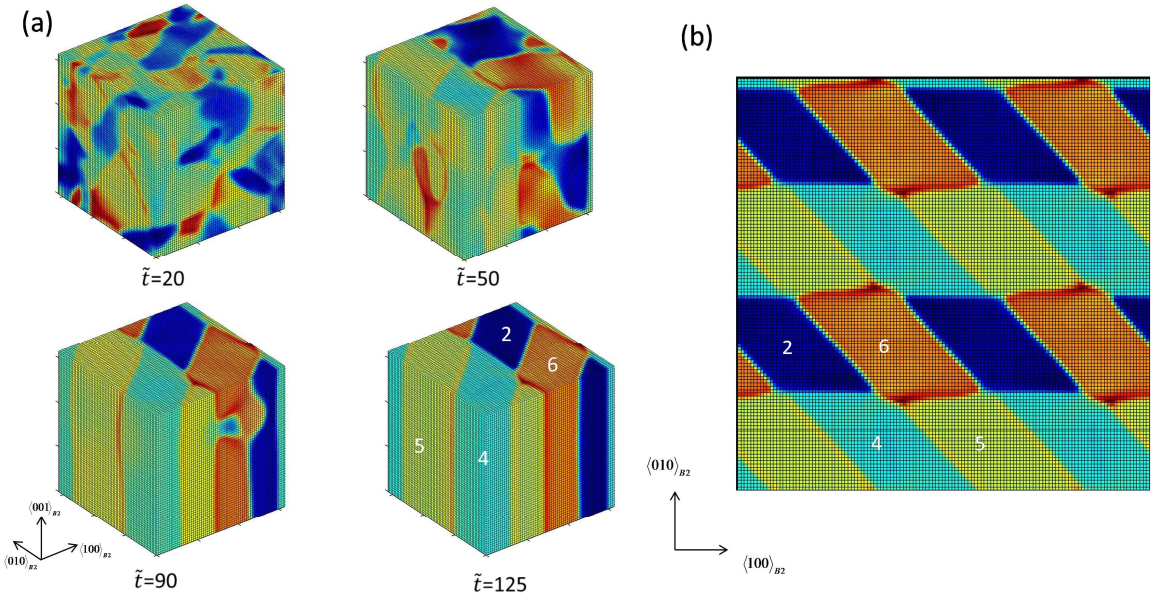

Fig. 5.2 A different result of polytwinned microstructures with the same boundary condition as Fig. 5.1. (a) Nucleation and growth of twinned martensite. (b) 2D projection of 3D microstructures. For a better visualization of polytwinned microstructures, the simulation cell is periodically doubled in the two in-plane directions.

Table 5.2. Compatibility of twin variants obtained in phase field simulations, compared with the crystallography theory based solutions.

Pair	Theoretical Solution [41]	Phase Field
$\{2:4\}$	$\{100\}$ type I	$\{100\}$
$\{2:6\}$	$\{110\}$ type I	$\{110\}$
$\{4:5\}$	$\{110\}$ type I	$\{110\}$
$\{5:6\}$	$\{110\}$ compound	$\{100\}$

5.3.2 Loading effects

The mechanical loading dictates both the selection and patterning of multivariants in the formation of strain-accommodating microstructures. We explore different combinations of boundary constraints. Here the simulation system containing $32 \times 32 \times 32$ mesh grids, $\tilde{\beta}$ is adjusted to be 0.5 and $l_0 = \frac{3\gamma}{4\Delta f(T)\sqrt{2\tilde{\beta}}} = 3.2nm$. Correspondingly, the side length of the cubic simulation cell is 102.4nm.

Fig. 5.3(a) and (b) show the two possible microstructures when the in-plane biaxial tensile strain is applied, i.e., $\varepsilon_1^{app} = \varepsilon_2^{app} = 1\%$, $\varepsilon_6^{app} = 0$ and $\tau_3^{app} = \tau_4^{app} = \tau_5^{app} = 0$. In Fig. 3(a), variants 9 and 12 form the $\{100\}$ twin. In Fig. 5.3(b), variants 10 and 11 form the $\{110\}$ twin, as listed in Table 5.3. Variants 9, 10, 11 and 12 belong to the same group of transformation strain tensors sharing the same normal components (both in-plane tension and out-of-plane compression in Eq. (18)). This group of transformation strain tensors can better match the imposed biaxial tension. Pairing of variants in this group yields the self-accommodating twin structures through complete canceling of in-plane shear strains. Repeated simulations all select the variants in the group containing variants 9, 10, 11 and 12. In most cases, the twin compatibility is satisfied such as the $\{100\}$ twin between variants 9 and 12, as shown in Fig. 5.3(a). However, exceptions are

observed, such as the $\{110\}$ twin of variants 10 and 11, as shown in Fig. 5.3(b) and Table 5.3. The reason is similar with the discussion above. Recall that when the zero in-plane strain is applied in section 5.3.1, only variants 1-8 are possible to nucleate because the in-plane normal strain components contain both tension and compression.

We also perform simulations under in-plane biaxial compression. The resulting microstructures are the same as those obtained in section 5.3.1, as shown in Fig. 5.1 and 5.2. It can be similarly explained by the compatibility requirement between the transformation strain and the imposed boundary conditions.

Fig. 5.3(c) and (d) show the case when the out-of-plane compressive strains are applied, i.e.$\varepsilon_3^{app} = -2\%$ and $\tau_1^{app} = \tau_2^{app} = \tau_4^{app} = \tau_5^{app} = \tau_6^{app} = 0$. Such loading mode of uniaxial compression yields results similar as those from in-plane biaxial tension. The same group containing variants 9, 10, 11 and 12 is the optimal choice, generating the $\{100\}$ twin for variants 10 and 12, and $\{110\}$ twin for variants 9 and 10, as listed in Table 5.3.

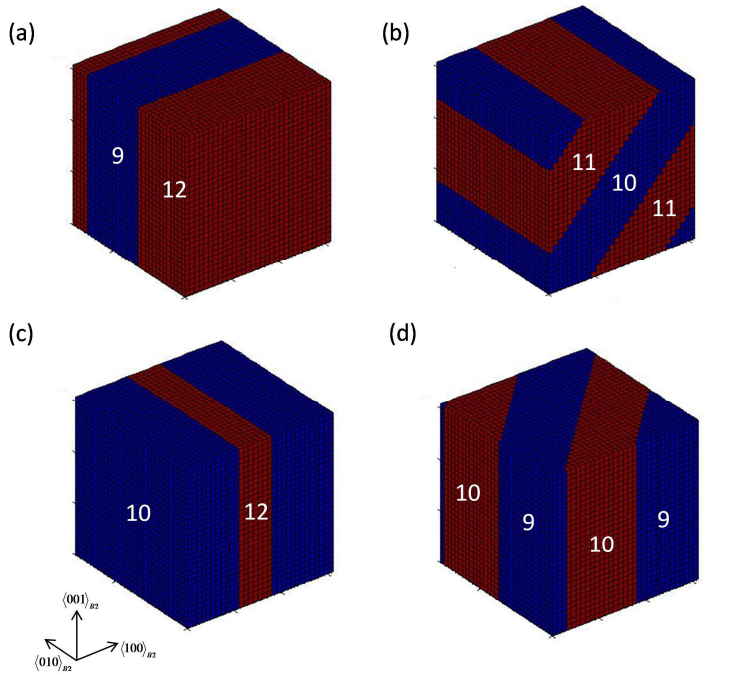

Fig. 5.3 Nucleation of martensite and microstructures at different applied boundary conditions. The mesh grids are colored by the nucleated B19′ variant. (a, b) Different microstructures form under the in-plane biaxial tension $\varepsilon_1^{app} = \varepsilon_2^{app} = 1\%$, $\varepsilon_6^{app} = 0$ and $\tau_3^{app} = \tau_4^{app} = \tau_5^{app} = 0$. (c, d) Different microstructures form under the out-of-plane compression $\varepsilon_3^{app} = -2\%$ and $\tau_1^{app} = \tau_2^{app} = \tau_4^{app} = \tau_5^{app} = \tau_6^{app} = 0$.

Table 5.3. Compatibility of twin variants obtained in phase field simulations, compared with the crystallography theory-based solutions.

Pair	Theoretical Solution [41]	Phase Field
{9: 12} Fig.3(a)	{100} type I	{100}
{10: 11} Fig.3(b)	{100} type I	{110}
{10: 12} Fig.3(c)	{100} type I	{100}
{9: 10} Fig.3(d)	{110} compound	{110}

5.3.3 Orientation effect

We also examine the orientation effects on the martensitic microstructure by setting three axes of the global Cartesian coordinate system to be parallel with the $\langle 110 \rangle$, $\langle 001 \rangle$ and $\langle 1\bar{1}0 \rangle$ directions in the parent B2 phase. The rotation of the transformation strain tensor $\boldsymbol{R\varepsilon_i^0 R^T}$ is required with the rotation matrix

$$\boldsymbol{R} = \begin{bmatrix} 0.707 & 0.707 & 0 \\ 0 & 0 & 1 \\ 0.707 & -0.707 & 0 \end{bmatrix} \tag{5.22}$$

Fig. 5.4(a1) shows the microstructure under the in-plane biaxial compressive strain of 0.5%. The $\{110\}$ twin between variants 11 and 12 is observed. Variants 11 and 12 fully cancel out the shear transformation strain with each other, and they also provide the in-plane transformation strain of biaxial compression, thus accommodating the imposed mechanical load. The $\{110\}$ twin between variants 11 and 12 is also consistent with the compatibility requirements [41], and agrees well with our previous atomistic simulation of $(010)_{\mathrm{B19}}$ compound twin (Fig. 5.4(a2)) [74].

Figure 5.4 (b) shows the polytwinned microstructure when the in-plane 1% biaxial tensile strain of 1% is applied. Variants 2, 3, 6 and 7 form the $\{100\}$ twins. The corresponding twin compatibility is given in Table 4. The nucleation of variants 2, 3, 6 and 7 are determined by the applied biaxial tension, because they are the only four variants whose in-plane components of transformation strain tensors $\boldsymbol{R\varepsilon_i^0 R^T}$ satisfy the loading condition of biaxial tension. The shear component of the average transformation strain is also minimized to zero

$$\boldsymbol{R}\left(\boldsymbol{\varepsilon_2^0} + \boldsymbol{\varepsilon_3^0} + \boldsymbol{\varepsilon_6^0} + \boldsymbol{\varepsilon_7^0}\right)\boldsymbol{R}^T/4 = \begin{pmatrix} 0.033 & 0 & 0 \\ 0 & 0.0243 & 0 \\ 0 & 0 & -0.0524 \end{pmatrix} \tag{5.23}$$

Fig. 5.4 (c) shows the microstructure formed under the out-of-plane compressive strain of 2%. Similarly, variants 2, 3, 6 and 7 nucleate, although the polytwinned morphology is different. As summarized in Table 5.5, pair {2: 3} and {6: 7} form the {100} twin; while {2: 6} and {3: 7} form the {110} twin. All the compatibility requirements at the twin interface are satisfied.

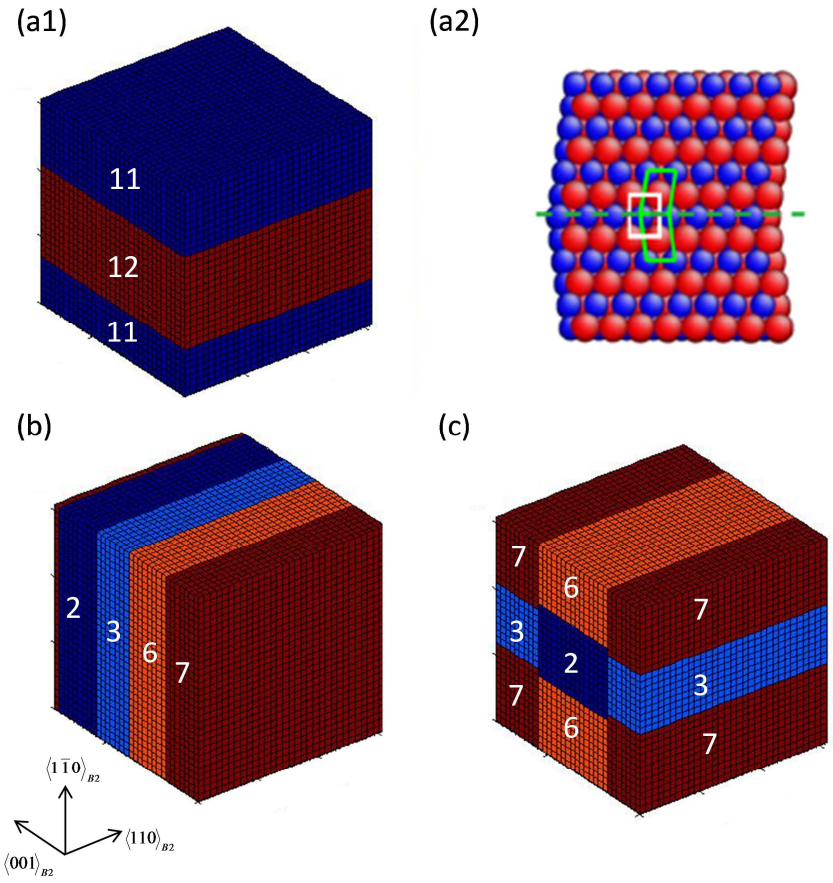

Fig. 5.4 Formation of polytwinned martensitic microstructures at different applied boundary conditions. (a1) {110} compound twin forms under the loading of biaxial compression. (a2) Corresponding atomic structures of {110} compound twin. (b) Layered twin lamellas form under biaxial tension. (c) Polytwinned structure form under out-of-plane compression.

Table 5.4. Compatibility of twin variants obtained in phase field simulations and given by continuum based solutions, corresponding to double tension in Fig. 5.4(b).

Pair	Theoretical Solution [41]	Phase Field
{2: 3}	{100}type I	{100}
{3: 6}	{110}type I	{100}
{6: 7}	{100}type I	{100}
{7: 2}	{110} type I	{100}

Table 5.5. Compatibility of twin variants obtained in phase field simulations and given by continuum based solutions, corresponding to double tension in Fig. 5.4(c).

Pair	Theoretical Solution [41]	Phase Field
{2: 3}	{100} type I	{100}
{2: 6}	{110} type I	{110}
{3: 7}	{110} type I	{110}
{6: 7}	{100} type I	{100}

5.4 Conclusions

We develop a phase field model based on a Landau-type free energy function to study the diffusionless cubic to monoclinic martensitic phase transformation in Nickel-Titanium (NiTi) shape memory alloys. The three-dimensional simulations reveal the nucleation and growth of twelve monoclinic B19′ variants that form the polytwinned morphology of martensitic microstructures. Parametric studies demonstrate that the mechanical constraints govern both the selection and spatial patterning of multivariants in the formation of strain-accommodating microstructures. The present phase field model is generally applicable to study the dynamic evolution of complex alloy systems that involve multi-variants and polytwinned microstructures.

CHAPTER 6

DISLOCATION NUCLEATION DURING NANOINDENTATION

6.1 Introduction

In nanoindentation experiments, the shear stress at the onset of plasticity can approach the theoretical shear strength of a perfect crystal [35, 104-108]. Such ultra-high stress occurs in small (nanometer-sized) volumes beneath the nanoindenter, which can be free of any preexisting defects. A defect-free crystal deforms in a nonlinear manner, when the shear stress approaches the theoretical limit. The nonlinear elastic, or the so-called hyperelastic, response arises from the elastic softening of crystal lattice at large strain. This paper is concerned with the critical role of hyperelasticity, as well as crystallography, in the onset of plasticity during nanoindentation, a process arguably associated with homogenous dislocation nucleation that result from the nonlinear elastic instability of crystal at large shear.

Here we employ the interatomic potential finite element method (IPFEM) [109-111] to simulate nanoindentation and predict homogenous dislocation nucleation. The IPFEM simulation takes as an input the interatomic potential-based constitutive relation derived within the framework of hyperelasticity of single crystals [112]. It can accurately capture the essential physical effects of crystal at large deformation: nonlinear elasticity and shear asymmetry (i.e., the asymmetry of shear stress with respect to the sense of shearing in the Shockley partial direction of $\{111\}\langle 11\bar{2}\rangle$), thereby enabling an accurate prediction of dislocation nucleation. Compared to the commonly used molecular

dynamics (MD), the IPFEM significantly improves the computational efficiency, so that the effects of system size and loading rate can be minimized, and consequently simulations of nanoindentation can be performed on the length and time scales close to laboratory experiments.

In this study, simulations are performed for nanoindentation on several face-centered cubic (fcc) crystals at low temperature (nearly zero-K) when the effect of thermal activation is negligible. For each crystal, we simulate indentation on the (111), (110) and (100) surfaces, and quantify the critical conditions of homogenous dislocation nucleation in the bulk perfect crystal. The results highlight the central role of hyperelasticity (nonlinear elasticity) and crystallography in dislocation nucleation in small material volumes, a process requiring ultra-high stress that is achievable during nanoindentation. Our study also reveals the deficiency of commonly used nucleation criterion such as the critical resolved shear stress. With the rapid development in the experimental techniques of nanoindentation [108], we perform a direct comparison between the experiments and atomistics-based quantification of critical conditions of dislocation nucleation as predicted in this paper [37].

6.2 Methods

6.2.1 Interatomic potential finite element method

The key to the interatomic potential finite element method (IPFEM) is the interatomic potential-based constitutive relation derived within the framework of hyperelasticity with the Cauchy–Born rule [112]. The basic premise of this approach is that every point in a continuum corresponds to a large region of uniformly deformed lattice at the atomic scale. It follows that the energy of a continuum point can be

calculated by summing the energy of the underlying lattice deformed according to the continuum deformation gradient, F_{ij}. Specifically, for a continuum point, all underlying atoms are identical, one may consider the energy of one atom at the origin to be representative, and calculate the energy associated with this atom; the energy density is the energy per atom divided by the atomic volume. Within the framework of the embedded-atom method (EAM) [113], and consider the crystal at nearly zero-K temperature, the energy density W is given by

$$W = \frac{1}{\Omega_0}\left[\sum_K V(r^K) + U(\bar{\rho})\right] \tag{6.1}$$

where $V(r^K)$ is the pair potential, $\bar{\rho} = \sum_K \rho(r^K)$ is the ambient electron density for the atom at the origin, and $U(\bar{\rho})$ is the energy required to embed this atom into the electron density. In Eq. (6.1), Ω_0 is the atomic volume in a stress free fcc lattice, namely, $\Omega_0 = a_0^3/4$, where a_0 is lattice constant; r^K denotes the distance between the atom at the origin and a neighboring atom when the lattice is deformed, here, the index *K* runs over all atoms within a cut-off radius R_c prescribed by the interatomic potential.

The Cauchy (true) stress can be obtained using the standard relation between energy density and stress,

$$\sigma_{ij} = \frac{1}{\det(F_{ij})} F_{im} F_{jn} \frac{\partial W}{\partial E_{mn}} \tag{6.2}$$

In Eq. (6.2), the Green strain E_{ij} is defined as $E_{ij} = \frac{1}{2}(F_{ki}F_{kj} - \delta_{ij})$, where δ_{ij} denotes the Kronecker delta; the energy density W, as defined in Eq. (6.1) depends on E_{ij} through

$r^K = \sqrt{(\delta_{ij} + 2E_{ij}) x_{0i}^K x_{0j}^K}$, where x_{0j}^K is the coordinate of a neighboring atom in the stress-free fcc lattice. Substitution of Eq. (6.1) into Eq. (6.2) leads to

$$\sigma_{ij} = \frac{1}{\det(F_{ij})\Omega_0} \sum_K \left[\frac{1}{2} \frac{\partial V(r^K)}{\partial r} + \frac{\partial U(\bar{\rho})}{\partial \bar{\rho}} \frac{\partial \rho(r^K)}{\partial r} \right] \frac{x_i^K x_j^K}{r^K} \tag{6.3}$$

Here x_j^K denotes the Cartesian coordinate of a neighboring atom in the deformed lattice, and it can be calculated by $x_j^K = F_{ij} x_{0j}^K$. Since the Cauchy stress in Eq. (6.3) involves lattice sum and nonlinear functions of $V(r^K)$, $U(\bar{\rho})$ and $\rho(r^K)$ [114, 115], the effects of crystal anisotropy and nonlinear elasticity are incorporated automatically.

The tangent modulus, c_{ijkl}, can also be calculated from the interatomic potential, as detailed in [111],

$$\begin{aligned} c_{ijkl} = \frac{1}{\det(F_{ij})\Omega_0} \Bigg\{ & \sum_K \left[\frac{1}{2} \left(\frac{\partial V^2(r^K)}{\partial r^2} - \frac{1}{r^K} \frac{\partial V(r^K)}{\partial r} \right) + \frac{\partial U(\bar{\rho})}{\partial \bar{\rho}} \left(\frac{\partial^2 \rho(r^K)}{\partial r^2} - \frac{1}{r^K} \frac{\partial \rho(r^K)}{\partial r} \right) \right] \frac{x_i^K x_j^K x_k^K x_l^K}{(r^K)^2} \\ & + \frac{\partial^2 U(\bar{\rho})}{\partial \bar{\rho}^2} \left(\sum_K \frac{\partial \rho(r^K)}{\partial r} \frac{x_i^K x_j^K}{r^K} \right) \left(\sum_K \frac{\partial \rho(r^K)}{\partial r} \frac{x_k^K x_l^K}{r^K} \right) \Bigg\} \end{aligned} \tag{6.4}$$

Here, the current and reference configurations are assumed to coincide. Because of the elastic softening of the hyperelastic crystal, the prediction of dislocation nucleation requires an update of the tangent modulus c_{ijkl} when deformation gradient F_{ij} changes.

The above interatomic potential-based constitutive model can accurately describe the hyperelastic response of a bulk crystal, whereas it is inadequate to model the elastic behavior of atomic layers near the crystal surface [116], where atoms are mis-coordinated compared to the perfect crystal. However, since we will consider the indenter with a tip

radius of 50nm (an approximate size in experiments), the nucleation sites are located at about 10nm below the contact surface, so that the effect of mis-coordinated surface atoms are negligible. As such, this constitutive model is sufficient to study nanoindentation-induced dislocation nucleation inside the bulk crystal, as verified by molecular dynamics simulations [111].

The interatomic interactions are modeled using the EAM potentials [113], which can better describe the many-body effects of metallic bonding compared to the two-body pair potential such as Lennard-Jones potential. The EAM potentials used in this study are developed by Mishin et al. [114, 115], which have been validated by comparing with experimental results (if available) and/or *ab initio* calculations. Table 6.1 compares the elastic constants of the stress-free crystals (Cu/Ni/Al) between experiments and predictions by the potentials. It also lists the crystal-anisotropy parameter $\beta \equiv 2c_{44}/(c_{11}-c_{12})$; for isotropic materials, $\beta = 1$.

Table 6.1. Elastic constants of stress-free single crystals of Cu, Ni and Al. Predictions by the EAM potentials are compared with experimental data. $\beta \equiv 2c_{44}/(c_{11}-c_{12})$ measures the degree of crystal anisotropy.

		c_{11}(GPa)	c_{12}(GPa)	c_{44}(GPa)	$\beta \equiv \frac{2c_{44}}{c_{11}-c_{12}}$
Cu	Experiment	168.4	121.4	75.4	3.2
	Potential	169.9	122.6	76.2	
Ni	Experiment	247	147	125	2.5
	Potential	247	148	125	
Al	Experiment	114	61.9	31.6	1.2
	Potential	114	61.6	31.6	

We have implemented this interatomic potential-based hyperelastic model for the fcc crystals of Cu, Al and Ni in the finite element program ABAQUS/Explicit (2006) by writing user material subroutines. In the dynamic, explicit computational procedures of this program, as detailed in ABAQUS Theory Manual [117], the nonlinear response is obtained incrementally, given the internal forces created by the stresses in the elements, as well as the applied external forces at the start of an increment, time *t*. Finite element procedures solve for the acceleration at the start of the increment by solving the discretized local equations of motion. The velocities at time $t + \Delta t / 2$ and the displacements at time $t + \Delta t$ are updated by a central difference time-integration procedure. The deformation gradient F_{ij} for each integration point at time $t + \Delta t$ is then calculated based on the updated displacement field. Given the calculated deformation gradient, a constitutive equation subroutine, called VUMAT in ABAQUS/Explicit, is required in order to determine the stress in the element at time $t + \Delta t$. In the implementation of stress calculation according to Eq. (6.3), each material point (integration point) is represented by an fcc lattice, which deforms according to the local continuum deformation gradient F_{ij}. That is, at the beginning of the calculation ($t = 0$), a set of neighboring atoms is created to represent the atomic environment of the central atom at the origin, e.g., an atom in the first neighboring shell should be located at ($a_0 / 2, a_0 / 2, 0$), an atom in the second neighboring shell is at $(a_0, 0, 0)$, etc. Here, the lattice spacing a_0 is chosen such that the Cauchy stress is zero at $t = 0$, and the number of included neighboring atoms is determined by the cut-off radius prescribed by interatomic potentials [114, 115]. For each time increment, the neighboring atoms update their positions according to the local deformation gradient F_{ij}, which is generated

according to the imposed boundary conditions. Then the Cauchy stress σ_{ij} and tangent modulus c_{ijkl} are calculated by substituting the deformed positions of neighboring atoms into Eq. (6.3) and (6.4), respectively. Thus, material properties depend exclusively on the atomistic description of the system.

6.2.2 Nonlinear elasticity and shear asymmetry at large strain

In this section, we highlight the important features of the interatomic potential-based constitutive model: nonlinear elasticity and shear asymmetry at large strain. Consider an fcc crystal undergoing uniform simple shear in the Shockley partial direction of $\{111\}\langle 11\bar{2}\rangle$. Fig. 6.1 shows the shear stress-strain curves predicted by the EAM potentials. Evidently, the crystal at large shear exhibits nonlinearity and asymmetry of shear stress with respect to the sense of shearing in the $\langle 11\bar{2}\rangle$ direction. The former can be attributed to the elastic softening at large strain, whereas the latter arises because of the asymmetric packing of atoms in the $\langle 11\bar{2}\rangle$ direction [111]. The two effects critically control when, where and how a dislocation homogeneously nucleates beneath the indenter.

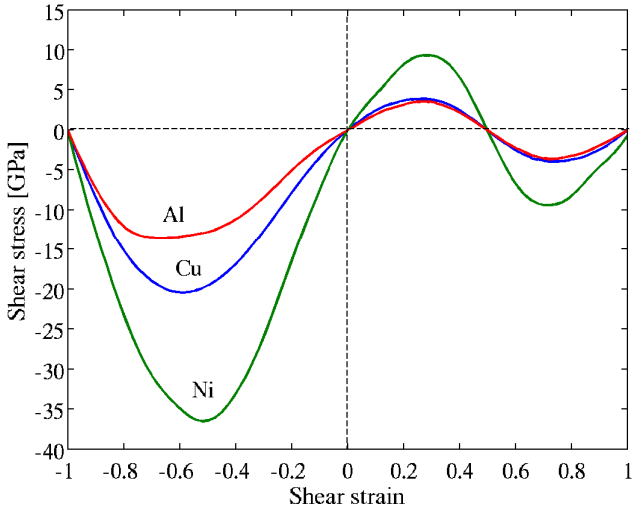

Fig.6.1. Stress-strain curves for simple shear of single crystals of Al, Cu, Ni in the Shockley partial direction of $\{111\}\langle 11\bar{2}\rangle$, showing the nonlinear elasticity and asymmetry of shear stress with respect to the sense of shearing at large deformation.

6.2.3 Dislocation nucleation criterion

Homogenous dislocation nucleation in the bulk perfect crystal can be triggered by the nonlinear elastic instability of crystal at large deformation. The onset of instability is associated with the Hadamard condition of loss of positive definiteness of the matrix Q_{jk} defined by

$$Q_{jk} = n_i (c_{ijkl} + \sigma_{jk}\delta_{il}) n_l \tag{6.5}$$

for any unit vector n_i [118, 119]. Here, the current and reference configurations are assumed to coincide; σ_{jk} is the Cauchy (true) stress and c_{ijkl} is the tangent (instantaneous elastic) modulus, both of which are calculated from the interatomic potential, see Eq. (6.3) and (6.4). For small deformations, Q_{jk} is positive definite. When

$$\det(Q_{jk}) = 0 \tag{6.6}$$

loss of stability occurs, leading to dislocation nucleation. Correspondingly, the unit vector n_i predicts the activated slip plane, and the eigenvector g_i associated with the matrix Q_{jk} predicts the slip direction at the onset of dislocation formation. By comparing with MD simulations, we have quantitatively verified the accuracy of this nucleation criterion in terms of the predictions of the critical indentation load, location of nucleation site and activated slip systems [111].

To appreciate the key difference between the nucleation criterion of Eq. (6.5) with the commonly used one such as the critical resolved shear stress (CRSS), we note that Q_{jk} in Eq. (6.5) contains both the tangent modulus c_{ijkl} and Cauchy (true) stress σ_{jk}. When a dislocation is about to nucleate (the corresponding shear strain is large), the magnitudes of c_{ijkl} and σ_{jk} become comparable due to elastic softening of the hyperelastic crystal; the nucleation criterion of Eq. (6.5) states that when the decreasing c_{ijkl} is balanced with the increasing σ_{jk}, the crystal becomes unstable, leading to homogenous dislocation nucleation. Since the instability does not occur precisely when the tangent modulus vanishes (equivalently, the RSS maximizes), the nucleation criterion based on the CRSS is not accurate. Moreover, the CRSS is not a material constant; it depends on other stress components than just the shear. Thus, even an approximate use of CRSS to predict nucleation would require a calibration for different stress (deformation) states, similar to the construction of a yield surface in stress space in the plasticity theory. In contrast, the nucleation criterion of Eq. (6.5) does not require calibration; nucleation occurs as a natural consequence of loss of positive definiteness of the matrix Q_{jk}.

6.2.4 Simulation setup

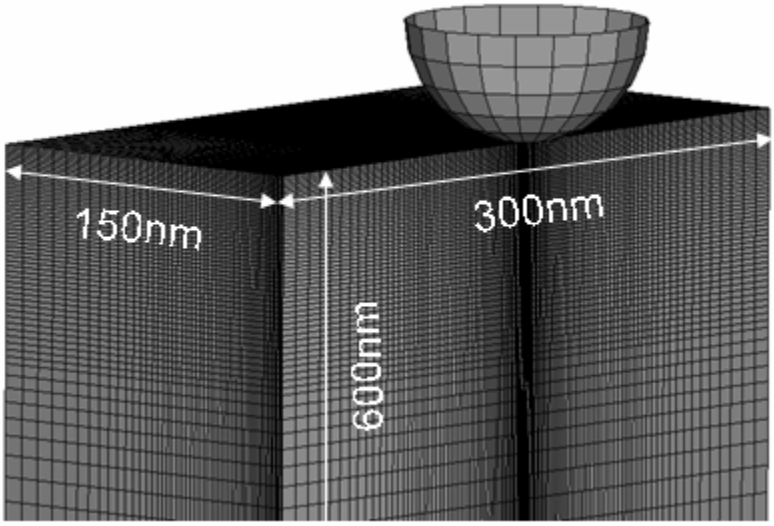

Fig. 6.2. Finite element mesh for indentation simulation. The spherical indenter is modeled as a frictionless, analytic rigid surface. The simulation cell is one half of the whole system considering the cubic symmetry of the fcc crystal.

Using the IPFEM, we have performed 3D simulations of nanoindentation by a spherical indenter, and quantified the critical states of dislocation nucleation. Predictions will be given as to when and where the dislocation will nucleate within the crystal, and what slip mode the nucleated dislocation will take. More specifically, indentation is simulated for a spherical indenter pressed into the (111), (110) and (100) surfaces of single crystals of Al, Cu, Ni. The radius of the indenter is 50nm, the approximate tip size of a nominally sharp Berkovich indenter used in typical nanoindentation experiments. The spherical indenter is modeled as a frictionless, analytic rigid surface. Since this research is focused on dislocation nucleation inside the bulk crystal, the effects of indenter elasticity and contact adhesion are ignored. However, those effects could play an important role if a dislocation nucleate directly from the contact surface [120, 121]; a detailed study of surface nucleation is beyond the scope of this work. We have previously

performed extensive numerical testing to assess the influences of geometry of simulation cell, imposed far-field boundary conditions, element type, and node density by comparing with the Hertzian solutions for the isotropic and anisotropic, linear elastic material, as detailed in [111]. We found for a system with the in-plane size of 300×300 and depth of 600nm, the effect of boundary constraint is sufficiently minimized. To reduce the computational cost, we simulate one half of the whole system considering the cubic symmetry of crystal, as shown in Fig. 6.2. The boundary conditions are imposed as follows: the displacement along the bottom of the mesh is constrained to be zero, while the displacements of lateral surfaces are unconstrained. The graded mesh comprises 8-node linear brick elements, with typical size of elements near the indenter about $10\,\mathring{\mathrm{A}}$. The total number of elements is 519,332. Indenter is moved down in displacement control at a sufficiently low rate to mimic the quasi-static loading condition, as calibrated by the analytic solutions for indentation on a linear anisotropic elastic material [111].

6.3 Results

6.3.1 Indentation load-displacement response

Figs. 6.3(a)-(c) show the load-displacement (*P*-*h*) curves for nanoindentation on single crystals of Al, Cu and Ni, respectively. For each crystal, the *P*-*h* curves are calculated for three indentation orientations (111)/(011)/(001). The different *P*-*h* responses arise because of the elastic anisotropy of single crystals. For Al, the three *P*-*h* curves are very close, consistent with the fact that Al is a nearly isotropic material ($\beta = 1.2$, see Table 6.1). As the elastic anisotropy increases, i.e., from $\beta = 2.5$ for Ni to $\beta = 3.2$ for Cu, the variation in the *P*-*h* responses also increases for different indentation

orientations. These results are consistent with the variation of indentation moduli given in Table 6.2, where the crystal is simplified as a linear, anisotropic and elastic material; such simplification renders the indentation moduli analytically solvable, thus providing a quantitative reference to the numerical calculation for the hyperelastic crystals. We note that the crystal beneath the nanoindenter should have undergone nonlinear elastic deformation before homogenous dislocation nucleation. But the effect of nonlinearity is not significant on the *P-h* response. This is because the *P-h* curve is not a particularly sensitive indicator on the nonlinear elastic deformation during nanoindentation, as it represents an average of the linear elastic response at the far field and the nonlinear elastic response close to indenter. However, the hyperelastic constitutive model, which is the basis of IPFEM simulations, is essential to predict dislocation nucleation caused by the nonlinear elastic instability of crystals at large shear, as shown later.

Table 6.2. Indentation moduli, E^*, for single crystals of Al, Cu and Ni. They are calculated by numerical integration using the semi-analytic indentation solution, with the elastic constants predicted by the interatomic potentials, as listed in Table 6.1.

	$E^*_{(111)}$ (GPa)	$E^*_{(100)}$ (GPa)
Al	88.9	87.1
Cu	153	135
Ni	254	228

Specifically, when a cubic crystal deforms in the regime of linear anisotropic elasticity, the *P-h* response can be derived as $P = \frac{4}{3} E^* R^{1/2} h^{3/2}$ for a spherical indenter (radius *R*) on a half space; for the (111) and (100) indentations, it can be proven that the

contact area is circular because of crystal symmetry, and the semi-analytic solution is given by [122, 123].

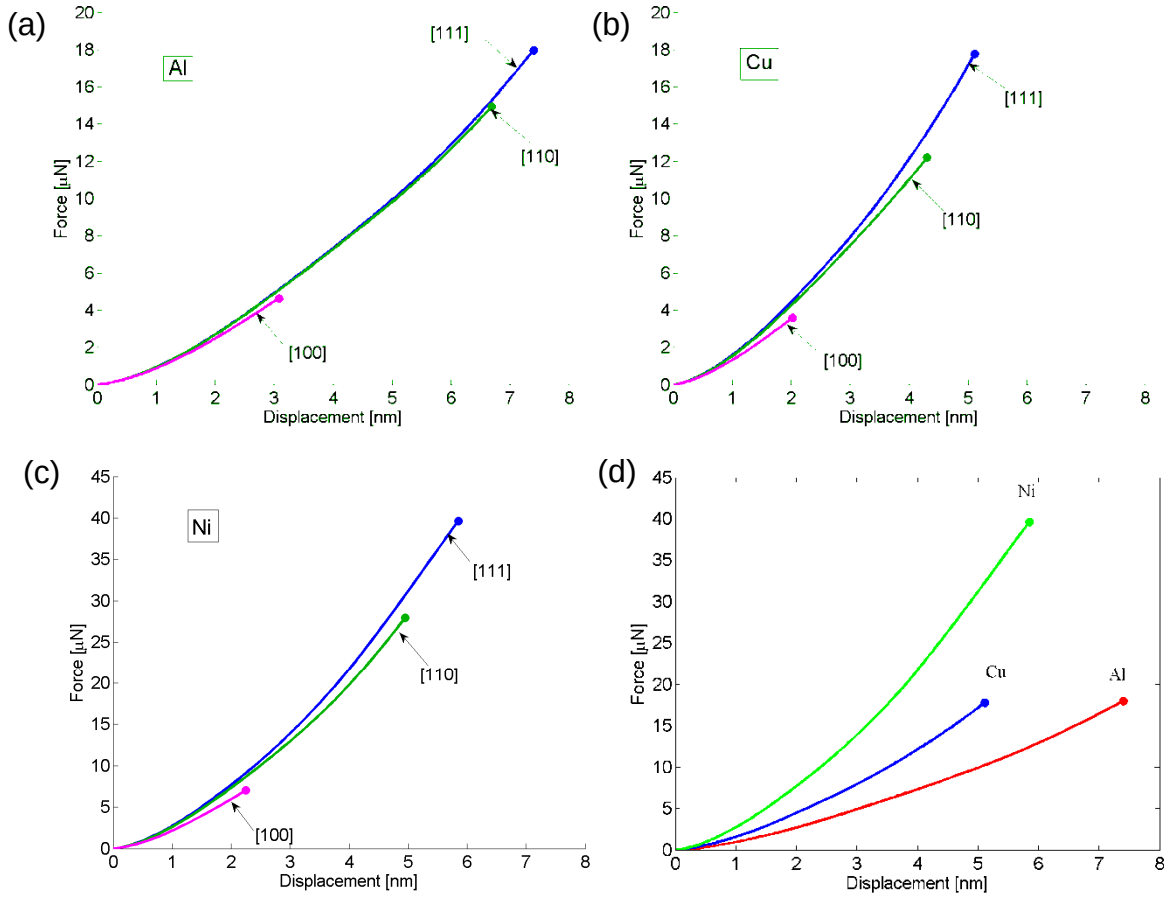

Fig. 6.3. Nanoindentation load-displacement curves for indentation on the (111), (110), (100) surfaces of single crystals of (a) Al, (b) Cu, (c) Ni. The (111) indentations are compared in (d) for the three crystals.

In Figs. 6.3(a)-(c), each *P-h* curve is terminated at an indentation depth (indicated by circle), when the onset of dislocation nucleation is first identified by the nucleation criterion of Eq. (6.5). For each crystal, the critical load of nucleation (P_c and h_c) changes considerably for different indentation orientations, e.g.,

$h_c^{\{111\}} : h_c^{\{110\}} : h_c^{\{100\}} \approx 5.04\text{nm} : 3.85\text{nm} : 1.93\text{nm} \approx 2.6 : 2 : 1$ for Cu. This change arises because of the effect of crystallography. Specifically, consider a simple situation of dislocation nucleation in the bulk single crystal under a uniaxial compressive stress σ. In this case a dislocation tends to nucleate on one of the $\{111\}\langle 11\bar{2}\rangle$ slip systems, where the resolved shear stress $\tau = m\sigma$ (m denotes the Schmid factor) first exceeds the shear resistance of nucleation in a perfect lattice. By considering the hard sphere packing of an fcc lattice and noting the effect of shear asymmetry as shown in Fig. 6.1, one can readily calculate m and identify the slip system of nucleation; for different compression orientations, the ratio of the inverse Schmid factor is $1/m^{\{111\}} : 1/m^{\{110\}} : 1/m^{\{100\}} = 3 : 2 : 1$. One may assume the shear resistance of nucleation τ_c is the same for each case, and then obtains $\sigma_c^{\{111\}} : \sigma_c^{\{110\}} : \sigma_c^{\{100\}} = 3 : 2 : 1$; here, in a first approximation we ignore the influence of other stress components on τ_c. The ratio of σ_c for different compression orientations is qualitatively consistent with that of the nucleation load h_c for different indentation orientations, thereby showing that the variation of h_c is dominantly controlled by the effect of crystallography. While the above simple analysis clarifies the controlling factor on h_c, the IPFEM calculations enable quantification of P_c and h_c by solving the distribution of non-uniform and nonlinear elastic deformation beneath the indenter, as shown in Fig. 6.3.

In Fig. 6.3(d), we compare the *P-h* curves for the (111) indentation of the three crystals. It is seen that Ni is much stiffer than Cu and Al, consistent with the result that Ni has a higher indentation modulus as shown in Table 6.2. In terms of the critical indentation displacements of nucleation, h_c, it is interesting to note that although Cu and

Al show very similar response for uniform simple shear (see Fig.6.1), their h_c differ considerably; such difference arises because of crystal anisotropy, as well as the non-uniform deformation beneath the indenter, as manifested in the different indentation moduli (see Table 6.2).

6.3.2 Nucleation site and activated slip system

Fig. 6.4 shows the predicted nucleation sites from IPFEM calculations, using Al as an example. As schematically shown in Fig. 6.4(a), the nucleation site for the (100) indentation is at the central loading axis. In contrast, it is off the central axis for the (110) and (111) indentations; the number of equivalent sites, as well as their locations, is dictated by crystal symmetry, see [111] for example. In Fig. 6.4(b), we show the contours of $\det(Q_{jk})$ at the respective critical moment of nucleation and for the respective activated slip system. In each case, the gray element (highlighted with red circles) indicates the nucleation site directly visible on the surface of the simulation cell. Because of the high symmetry of indentation orientations, there are multiple equivalent slip systems at each site; the slip system first activated in experiment or MD simulation would be randomly selected by thermal fluctuations. Our predictions by IPFEM, which accurately incorporate the effects of elastic softening and crystal anisotropy, have been qualitatively verified by MD simulations [37]; but they are at variance with predictions based on the linear elastic analysis [124] and/or using the stress-based nucleation criterion such as the maximum equivalent shear stress or CRSS [125].

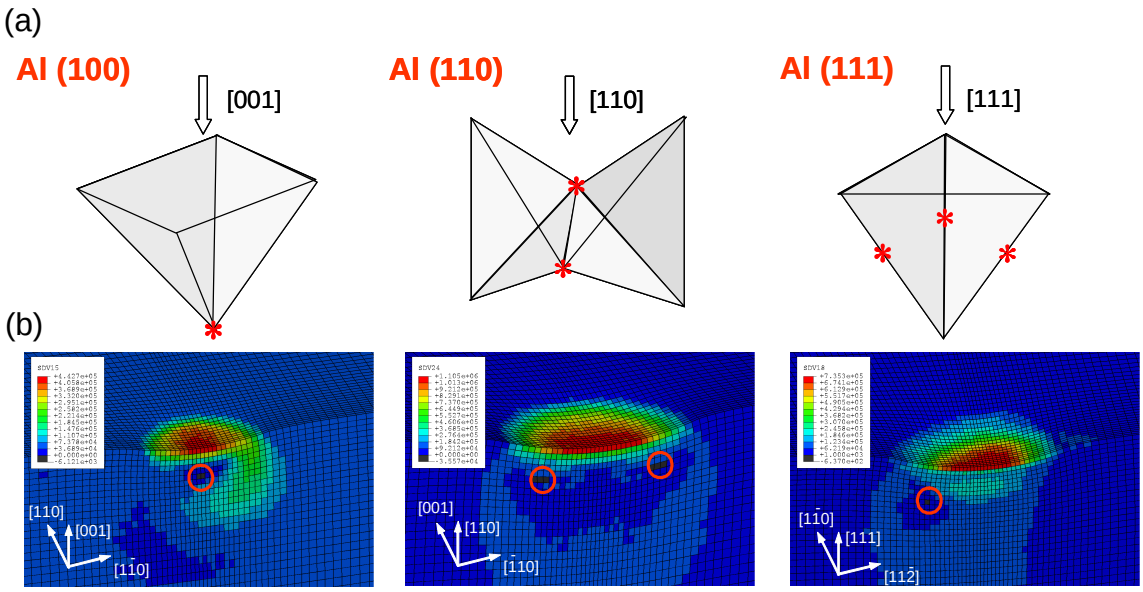

Fig. 6.4. IPFEM predictions of nucleation sites by nanoindentation on the (100), (110) and (111) surfaces of single crystal Al. (a) Schematics of location of nucleation sites; all the solid lines are in the $\langle 110 \rangle$ directions and the shaded triangles represent the {111} plane. (b) Contours of $\det(Q_{jk})$ at the respective critical moment of nucleation and for the respective activated slip plane. The gray element (highlighted with red circles) has a small negative value of $\det(Q_{jk})$, thus showing the nucleation sites.

6.3.3 Critical resolved shear stress

We calculate the critical resolved shear stress (CRSS), τ_c, at the onset of nucleation, and show the CRSS is not an accurate nucleation criterion. Fig. 6.5 shows the indentation displacement versus RSS curves. The RSS, τ, is calculated at the critical nucleation site and for the activated slip system, according to $\tau = \sigma_{ij} n_i g_j$, where the current slip-plane normal, n_i, and slip direction, g_i, are related to those in the undeformed crystal, n_{0j} and g_{0j}, by $n_i = n_{0j} F_{ji}^{-1}$ and $g_i = F_{ij} g_{0j}$, respectively. In Fig.

6.5, circle represents the CRSS, τ_c, when the nucleation criterion is first satisfied in IPFEM calculations. The respective τ_c is listed in Table 6.3 for the three crystals and three indentation orientations. Importantly, τ_c is not a constant for each crystal, and it depends on the indentation orientation. Fig. 6.5 also shows that τ_c is close to, but not right at the maximum of RSS. This is due to the elastic-softening effect associated with the hyperelastic crystals; namely, according to the physically based nucleation criterion of Eq. (6.5), the nucleation occurs when the tangent modulus c_{ijkl} is balanced with the Cauchy stress σ_{ij}, rather than when c_{ijkl} vanishes or equivalently the RSS maximizes. Hence, these results clearly demonstrate that the CRSS is not an accurate nucleation criterion; an approximate use of CRSS needs a calibration by combining experiments and IPFEM calculations.

Finally, we note that Fig. 6.5(c) reveals a numerical artifact of the RSS response for Ni under the (110) indentation, i.e., there is an abrupt change of the slope at low loads. Considering the overall reliable performance of the EAM potentials, which have been extensively calibrated by comparing with experimental or *ab inito* data [114, 115], we believe such a small artifact should not affect the overall reliability of the results reported in this study.

Table 6.3. The critical resolved shear stress (CRSS) of dislocation nucleation

	(111)	(110)	(100)
τ_c - Cu (GPa)	3.2	3.0	2.3
τ_c - Al (GPa)	3.8	4.0	3.1
τ_c - Ni (GPa)	8.2	8.0	4.5

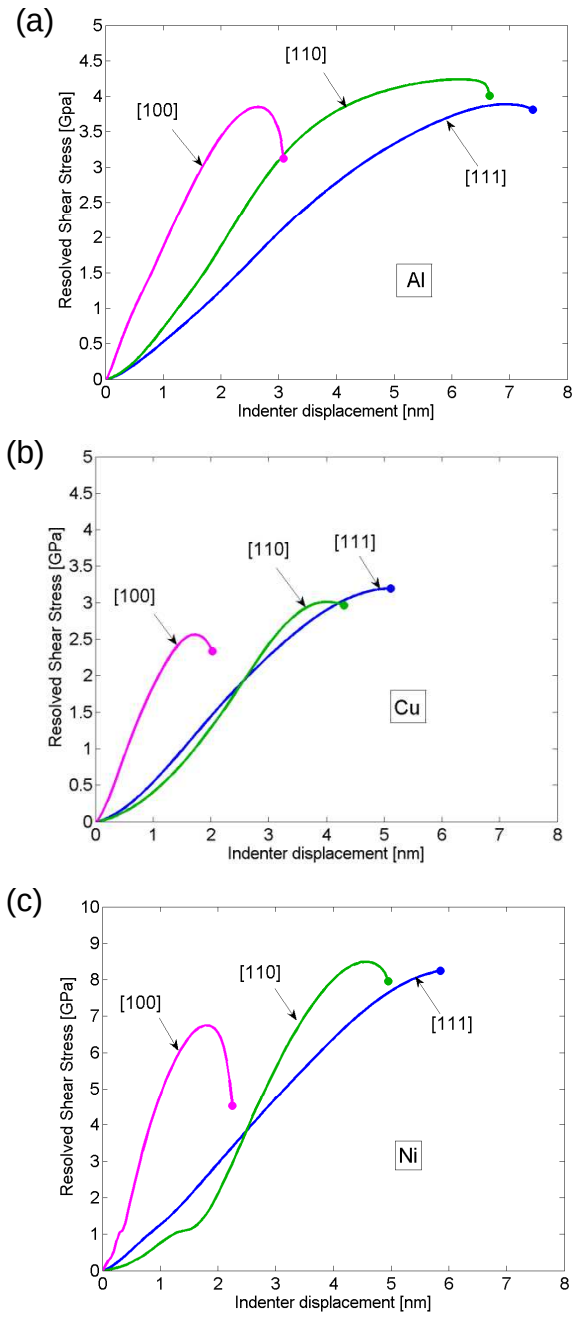

Fig. 6.5. Nanoindentation displacement versus resolved shear stress at the critical nucleation site and for the activated slip system for single crystals of Al, Cu and Ni.

6.4 Discussions

6.4.1 Nanoindentation experiment

We compare our IPFEM results with nanoindentation experimental results. Nanoindentation experiments were performed on Cu single crystals by our collaborators [37]. Both the pyramid Berkovich tip (with an indenter radius of $164 \pm 10\text{nm}$) and cube-corner tip (with an indenter radius of $53 \pm 4\text{nm}$) were used. Indentations are performed on (111), (110), and (100) surfaces under constant loading rate $\dot{P} = 10\mu\text{N/s}$. For each orientation, at least 300 indentations were measured. Experimental results show the strength is not a constant but fluctuates.

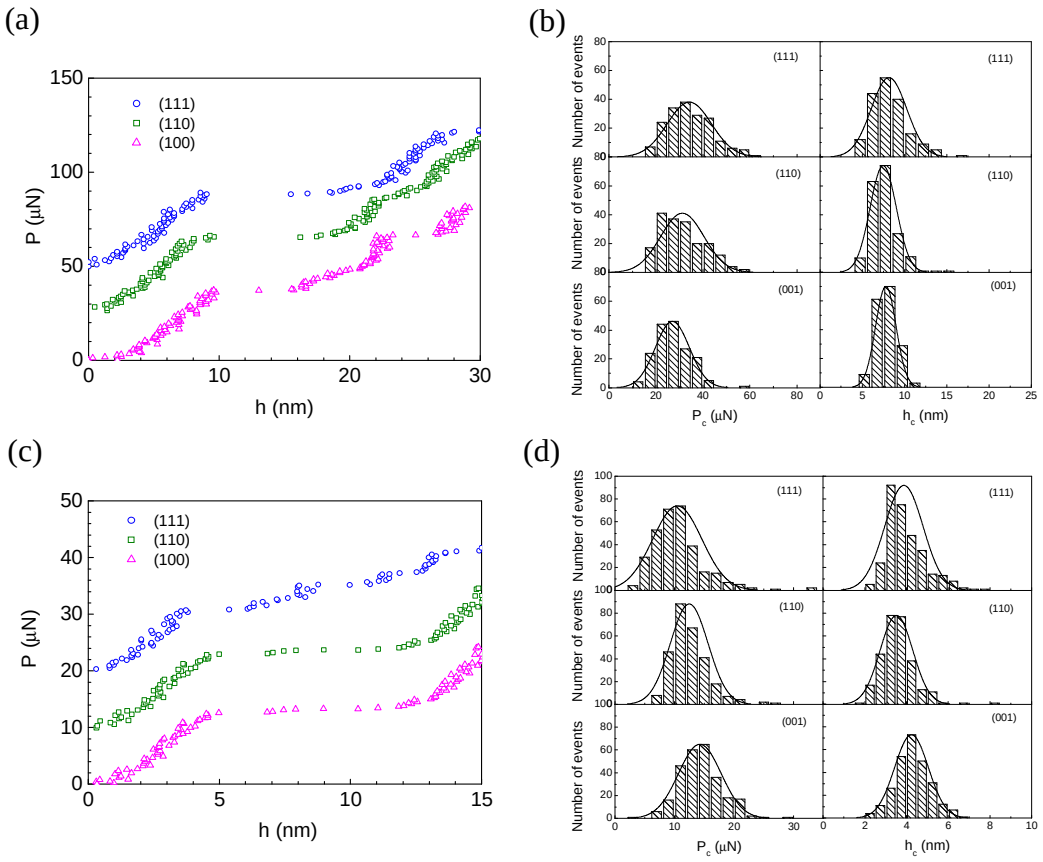

Fig. 6.6. Experimental results of (111), (110), and (100) nanoindentation on single crystal Cu. (a) Representative P-h curves for (tip radius $R = 164 \pm 10\text{nm}$), and (b) Histograms of the critical indenter force P_c and displacement h_c at the onset of displacement bursts for the same tip radius. (c) Similar with (a), and (d) Similar with (b), except for the tip radius $R = 53 \pm 4\text{nm}$). In (a) the origin of the indenter force P is shifted for (111) and (110) cases to guide the eyes, and in (b) each nanoindentation orientation includes about 300 indents.

Stochastic, discontinuous character is shown by nanoindentation experiments in Fig 6.6, in contrast to the typical smooth yield behavior in their bulk counterparts [34, 105, 126-128, 129]. Such jerky behavior has been attributed to the stochastic nature of dislocation sources in nanoscale and is fundamentally different from the microscale size effect often related to hardening associated with strain gradients [130]. In such a small volume, the number of potential dislocation sources is severely limited, and initial yield events evolving from a single source become measurable, as manifested by displacement bursts in a load-controlled nanoindentation test [129]. The statistical distribution of source strengths can lead to the fluctuation of yield stresses for a fixed indenter size.

6.4.2 Theoretical analysis

The stochastic nature of a single source can be characterized by using the weakest link concept and Weibull statistics [131, 132]. It follows that the cumulative probability of discrete plastic yielding is given by [133]

$$F(\sigma, L) = 1 - \exp\left[-\left(\frac{L}{L_0} \right)^d \left(\frac{\sigma}{\sigma_0} \right)^m \right] \tag{6.7}$$

where L is the characteristic length scale of the highly stressed volume, σ is the average stress acting on this volume, d is the dimensionality of the source ($d = 2$ for surface and $d = 3$ for bulk defects), m is the Weibull modulus, L_0 is the reference length, and σ_0 is the reference stress. Eq. (6.7) implies that the yield strength σ_Y satisfying the scaling law

$$\sigma_Y \propto L^{-\beta} \tag{6.8}$$

where the exponent $\beta = d/m$.

On the other hand, we rewrite Eq. (6.7) to

$$\ln\left[\ln\left((1-F)^{-1}\right)\right] = m\ln(\sigma/\sigma_0) + \ln\left[(L/L_0)^d\right] \tag{6.9}$$

The parameters of β and Weibull modulus m can be determined by linear regression of the experimental data, which finally provide the dimensionality of the nucleation source in Table 6.4.

Table 6.4. The indenter force P_c and displacement h_c at the onset of initial displacement bursts from nanoindentation experiments. The power-law exponent β, Weibull modulus m, and the dimensionality of dislocation source $d = \beta m$ are also provided.

Indentation plane	Berkovich tip (R = 164nm)		Cube-corner tip (R = 53nm)		β	m	d
	P_c (μN)	h_c (nm)	P_c (μN)	h_c (nm)			
(111)	34.2±9.4	8.2±2.1	10.5±4.1	3.9±0.9	0.22	8.11	1.8
(110)	31.2±9.2	7.4±1.5	12.5±3.2	3.5±0.8	0.27	7.49	2.0
(100)	27.0±7.3	7.8±1.2	14.3±3.6	4.2±0.8	0.49	5.67	2.8

These results indicate that bulk defects ($d \approx 3$) are most likely responsible for the displacement bursts in the case of (100) indentation. In contrast, surface defects ($d \approx 2$) are most likely underlying the bursts in the (111) and (110) indentations.

6.4.3 Heterogeneous dislocation nucleation

Using the IPFEM, we study the nanoindentation-induced homogenous dislocation nucleation in a dislocation-free perfect crystal as a possible cause of experimentally measured displacement bursts. The IPFEM enables nanoindentation simulations at the experimental size scale while retaining the atomic-scale resolution. We consider the homogenous dislocation nucleation resulting from the hyperelastic (non-linear elastic) instability [111]. When the indenter radius *R* is 50nm, the critical indenter displacements for nucleation are predicted as $h_c^{(111)} : h_c^{(110)} : h_c^{(100)} \approx 2.6 : 2 : 1$, with the corresponding nucleation sites shown in Fig. 6.4 and 6.7 (a). These ratios have been verified qualitatively by direct MD simulations in smaller systems (*R* = 5nm), as shown in Fig. 6.7 (b), and can also be rationalized by evaluating the Schmid factors or resolved shear stresses on the most favorably oriented slip systems for nucleation [134]. Importantly, while these predictions are within the range of experimental values of h_c (as given in Table 6.4), they disagree qualitatively with the measured ratios that exhibited a considerably weak orientation dependence. Such differences provide quantitative evidence that discontinuous yielding should be triggered by the activation of

heterogeneous sources, rather than the homogenous dislocation nucleation in a small volume of perfect crystal beneath the indenter tip.

6.4.4 Dimensionality of nucleation sources

In order to understand the effect of crystallographic orientation on the dislocation sources responsible for the indenter displacement bursts in experiments, we have performed direct MD simulations to study the post homogenous nucleation behavior in nanoindentation. Our MD simulation is performed in a displacement-controlled mode, such that the discontinuous yielding event is shown as a load drop rather than a displacement burst under force control. Fig. 6.7(b) shows that in the (100) indentation, the load drop is not observed immediately after the initial homogenous nucleation event (as indicated by the square symbol); the indenter force continues to increase, and a significant load drop occurs at a much larger force, as also reported by Liang et al. [135]. Such hardening response arises because of the immediate formation of dislocation locks. In particular, the nucleation site and the site of lock formation coincide, both of which are located at the central axis where the four equivalent slip systems (indicated by shaded triangles) intersect, see Fig. 6.7(a). Notice that the lock junction creates a wedged-shape region bounded by the two {111} slip planes (see Fig. 6.7(c)), which restricts the plastic deformation inside the wedge and prevents a significant load drop. Moreover, the wedge transmits the indenter load and generates a stress concentration at its tip. At larger indenter penetrations, the load drops occur due to the heterogeneous dislocation nucleation from the junctions near the wedge tip, see Fig. 6.7(d) for example. Considering the dominant effect of bulk dislocation junctions on stress relaxation in the (100) indentation, we propose that such type of dislocation lock can act as a

heterogeneous source to initiate dislocation avalanches and thus the experimentally measured indenter displacement burst. This source is located inside the crystal, consistent with the Weibull analysis of the (100) nanoindentation experiment ($d \approx 3$). In contrast, MD simulations show that for both the (111) and (110) indentations, the load drops occur immediately after the first nucleation event. In particular, no major locks form owing to the fact that several equivalent nucleation sites are located off the central axis and at different locations, as shown in Fig. 6.7(a). This facilitates the escape of dislocations to the surface, as well as injection into the bulk. The former process creates the heterogeneous surface sources that could initiate dislocation avalanches leading to the indenter displacement burst. In these two cases, the locations of heterogeneous sources are consistent with those from the Weibull analysis of experiments ($d \approx 2$).

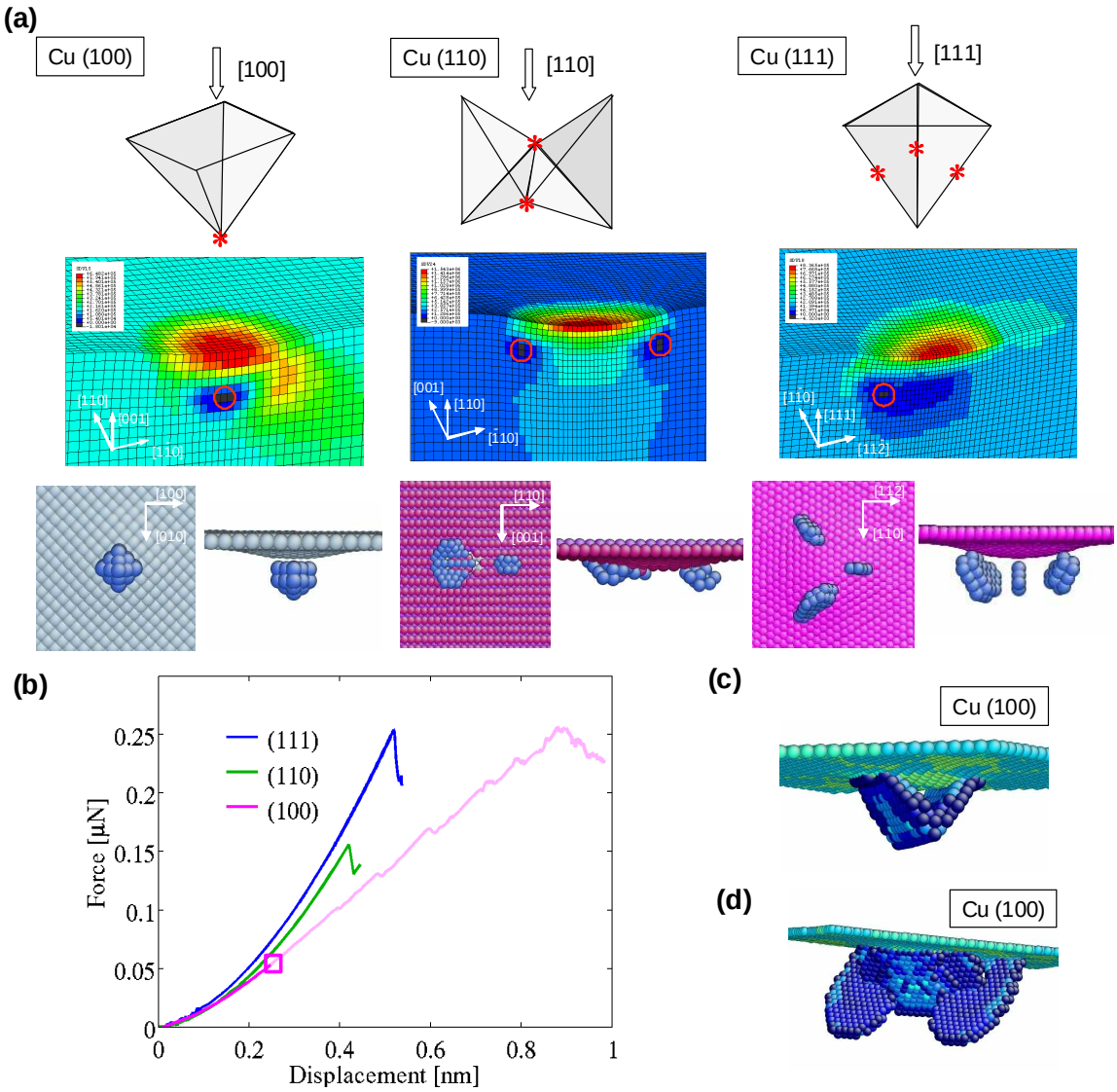

Fig. 6.7. Modeling of nanoindentation on the (111), (110), and (100) surface of single crystal Cu. (a) Dislocation nucleation sites. Upper: schematics (stars); middle: IPFEM predictions (circles) when the indenter radius R = 50 nm; lower: MD simulations when R = 5 nm – atoms are colored by the coordination number and the perfectly coordinated atoms are removed to show the surface and dislocation embryos. (b) Indenter load-displacement responses from MD simulations; (c) Post-nucleation dislocation structures for the (100) indentation at a small indentation penetration. (d) Same as (c) except at large indenter displacement. In both (c) and (d), atoms are colored by the central

symmetry parameter to show the wedged-shape lock junction bounded by the two stacking faults on the {111} slip planes.

6.5 Conclusions

We have simulated nanoindentation and predicted dislocation nucleation in fcc single crystals of Al, Cu and Ni. Simulations are performed using the interatomic potential finite element method, which is a computationally efficient approach that facilitates the study at length scales large compared to atomic dimensions, while remaining faithful to the nonlinear interatomic interactions. We consider homogenous dislocation nucleation triggered by the nonlinear elastic instability of crystal at large strain and nearly zero-*K* temperature. The results show that the critical resolved shear stress of nucleation is at the GPa-level, close to the theoretical limit of perfect crystals. However, the critical conditions of dislocation nucleation, including the indentation load of nucleation, location of nucleation site, nucleation stress and activated slip systems, sensitively depend on the indentation orientation. But these conditions are consistent for different fcc crystals. Last but not least, we have also studied the stochastic, discontinuous plastic deformation in the nanoscale volumes of single crystal Cu and explored the characteristics of the nucleation. The mechanisms of the nucleation-controlled plasticity and dimensionality of nucleation source have been studied.

CHAPTER 7

CONCLUTIONS

We study the plasticity mechanisms of diffusionless martensite phase transformation in Nickel-Titanium. NiTi usually exhibits various metastable phases (B2, B19, B19′, R etc.), the activation of which depends sensitively on temperature, loading, concentration, and precipitation, etc. The formation of a variety of twin structures further complicates the study. Also, nanoscale size effects play an important role in the controlling of pseudoelasticity, shape memory and other plastic deformation. We begin the study with understanding the nanotwin structure in NiTi martensite by molecular statics. Then molecular dynamics simulations are applied to study the temperature-driven B2 → B19′ phase transitions. Then the stress-driven martensitic phase transformation governing the pseudoelasticity and shape memory effects in NiTi nanopillars is explored by molecular dynamics. Monte Carlo simulations are conducted to characterize the temperature- driven B2 → B19 phase transition and the patterning of martensitic nanotwins in NiTi thin films, which is not easy to be achieved by molecular dynamics due to its time scale limitations. Finally, phase field simulations are performed to predict the formation and evolution of complex martensitic microstructures, including the detailed analysis of twin compatibility under complex loading conditions in a larger modeling system. The above results not only provide new insights into the nanoscale martensitic phase transformation in NiTi, but also provide an effective modeling framework for studying the diffusionless phase transformation in large systems with atomic resolution.

We also study the nucleation-controlled plastic deformation in metals, which is the underlying deformation mechanism in ultra-strength nano materials. Our work focuses on understanding how dislocations nucleate in single crystals. Interatomic potential finite element method is applied to determine when, where and how dislocations nucleate during nanoindentation in metals such as Cu, Al and Ni. We explore the effects of indentation orientation on the characteristics of activated dislocation sources. Results provide insights into the nanoscale mechanisms of plastic yielding, and are useful for guiding the nanomechanical experiments in the future.

Overall, the nanomechanics study in this thesis provides novel mechanistic insights into the deformation mechanisms in shape memory alloys and ultra-strength metallic nanostructures.

APPENDIX A

CRYSTALLOGRAPHIC THEORY OF TWINNED MARTENSITE

We have used the crystallographic theory of twinned martensite [41] to facilitate the construction of initial twin structures. This theory only requires an input of the transformation matrix from the cubic parent phase to monoclinic martensitic phase. The twinning elements, including the twin plane normal $\mathbf{n}$ and twin shear vector $\mathbf{m}$, can be predicted by solving the twinning equation of Eq. (4) in the text. This appendix provides the solution of twinning elements for compound twins. Their relaxed structures are discussed in the section of Results and Discussion. It should be noted that the general solutions provided by Hane and Shield [41] sometimes cannot be directly used in the atomistic simulation when periodic boundary conditions[59] are imposed to eliminate the free surface for studying bulk properties. In other words, it is necessary to construct the deformation gradient matrix such that the twin plane after martensitic transformation remains parallel to one side of the supercell for ensuring periodic twin structures in different supercells.

Consider a pair of symmetry-related transformation matrices

$$\mathbf{F}_I = \frac{1}{a_0}\begin{bmatrix} b/\sqrt{2} & 0 & 0 \\ 0 & c\sin\beta/\sqrt{2} & 0 \\ 0 & -c\cos\beta/\sqrt{2} & a \end{bmatrix} \text{ and } \mathbf{F}_J = \frac{1}{a_0}\begin{bmatrix} b/\sqrt{2} & 0 & 0 \\ 0 & c\sin\beta/\sqrt{2} & 0 \\ 0 & c\cos\beta/\sqrt{2} & a \end{bmatrix} \quad \text{(A1)}$$

We solve the twinning equation of Eq. (4) by following the procedure described by James and Hane (Proposition 1 in page 202 of their paper).[6] Using the experimental values of lattice constant and monoclinic angle listed in Table 1. we obtain two solutions: $\mathbf{n}^{\mathrm{I}} = [0,1,0]$, $\mathbf{m}^{\mathrm{I}} = [0,0,0.2566]$ and $\mathbf{n}^{\mathrm{II}} = [0,0,1]$, $\mathbf{m}^{\mathrm{II}} = [0,0.2252,-0.0268]$, which

give the (010) and (001) compound twin, respectively. This pair of twins is conventionally called reciprocal or conjugate twins. Note that all the vectors are given in the $(\mathbf{i}', \mathbf{j}', \mathbf{k}')$ basis defined in Fig. 1.

Substitution of $\mathbf{n}^{\mathrm{I}}$ and $\mathbf{m}^{\mathrm{I}}$ into Eq. (4) yields $\mathbf{Q} = \mathbf{I}$. As discussed earlier, this result indicates that after the martensitic transformation of variants I and J, the orientation of the twin plane (010) is unchanged as illustrated in Fig. A1(a). This can be readily verified by noting that the twin plane normal after transformation, $\mathbf{n}^{\mathrm{I}}\mathbf{F}^{-1}$, is still along the $[0,1,0]$ direction.

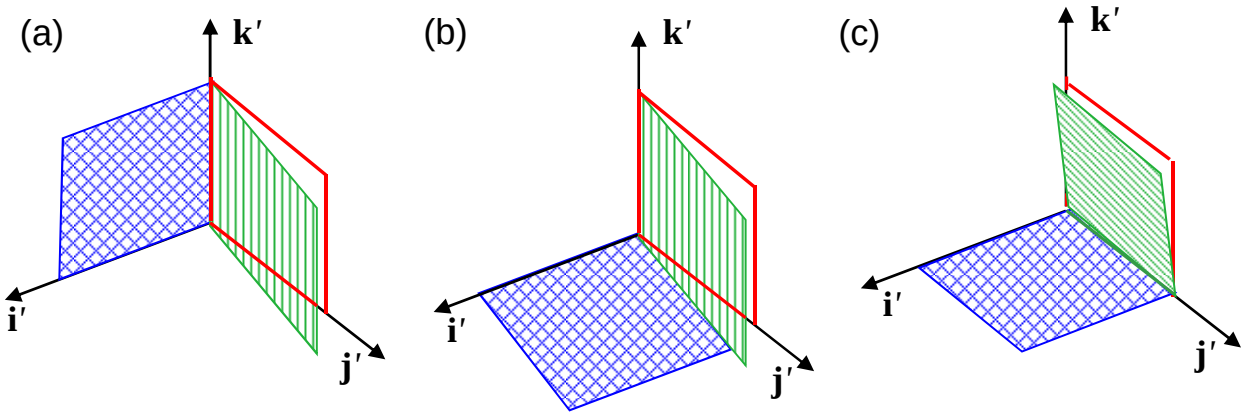

Fig. A1 Illustration of shear transformation and the rotation of the mirror twin plane during the formation of (010) and (001) compound twins. (a) The (010) mirror twin plane (in blue) is unrotated after the shear transformation of the red rectangle to green parallelogram in the $(\mathbf{j}', \mathbf{k}')$ plane along the $\mathbf{k}'$ direction. (b) The (001) mirror twin plane (in blue) is rotated after the same shear transformation as (a). (c) The (001) mirror twin plane (in blue) is unrotated after the shear transformation of the red rectangle to green parallelogram in the $(\mathbf{j}', \mathbf{k}')$ plane along the $\mathbf{j}'$ direction.

In contrast, substitution of $\mathbf{n}^{\mathrm{II}}$ and $\mathbf{m}^{\mathrm{II}}$ into Eq. (4) yields $\mathbf{Q}$ unequal to the identity matrix. This is consistent with the fact that the orientation of the twin plane (001) is changed after martensitic transformation, as shown in Fig. A1(b). Indeed, the twin plane normal after transformation, $\mathbf{n}^{\mathrm{I}}\mathbf{F}^{-1}$, is in the $[0,0,1]$ direction. To ensure the periodicity of (001) compound twins in different supercells, we construct a pair of transformation matrices that are equivalent to those given by Eq. (A1), but keep the twin plane unrotated after martensitic transformation (see Fig. A1(c)),

$$\mathbf{F}_I^* = \frac{1}{a_0}\begin{bmatrix} b/\sqrt{2} & 0 & 0 \\ 0 & c/\sqrt{2} & -a\cos\beta \\ 0 & 0 & a\sin\beta \end{bmatrix} \text{ and } \mathbf{F}_J^* = \frac{1}{a_0}\begin{bmatrix} b/\sqrt{2} & 0 & 0 \\ 0 & c/\sqrt{2} & a\cos\beta \\ 0 & 0 & a\sin\beta \end{bmatrix} \quad \text{(A2)}$$

The above matrices are constructed by noting that the martensitic transformation of the B2 to B19' phase can be considered as an expansion or contraction along the edges of a tetragonal unit cell (see Fig. 1), followed by a simple shear to a monoclinic angle β. This simple shear can be achieved by rotating the $\mathbf{j}'$ axis about the $\mathbf{i}'$ axis, giving Eq. (A1) or equivalently by rotating $\mathbf{k}'$ about $\mathbf{i}'$, giving Eq. (A2). Solution of Eq. (1) with an input of Eq. (A2) gives compound twins of $\mathbf{n}^{\mathrm{I}} = [0,1,0]$, $\mathbf{m}^{\mathrm{I}} = [0,-0.0304,0.2550]$ and $\mathbf{n}^{\mathrm{II}} = [0,0,1]$, $\mathbf{m}^{\mathrm{II}} = [0,0.227,0]$. They are equivalent to the results from Eq. (A1), differing by a rotation.

Incidentally, Eq. (A2) can also be obtained by a more general procedure of starting from Eq. (A1) and then constructing a matrix that rotates the twin plane so that it is parallel to the side of the supercell, i.e., $\mathbf{F}_J^* = \mathbf{Q}^*\mathbf{F}_J$ and $\mathbf{F}_I^* = \mathbf{Q}^{*\mathrm{T}}\mathbf{F}_J$, where

$$\mathbf{Q}^{*} = \begin{bmatrix} 1 & 0 & 0 \\ 0 & \sin\beta & \cos\beta \\ 0 & -\cos\beta & \sin\beta \end{bmatrix} \qquad \text{(A3)}$$

This “transformation and rotation” procedure is general, and can be applied to construct other types of twins in periodic supercells.

APPENDIX B

STRESS FIELD IN FOURIER SPACE

One needs to solve the equilibrium equations to obtain the total strain $\boldsymbol{\varepsilon}$ and stress $\boldsymbol{\tau}$. We define a differential operator

$$\mathbf{A} = \begin{pmatrix} \frac{\partial}{\partial x_1} & 0 & 0 & 0 & \frac{\partial}{\partial x_3} & \frac{\partial}{\partial x_2} \\ 0 & \frac{\partial}{\partial x_2} & 0 & \frac{\partial}{\partial x_3} & 0 & \frac{\partial}{\partial x_1} \\ 0 & 0 & \frac{\partial}{\partial x_3} & \frac{\partial}{\partial x_2} & \frac{\partial}{\partial x_1} & 0 \end{pmatrix}^T \tag{B1}$$

where x_1, x_2 and x_3 are the spatial coordinate. Then the geometry equation of strain can be represented as

$$\boldsymbol{\varepsilon} = \boldsymbol{A}\boldsymbol{u} \tag{B2}$$

where the displacement vector $\boldsymbol{u} = (u_1, u_2, u_3)^T$ is a function of x_1, x_2 and x_3.

The equilibrium equation can be written as

$$\boldsymbol{A}^T\boldsymbol{\tau} = \mathbf{0} \tag{B3}$$

It is non-trivial to obtain the analytical solution of Eq. (5.10), (B2) and (B3) for generally prescribed boundary conditions. Instead, these equations can be discretized and numerically solved. However, direct solution of Eq. (5.10), (B2) and (B3) could be computationally inefficient, since a set of partial difference equations for the whole field needs to be satisfied at each time step. However, for the problem with periodic boundary conditions, the semi-implicit algorithm, which is originally developed by Chen and Shen, can significantly improve the computational efficiency by applying the Fast Fourier Transformation (FFT). The differential equations are transformed to linear equations mutually independent at different mesh node [99]. In this appendix, we present the

detailed formulation and procedure of solving the equilibrium equations with the FFT method by partially following the approach introduced by Shu and Yen [92].

The total strain $\boldsymbol{\varepsilon}$, transformation strain $\boldsymbol{\varepsilon}^*$ and stress $\boldsymbol{\tau}$ are discomposed into the homogeneous and inhomogeneous components

$$\boldsymbol{\varepsilon} = \langle \boldsymbol{\varepsilon} \rangle + \boldsymbol{\varepsilon}', \text{ where } \langle \boldsymbol{\varepsilon} \rangle = \int_V \boldsymbol{\varepsilon}\, d^3r \tag{B4}$$

and

$$\boldsymbol{\varepsilon}^* = \langle \boldsymbol{\varepsilon}^* \rangle + \boldsymbol{\varepsilon}^{*\prime}, \text{ where } \langle \boldsymbol{\varepsilon}^* \rangle = \int_V \boldsymbol{\varepsilon}^*\, d^3r \tag{B5}$$

One can further decompose the total displacement $\boldsymbol{u}$ into a homogeneous and an inhomogeneous component

$$\boldsymbol{u} = \langle \boldsymbol{u} \rangle + \boldsymbol{u}' \text{ satisfying } \langle \boldsymbol{\varepsilon} \rangle = \boldsymbol{A}\langle \boldsymbol{u} \rangle \text{ and } \boldsymbol{\varepsilon}' = \boldsymbol{A}\boldsymbol{u}' \tag{B6}$$

Note that the homogeneous component $\langle \boldsymbol{u} \rangle$ is a linear function of $\boldsymbol{x}$, because the homogeneous strain $\langle \boldsymbol{\varepsilon} \rangle$ is a constant. Although this decomposition in Eq. (B6) is not unique with a constant plus a rigid body rotation, it will not affect the result of our interest, because we will only use the differential form of displacement $\boldsymbol{u}'$.

Substitution of Eq. (B4) and (B5) into Eq. (5.10) yields

$$\boldsymbol{\tau} = \boldsymbol{C} \cdot (\boldsymbol{\varepsilon} - \boldsymbol{\varepsilon}^*) = \boldsymbol{C} \cdot (\langle \boldsymbol{\varepsilon} \rangle - \langle \boldsymbol{\varepsilon}^* \rangle) + \boldsymbol{C} \cdot (\boldsymbol{\varepsilon}' - \boldsymbol{\varepsilon}^{*\prime}) = \langle \boldsymbol{\tau} \rangle + \boldsymbol{\tau}' \tag{B7}$$

where the homogeneous stress is defined as

$$\langle \boldsymbol{\tau} \rangle = \boldsymbol{C} \cdot (\langle \boldsymbol{\varepsilon} \rangle - \langle \boldsymbol{\varepsilon}^* \rangle) \tag{B8}$$

and the inhomogeneous stress is

$$\boldsymbol{\tau}' = \boldsymbol{C} \cdot (\boldsymbol{\varepsilon}' - \boldsymbol{\varepsilon}^{*\prime}) \tag{B9}$$

In each simulation time step, once the field variables $\eta_1, \eta_2, \cdots, \eta_{12}$ are known, $\boldsymbol{\varepsilon}^*$ is can be directly calculated from Eq. (5.1), so that it is easy to calculate $\langle \boldsymbol{\varepsilon}^* \rangle$ from Eq. (B5). The applied boundary conditions can be given by either $\langle \boldsymbol{\varepsilon} \rangle = \boldsymbol{\varepsilon}^{app}$ or $\langle \boldsymbol{\tau} \rangle = \boldsymbol{\tau}^{app}$,

or a mixed type. Together with Eq. (B8), all the homogeneous components $\langle \boldsymbol{\varepsilon} \rangle$ and $\langle \boldsymbol{\tau} \rangle$ can be obtained.

The equilibrium equation of $\boldsymbol{\tau}'$ remain the same form

$$\boldsymbol{A}^T \boldsymbol{\tau}' = \boldsymbol{0} \tag{B10}$$

Substituting Eq. (B6) into Eq. (B9) and (B10), we obtain the partial differential equations

$$\boldsymbol{A}^T \boldsymbol{C} \boldsymbol{A} \boldsymbol{u}' = \boldsymbol{A}^T \boldsymbol{C} \boldsymbol{\varepsilon}^{*\prime} \tag{B11}$$

For an integral equation $f: R^3 \to R$, the Fourier transformation is defined by

$$\widehat{f(\boldsymbol{s})} = \mathcal{F}(f) = \iiint_{-\infty}^{\infty} f(\boldsymbol{x}) e^{-2\pi i \boldsymbol{x} \cdot \boldsymbol{s}} d\boldsymbol{x} \tag{B12}$$

where $\boldsymbol{s} = (s_1, s_2, s_3)^T$ is the coordinate in the reciprocal space.

The inverse Fourier transformation is defined by

$$f(\boldsymbol{x}) = \mathcal{F}^{-1}(\hat{f}) = \iiint_{-\infty}^{\infty} \widehat{f(\boldsymbol{s})}\, e^{2\pi i \boldsymbol{x} \cdot \boldsymbol{s}} d\boldsymbol{s} \tag{B13}$$

It can be shown that the differential operator $\boldsymbol{A}$ in the real space is transformed to the linear operator $\boldsymbol{B}$ in the reciprocal space, which is given by

$$\mathbf{B} = 2\pi i \begin{pmatrix} s_1 & 0 & 0 & 0 & s_3 & s_2 \\ 0 & s_2 & 0 & s_3 & 0 & s_1 \\ 0 & 0 & s_3 & s_2 & s_1 & 0 \end{pmatrix}^T \tag{B14}$$

Then $\widehat{\boldsymbol{u}'}$ is obtained from Eq. (B11) as

$$\widehat{\boldsymbol{u}'} = \mathcal{F}(\boldsymbol{u}') = (\boldsymbol{B}^T \boldsymbol{C} \boldsymbol{B})^{-1} \boldsymbol{B}^T \boldsymbol{C} \widehat{\boldsymbol{\varepsilon}^{*\prime}} \tag{B15}$$

From Eq. (B6), the transformed inhomogeneous strain is

$$\widehat{\boldsymbol{\varepsilon}'} = \mathcal{F}(\boldsymbol{\varepsilon}') = \boldsymbol{B} (\boldsymbol{B}^T \boldsymbol{C} \boldsymbol{B})^{-1} \boldsymbol{B}^T \boldsymbol{C} \widehat{\boldsymbol{\varepsilon}^{*\prime}} \tag{B16}$$

From Eq. (B9), the transformed inhomogeneous stress is

$$\widehat{\boldsymbol{\tau}'} = \mathcal{F}(\boldsymbol{\tau}') = \boldsymbol{C} \boldsymbol{B} (\boldsymbol{B}^T \boldsymbol{C} \boldsymbol{B})^{-1} \boldsymbol{B}^T \boldsymbol{C} \widehat{\boldsymbol{\varepsilon}^{*\prime}} - \boldsymbol{C} \widehat{\boldsymbol{\varepsilon}^{*\prime}} \tag{B17}$$

The inhomogeneous stress and strain can be obtained by the inverse Fourier transformation according to Eq. (B13). Finally, together with the homogeneous stress given by Eq. (B8) and the boundary condition, one can obtain the driving force associated with elastic energy density given in Eq. (5.11). If the kinetic equations Eq. (5.16) are also solved in the Fourier space, the inverse transformation of stress is not needed in the phase field simulation.

REFERENCES

[1] Christian JW, Mahajan S. Deformation Twinning. Progress in Materials Science 1995;39:1.

[2] Otsuka K, Kakeshita T. Science and technology of shape-memory alloys. New developments. Mrs Bulletin 2002;27:91.

[3] Otsuka K, Wayman CM. Shape Memory Materials, Cambridge University Press, Cambridge, UK 1998.

[4] Otsuka K, Ren X. Physical metallurgy of Ti-Ni-based shape memory alloys. Progress in Materials Science 2005;50:511.

[5] Otsuka K, Wayman C. Shape Memory Materials. Cambridge, UK: Cambridge University Press 1998.

[6] James RD, Hane KF. Martensitic transformations and shape-memory materials. Acta Materialia 2000;48:197.

[7] Bhattacharya K. Microstructure of martensite. Why it forms and how it gives rise to the shape-memory effect. Oxford, UK: Oxford University Press 2003.

[8] Waitz T, Tsuchiya K, Antretter T, Fischer FD. Phase Transformations of Nanocrystalline Martensitic Materials. Mrs Bulletin 2009;34:814.

[9] Waitz T, Kazykhanov V, Karnthaler HP. Martensitic phase transformations in nanocrystalline NiTi studied by TEM. Acta Materialia 2004;52:137.

[10] Ma XG, Komvopoulos K. Nanoscale pseudoelastic behavior of indented titanium-nickel films. Applied Physics Letters 2003;83:3773.

[11] Wood AJM, Clyne TW. Measurement and modelling of the nanoindentation response of shape memory alloys. Acta Materialia 2006;54:5607.

[12] Frick CP, Lang TW, Spark K, Gall K. Stress-induced martensitic transformations and shape memory at nanometer scales. Acta Materialia 2006;54:2223.

[13] Frick CP, Orso S, Arzt E. Loss of pseudoelasticity in nickel-titanium sub-micron compression pillars. Acta Materialia 2007;55:3845.

[14] Juan JS, No ML, Schuh CA. Nanoscale shape-memory alloys for ultrahigh mechanical damping. Nat Nanotechnol 2009;4:415.

[15] Huang X, Ramirez AG. Effects of film dimension on the phase transformation behavior of NiTi thin films. Applied Physics Letters 2009;95.

[16] Ye J, Mishra RK, Pelton AR, Minor AM. Direct observation of the NiTi martensitic phase transformation in nanoscale volumes. Acta Materialia 2010;58:490.

[17] Waitz T, Spisak D, Hafner J, Karnthaler HP. Size-dependent martensitic transformation path causing atomic-scale twinning of nanocrystalline NiTi shape memory alloys. Europhysics Letters 2005;71:98.

[18] Waitz T, Antretter T, Fischer FD, Simha NK, Karnthaler HP. Size effects on the martensitic phase transformation of NiTi nanograins. Journal of the Mechanics and Physics of Solids 2007;55:419.

[19] Norfleet DM, Sarosi PM, Manchiraju S, Wagner MFX, Uchic MD, Anderson PM, Mills MJ. Transformation-induced plasticity during pseudoelastic deformation in Ni-Ti microcrystals. Acta Materialia 2009;57:3549.

[20] Gunderov D, Lukyanov A, Prokofiev E, Kilmametov A, Pushin V, Valiev R. Mechanical properties and martensitic transformations in nanocrystalline Ti49.4Ni50.6 alloy produced by high-pressure torsion. Materials Science and Engineering a 2009;503:75.

[21] Clark BG, Gianola DS, Kraft O, Frick CP. Size Independent Shape Memory Behavior of Nickel-Titanium. Advanced Engineering Materials 2010;12:808.

[22] Simon T, Kroger A, Somsen C, Dlouhy A, Eggeler G. On the multiplication of dislocations during martensitic transformations in NiTi shape memory alloys. Acta Materialia 2010;58:1850.

[23] Chen Y, Schuh CA. Size effects in shape memory alloy microwires. Acta Materialia 2011;59:537.

[24] Phillips FR, Fang D, Zheng HX, Lagoudas DC. Phase transformation in free-standing SMA nanowires. Acta Materialia 2011;59:1871.

[25] Sun QP, Hwang KC. Micromechanics Modeling for the Constitutive Behavior of Polycrystalline Shape Memory Alloys .1. Derivation of General Relations. Journal of the Mechanics and Physics of Solids 1993;41:1.

[26] Abeyaratne R, Knowles JK. A Continuum Model of a Thermoelastic Solid Capable of Undergoing Phase-Transitions. Journal of the Mechanics and Physics of Solids 1993;41:541.

[27] Cherkaoui M, Sun QP, Song GQ. Micromechanics modeling of composite with ductile matrix and shape memory alloy reinforcement. International Journal of Solids and Structures 2000;37:1577.

[28] Thamburaja P, Anand L. Polycrystalline shape-memory materials: effect of crystallographic texture. Journal of the Mechanics and Physics of Solids 2001;49:709.

[29] Patoor E, Lagoudas DC, Entchev PB, Brinson LC, Gao XJ. Shape memory alloys, Part I: General properties and modeling of single crystals. Mechanics of Materials 2006;38:391.

[30] Sengupta A, Papadopoulos P. Constitutive modeling and finite element approximation of B2-R-B19 ' phase transformations in Nitinol polycrystals. Computer Methods in Applied Mechanics and Engineering 2009;198:3214.

[31] Lai WS, Liu BX. Lattice stability of some Ni-Ti alloy phases versus their chemical composition and disordering. Journal of Physics-Condensed Matter 2000;12:L53.

[32] Zhu T, Li J, Ogata S, Yip S. Mechanics of ultra-strength materials. Mrs Bulletin 2009;34:167.

[33] Wu B, Heidelberg A, Boland JJ, Sader JE, Sun XM, Li YD. Microstructure-hardened silver nanowires. Nano Letters 2006;6:468.

[34] Greer JR, Nix WD. Nanoscale gold pillars strengthened through dislocation starvation. Physical Review B 2006;73:245410.

[35] Wang W, Lu K. Nanoindentation study on elastic and plastic anisotropies of Cu single crystals. Philosophical Magazine 2006;86:5309.

[36] Shan ZW, Mishra RK, Asif SAS, Warren OL, Minor AM. Mechanical annealing and source-limited deformation in submicrometre-diameter Ni crystals. Nature Materials 2008;7:115.

[37] Wang W, Zhong Y, Lu K, Lu L, McDowell DL, Zhu T. Size effects and strength fluctuation in nanoscale plasticity. Acta Materialia 2012;60:3302.

[38] Zhang XY, Sehitoglu H. Crystallography of the B2 -> R -> B 19 ' phase transformations in NiTi. Materials Science and Engineering a-Structural Materials Properties Microstructure and Processing 2004;374:292.

[39] Hatcher N, Kontsevoi OY, Freeman AJ. Martensitic transformation path of NiTi. Physical Review B 2009;79:020202.

[40] Knowles KM, Smith DA. The Crystallography of the Martensitic-Transformation in Equiatomic Nickel-Titanium. Acta Metallurgica 1981;29:101.

[41] Hane KF, Shield TW. Microstructure in the cubic to monoclinic transition in titanium-nickel shape memory alloys. Acta Materialia 1999;47:2603.

[42] Fukuda T, Saburi T, Chihara T, Tsuzuki Y. Mechanism of B2-B19-B19' Transformation in Shape-Memory Ti-Ni-Cu Alloys. Materials Transactions Jim 1995;36:1244.

[43] Krulevitch P, Lee AP, Ramsey PB, Trevino JC, Hamilton J, Northrup MA. Thin film shape memory alloy microactuators. J Microelectromech S 1996;5:270.

[44] Hatcher N, Kontsevoi OY, Freeman AJ. Role of elastic and shear stabilities in the martensitic transformation path of NiTi. Physical Review B 2009;80:144203.

[45] Wagner MFX, Windl W. Lattice stability, elastic constants and macroscopic moduli of NiTi martensites from first principles. Acta Materialia 2008;56:6232.

[46] Wechsler MS, Lieberman DS, Read TA. On the Theory of the Formation of Martensite. Transactions of the American Institute of Mining and Metallurgical Engineers 1953;197:1503.

[47] Ball JM, James RD. Fine Phase Mixtures as Minimizers of Energy. Archive for Rational Mechanics and Analysis 1987;100:13.

[48] Huang XY, Ackland GJ, Rabe KM. Crystal structures and shape-memory behaviour of NiTi. Nature Materials 2003;2:307.

[49] Wang XQ. Twinned structure for shape memory: First-principles calculations. Physical Review B 2008;78.

[50] Kibey S, Sehitoglu H, Johnson DD. Energy landscape for martensitic phase transformation in shape memory NiTi. Acta Materialia 2009;57:1624.

[51] Vishnu KG, Strachan A. Phase stability and transformations in NiTi from density functional theory calculations. Acta Materialia 2010;58:745.

[52] Leclercq S, Lexcellent C. A general macroscopic description of the thermomechanical behavior of shape memory alloys. Journal Of The Mechanics And Physics Of Solids 1996;44:953.

[53] Lu ZK, Weng GJ. Martensitic transformation and stress-strain relations of shape-memory alloys. Journal Of The Mechanics And Physics Of Solids 1997;45:1905.

[54] Huang Y, Zhang F, Hwang KC, Nix WD, Pharr GM, Feng G. A model of size effects in nano-indentation. Journal of the Mechanics and Physics of Solids 2006;54:1668.

[55] Lim TJ, McDowell DL. Cyclic thermomechanical behavior of a polycrystalline pseudoelastic shape memory alloy. Journal Of The Mechanics And Physics Of Solids 2002;50:651.

[56] Lei CH, Li LJ, Shu YC, Li JY. Austenite-martensite interface in shape memory alloys. Applied Physics Letters 2010;96.

[57] Ding XD, Suzuki T, Ren XB, Sun J, Otsuka K. Precursors to stress-induced martensitic transformations and associated superelasticity: Molecular dynamics simulations and an analytical theory. Physical Review B 2006;74.

[58] Finnis MW, Sinclair JE. A Simple Empirical N-Body Potential for Transition-Metals. Philosophical Magazine a-Physics of Condensed Matter Structure Defects and Mechanical Properties 1984;50:45.

[59] Parrinello M, Rahman A. Polymorphic transitions in single-crystals - A new molecular-dynamics method. J Appl Phys 1981;52:7182.

[60] Huang S, Zhang SL, Belytschko T, Terdalkar SS, Zhu T. Mechanics of nanocrack: Fracture, dislocation emission, and amorphization. Journal Of The Mechanics And Physics Of Solids 2009;57:840.

[61] Brill TM, Mittelbach S, Assmus W, Mullner M, Luthi B. Elastic Properties of Niti. Journal of Physics-Condensed Matter 1991;3:9621.

[62] Mercier O, Melton KN, Gremaud G, Hagi J. Single-Crystal Elastic-Constants of the Equiatomic Niti Alloy near the Martensitic-Transformation. J Appl Phys 1980;51:1833.

[63] Elliott RS, Shaw JA, Triantafyllidis N. Stability of crystalline solids - II: Application to temperature-induced martensitic phase transformations in a bi-atomic crystal. Journal Of The Mechanics And Physics Of Solids 2006;54:193.

[64] Dobson M, Elliott RS, Luskin M, Tadmor EB. A multilattice quasicontinuum for phase transforming materials: Cascading Cauchy Born kinematics. Journal Of Computer-Aided Materials Design 2007;14:219.

[65] Morris JR, Ye Y, Krcmar M, Fu CL. The Role of Phase Stability in Ductile, Ordered B2 Intermetallics. In: Wiezorek J, Fu CL, Takeyama M, Morris D, Clemens H, editors. Advanced Intermetallic-Based Alloys, MRS Symposia Proceedings No. 980 (Materials Research Society, Warrendale, PA), 2007. p.II06.

[66] Plimpton S. Fast Parallel Algorithms for Short-Range Molecular-Dynamics. J Comput Phys 1995;117:1.

[67] Miyazaki S, Otsuka K. DEFORMATION AND TRANSITION BEHAVIOR ASSOCIATED WITH THE R-PHASE IN TI-NI ALLOYS. Metallurgical Transactions A 1986;17:53.

[68] Ogata S, Li J, Yip S. Energy landscape of deformation twinning in bcc and fcc metals. Physical Review B 2005;71:224102.

[69] Lu L, Shen YF, Chen XH, Qian LH, Lu K. Ultrahigh strength and high electrical conductivity in copper. Science 2004;304:422.

[70] Zhu T, Li J, Samanta A, Kim HG, Suresh S. Interfacial plasticity governs strain rate sensitivity and ductility in nanostructured metals. Proceedings of the National Academy of Sciences of the USA 2007;104:3031.

[71] Lu L, Chen X, Huang X, Lu K. Revealing the Maximum Strength in Nanotwinned Copper. Science 2009;323:607.

[72] Li XY, Wei YJ, Lu L, Lu K, Gao HJ. Dislocation nucleation governed softening and maximum strength in nano-twinned metals. Nature 2010;464:877.

[73] Zhu T, Li J. Ultra-strength Materials. Progress In Materials Science 2010;55:710.

[74] Zhong Y, Gall K, Zhu T. Atomistic study of nanotwins in NiTi shape memory alloys. J Appl Phys 2011;110:033532.

[75] Mutter D, Nielaba P. Simulation of structural phase transitions in NiTi. Physical Review B 2010;82:224201.

[76] Mutter D, Nielaba P. Simulation of the thermally induced austenitic phase transition in NiTi nanoparticles. The European Physical Journal B 2011;84:109.

[77] Pun GPP, Mishin Y. Molecular dynamics simulation of the martensitic phase transformation in NiAl alloys. Journal of Physics-Condensed Matter 2010;22.

[78] Holec D, Friák M, Dlouhý A, Neugebauer J. Ab initio study of pressure stabilized NiTi allotropes: Pressure-induced transformations and hysteresis loops. Physical Review B 2011;84:224119.

[79] Park HS, Gall K, Zimmerman JA. Shape memory and pseudoelasticity in metal nanowires. Physical Review Letters 2005;95:255504.

[80] Liang WW, Zhou M, Ke FJ. Shape memory effect in Cu nanowires. Nano Letters 2005;5:2039.

[81] Li SZ, Ding XD, Deng JK, Lookman T, Li J, Ren XB, Sun J, Saxena A. Superelasticity in bcc nanowires by a reversible twinning mechanism. Physical Review B 2010;82:205435.

[82] Li SZ, Ding XD, Li J, Ren XB, Sun J, Ma E, Lookman T. Inverse martensitic transformation in Zr nanowires. Physical Review B 2010;81:245433.

[83] Otsuka K, Ren X. Martensitic transformations in nonferrous shape memory alloys. Materials Science and Engineering a 1999;273:89.

[84] Qiu S, Clausen B, II SAP, Noebe RD, Vaidyanathan R. On elastic moduli and elastic anisotropy in polycrystalline martensitic NiTi. Acta Materialia 2011;59:5055.

[85] Ishida A, Sato M. Thickness effect on shape memory behavior of Ti-50.0at.%Ni thin film. Acta Materialia 2003;51:5571.

[86] Fu YQ, Zhang S, Wu MJ, Huang WM, Du HJ, Luo JK, Flewitt AJ, Milne WI. On the lower thickness boundary of sputtered TiNi films for shape memory application. Thin Solid Films 2006;515:80.

[87] Juan JS, No ML, Schuh CA. Thermomechanical behavior at the nanoscale and size effects in shape memory alloys. Journal of Materials Research 2011;26:2461.

[88] Schlom DG, Chen LQ, Eom CB, Rabe KM, Streiffer SK, Triscone JM. Strain tuning of ferroelectric thin films. Ann. Rev. Mater. Res. 2007;37:589.

[89] Saxena A, Aeppli G. Phase Transitions at the Nanoscale in Functional Materials. Mrs Bulletin 2009;34:804.

[90] Kaufmann S, Niemann R, Thersleff T, Rossler UK, Heczko O, Buschbeck J, Holzapfel B, Schultz L, Fahler S. Modulated martensite: why it forms and why it deforms easily. New J Phys 2011;13.

[91] Chen LQ. Phase-field models for microstructure evolution. Ann. Rev. Mater. Res. 2002;32:113.

[92] Shu YC, Yen JH. Multivariant model of martensitic microstructure in thin films. Acta Materialia 2008;56:3969.

[93] Metropolis N, Rosenbluth AW, Rosenbluth MN, Teller AH, Teller E. Equation of State Calculations by Fast Computing Machines. Journal of Chemical Physics 1953;21:1087.

[94] Zhong Y, Zhu T. Atomistic characterization of pseudoelasticity and shape memory in NiTi nanopillars Acta Materialia In press.

[95] Verwey GC, Warner M, Terentjev EM. Elastic instability and stripe domains in liquid crystalline elastomers. Journal De Physique Ii 1996;6:1273.

[96] Bhattacharya K. Theory of martensitic microstructure and the shape-memory effect. Theory of martensitic microstructure and the shape-memory effect, Available from author: bhatta@co.caltech.edu 1998.

[97] Zhong Y, Zhu T. Patterning and Branching of Martensitic Nanotwins In preparation.

[98] Artemev A, Jin Y, Khachaturyan AG. Three-dimensional phase field model of proper martensitic transformation. Acta Materialia 2001;49:1165.

[99] Chen LQ, Shen J. Applications of semi-implicit Fourier-spectral method to phase field equations. Comput Phys Commun 1998;108:147.

[100] Wang Y, Khachaturyan AG. Three-dimensional field model and computer modeling of martensitic transformations. Acta Materialia 1997;45:759.

[101] Yang L, Dayal K. Formulation of phase-field energies for microstructure in complex crystal structures. Applied Physics Letters 2010;96.

[102] Anand L, Gurtin ME. Thermal effects in the superelasticity of crystalline shape-memory materials. Journal Of The Mechanics And Physics Of Solids 2003;51:1015.

[103] Thamburaja P. Superelasticity in polycrystalline shape-memory materials: effect of crystallographic texture. Doctoral Dissertation, Massachusetts Institute of Technology 2002.

[104] Page TF, Oliver WC, McHargue CJ. The deformation-behavior of ceramic crystals subjected to very low load (nano)indentations. Journal Of Materials Research 1992;7:450.

[105] Gerberich WW, Nelson JC, Lilleodden ET, Anderson P, Wyrobek JT. Indentation induced dislocation nucleation: The initial yield point. Acta Materialia 1996;44:3585.

[106] Gouldstone A, Koh HJ, Zeng KY, Giannakopoulos AE, Suresh S. Discrete and continuous deformation during nanoindentation of thin films. Acta Materialia 2000;48:2277.

[107] Minor AM, Asif SAS, Shan ZW, Stach EA, Cyrankowski E, Wyrobek TJ, Warren OL. A new view of the onset of plasticity during the nanoindentation of aluminium. Nature Materials 2006;5:697.

[108] Gouldstone A, Chollacoop N, Dao M, Li J, Minor AM, Shen YL. Overview No. 142: Indentation across size scales and disciplines: Recent developments in experimentation and modeling. Acta Materialia 2007;55:4015.

[109] Li J, Van Vliet KJ, Zhu T, Yip S, Suresh S. Atomistic mechanisms governing elastic limit and incipient plasticity in crystals. Nature 2002;418:307.

[110] Van Vliet KJ, Li J, Zhu T, Yip S, Suresh S. Quantifying the early stages of plasticity through nanoscale experiments and simulations. Physical Review B 2003;67:104105.

[111] Zhu T, Li J, Van Vliet KJ, Ogata S, Yip S, Suresh S. Predictive modeling of nanoindentation-induced homogeneous dislocation nucleation in copper. Journal Of The Mechanics And Physics Of Solids 2004;52:691.

[112] Ericksen JL. The Cauchy and Born hypotheses for crystals. In: Gurtin ME, editor. Phase Transformations and Material Instabilities in Solids. New York: Academic Press, 1984. p.61.

[113] Daw MS, Baskes MI. Embedded-Atom Method - Derivation And Application To Impurities, Surfaces, And Other Defects In Metals. Physical Review B 1984;29:6443.

[114] Mishin Y, Farkas D, Mehl MJ, Papaconstantopoulos DA. Interatomic potentials for monoatomic metals from experimental data and ab initio calculations. Physical Review B 1999;59:3393.

[115] Mishin Y, Mehl MJ, Papaconstantopoulos DA, Voter AF, Kress JD. Structural stability and lattice defects in copper: Ab initio, tight-binding, and embedded-atom calculations. Physical Review B 2001;63:224106.

[116] Park HS, Klein PA, Wagner GJ. A surface Cauchy-Born model for nanoscale materials. International Journal for Numerical Methods in Engineering 2006;68:1072.

[117] ABAQUS. Theory Manual. Hibbitt, Karlsson and Sorensen Inc., Pawtucket, R.I. 2006.

[118] Hill R. Acceleration Waves in Solids. Journal Of The Mechanics And Physics Of Solids 1962;10:1.

[119] Rice JR. The localization of plastic deformation. In: Koiter WT, editor. Proceedings of the 14th International Congress on Theoretical and Applied Mechanics: North-Holland Publishing Co., Amsterdam, 1976. p.207.

[120] Zimmerman JA, Kelchner CL, Klein PA, Hamilton JC, Foiles SM. Surface step effects on nanoindentation. Physical Review Letters 2001;8716:165507.

[121] Yu HH, Shrotriya P, Gao YF, Kim KS. Micro-plasticity of surface steps under adhesive contact: Part I - Surface yielding controlled by single-dislocation nucleation. Journal Of The Mechanics And Physics Of Solids 2007;55:489.

[122] Swadener JG, Pharr GM. Indentation of elastically anisotropic half-spaces by cones and parabolae of revolution. Philosophical Magazine A-Physics Of Condensed Matter Structure Defects And Mechanical Properties 2001;81:447.

[123] Gao YF, Pharr GM. Multidimensional contact moduli of elastically anisotropic solids. Scripta Materialia 2007;57:13.

[124] Bei H, George EP, Hay JL, Pharr GM. Influence of indenter tip geometry on elastic deformation during nanoindentation. Physical Review Letters 2005;95:045501.

[125] Tsuru T, Shibutani Y. Anisotropic effects in elastic and incipient plastic deformation under (001), (110), and (111) nanoindentation of Al and Cu. Physical Review B 2007;75:035415.

[126] Volkert CA, Lilleodden ET. Size effects in the deformation of sub-micron Au columns. Philosophical Magazine 2006;86:5567.

[127] Ng KS, Ngan AHW. Stochastic theory for jerky deformation in small crystal volumes with pre-existing dislocations. Philosophical Magazine 2008;88:677.

[128] Kiely JD, Houston JE. Nanomechanical properties of Au (111), (001), and (110) surfaces. Physical Review B 1998;57:12588.

[129] Gouldstone A, Chollacoop N, Dao M, Li J, Minor AM, Shen YL. Indentation across size scales and disciplines: Recent developments in experimentation and modeling. Acta Materialia 2007;55:4015.

[130] Nix WD, Gao HJ. Indentation size effects in crystalline materials: A law for strain gradient plasticity. Journal Of The Mechanics And Physics Of Solids 1998;46:411.

[131] Sieradzki K, Rinaldi A, Friesen C, Peralta P. Length scales in crystal plasticity. Acta Materialia 2006;54:4533.

[132] McDowell DL. Viscoplasticity of heterogeneous metallic materials. Materials Science & Engineering R-Reports 2008;62:67.

[133] Rinaldi A, Peralta P, Friesen C, Sieradzki K. Sample-size effects in the yield behavior of nanocrystalline nickel. Acta Materialia 2008;56:511.

[134] Zhong Y, Zhu T. Simulating nanoindentation and predicting dislocation nucleation using interatomic potential finite element method. Computer Methods In Applied Mechanics And Engineering 2008;197:3174.

[135] Liang HY, Woo CH, Huang HC, Ngan AHW, Yu TX. Crystalline plasticity on copper (001), (110), and (111) surfaces during nanoindentation. Cmes-Computer Modeling in Engineering & Sciences 2004;6:105.